



HAL
open science

Stability Enhancement of Inverter-dominated power systems with virtual inertia control

Lalitha Subramanian

► **To cite this version:**

Lalitha Subramanian. Stability Enhancement of Inverter-dominated power systems with virtual inertia control. Electric power. Université Grenoble Alpes [2020-..]; Nanyang Technological University (Singapour), 2021. English. NNT : 2021GRALT060 . tel-03505925

HAL Id: tel-03505925

<https://theses.hal.science/tel-03505925v1>

Submitted on 1 Jan 2022

HAL is a multi-disciplinary open access archive for the deposit and dissemination of scientific research documents, whether they are published or not. The documents may come from teaching and research institutions in France or abroad, or from public or private research centers.

L'archive ouverte pluridisciplinaire **HAL**, est destinée au dépôt et à la diffusion de documents scientifiques de niveau recherche, publiés ou non, émanant des établissements d'enseignement et de recherche français ou étrangers, des laboratoires publics ou privés.



THÈSE

Pour obtenir le grade de

DOCTEUR DE L'UNIVERSITÉ GRENOBLE ALPES

Spécialité : GENIE ELECTRIQUE

Arrêté ministériel : 25 mai 2016

Présentée par

Lalitha SUBRAMANIAN

Thèse dirigée par **Nouredine HADJSAID**
et codirigée par **Vincent DEBUSSCHERE**, Enseignant chercheur,
Université Grenoble Alpes

préparée au sein du **Laboratoire Laboratoire de Génie
Electrique**
dans l'**École Doctorale Electronique, Electrotechnique,
Automatique, Traitement du Signal (EEATS)**

**Stabilité des systèmes électriques à fort taux
de production basée sur des convertisseurs
statiques incluant un contrôle d'inertie
virtuelle**

**Stability Enhancement of Inverter-dominated
power systems with virtual inertia control**

Thèse soutenue publiquement le **1 septembre 2021**,
devant le jury composé de :

Monsieur Nouredine HADJSAID

PROFESSEUR DES UNIVERSITES, GRENOBLE INP, Directeur de
thèse

Monsieur Miroslav BEGOVIC

PROFESSEUR, Texas A&M University, Rapporteur

Monsieur Bala VENKATESH

PROFESSEUR, Ryerson University, Rapporteur

Monsieur Josep POU

PROFESSEUR, Nanyang Technological University, Président

Monsieur David FREY

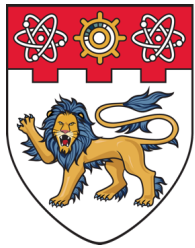
MAITRE DE CONFERENCE, UNIVERSITE GRENOBLE ALPES,
Examineur

Monsieur Hoay Beng GOOI

PROFESSEUR ASSOCIE, Nanyang Technological University, Directeur
de thèse

Monsieur Vincent DEBUSSCHERE

MAITRE DE CONFERENCE HDR, Univ. Grenoble Alpes, Co-directeur de
thèse



**NANYANG
TECHNOLOGICAL
UNIVERSITY**
SINGAPORE

UGA
Université
Grenoble Alpes

**STABILITY ENHANCEMENT OF INVERTER
DOMINATED POWER SYSTEMS USING VIRTUAL
INERTIA CONTROL**

LALITHA SUBRAMANIAN

Interdisciplinary Graduate Programme
Energy Research Institute @ NTU

2020

**STABILITY ENHANCEMENT OF INVERTER
DOMINATED POWER SYSTEMS USING VIRTUAL
INERTIA CONTROL**

LALITHA SUBRAMANIAN

**INTERDISCIPLINARY GRADUATE PROGRAMME
and
GRENOBLE INP**

A thesis submitted to **Nanyang Technological University**
and **Université Grenoble Alps**
in partial fulfillment of the requirements for the degree of
Doctor of Philosophy

2020

Statement of Originality

I hereby certify that the work embodied in this thesis is the result of original research, is free of plagiarised materials, and has not been submitted for a higher degree to any other University or Institution.

28/08/2020

.....

Date

Lalitha S.

.....

Lalitha Subramanian

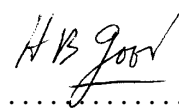
Supervisor Declaration Statement

I have reviewed the content and presentation style of this thesis and declare it is free of plagiarism and of sufficient grammatical clarity to be examined. To the best of my knowledge, the research and writing are those of the candidate except as acknowledged in the Author Attribution Statement. I confirm that the investigations were conducted in accord with the ethics policies and integrity standards of Nanyang Technological University and that the research data are presented honestly and without prejudice.

28/08/2020

.....

Date




.....

Assoc. Prof. H. B. Gooi

Supervisor Declaration Statement

I have reviewed the content and presentation style of this thesis and declare it is free of plagiarism and of sufficient grammatical clarity to be examined. To the best of my knowledge, the research and writing are those of the candidate except as acknowledged in the Author Attribution Statement. I confirm that the investigations were conducted in accord with the ethics policies and integrity standards of Université Grenoble Alps.

28/08/2020...



Nouredine HADJSAID
Directeur du laboratoire
G2Elab



Date

Assoc. Prof. Vincent Debusschere

Prof. Nouredine Hadjsaid



Authorship Attribution Statement

I have worked on the development of the proposed control strategies, their simulation/validation and analysis in the different topics. The other notable contributions to the thesis are as follows:

- Dr. Ujjal Manandhar guided me in setting up the testbench at the CERL, NTU, which was used for the droop control validation in Chapter 5.
- Mr. Cedric Boudinet and Mr. William Norris helped me modify the connections at the FLIRT real-time testing facility at G2Elab.
- Mr. Antoine Labonne and I had worked on setting up a power hardware-in-the-loop experiment at the PREDIS, PDE facility, which could not be continued later due to the COVID 19 outbreak.
- Assoc. Prof. Vincent Debusschere helped me frame the objectives of the respective researches, provided technical inputs, supervised my research, and proofread the manuscripts.
- Assoc. Prof. H. B. Gooi supervised the research work, proofread the manuscript at various stages, suggested improvements to the content and organization of the manuscript, and guided me to address reviewers' comments in the respective topics.
- Assoc. Prof. N.Hadjsaid supervised and guided the research work at the G2Elab.

The submission of the contributions of this work for publication is in progress. The chapterwise publications associated with the thesis where I was the first and corresponding author are listed below.

- Chapter 3 contains the storage design and sizing methodology published in L. Subramanian, V. Debusschere, and H. B. Gooi, "Design and Control of Storage Systems for Voltage Source Controlled Autonomous Microgrids," *2019 IEEE Power & Energy Society General Meeting (PESGM)*, Atlanta, GA, USA, 2019, pp. 1-5, doi: 10.1109/PESGM40551.2019.8973887.
- The cooperative MPC framework proposed in Chapter 4 has been published as L. Subramanian, V. Debusschere, H. B. Gooi and N. Hadjsaid, "A Distributed Model Predictive Control Framework for Grid-friendly Distributed Energy Resources," in *IEEE Transactions on Sustainable Energy*, doi: 10.1109/TSTE.2020.3018913.
- The rate-based MPC framework proposed in Chapter 5 has been submitted as L. Subramanian, V. Debusschere, H. B. Gooi, and N. Hadjsaid, "A Cooperative Rate-based Model Predictive Framework for Flexibility Management of DERs." (Journal submission under review)
- Chapter 6 contains the modal analysis and the islanded microgrid power flow that are published in the conference proceedings below.
 L. Subramanian and H. B Gooi, "Stabilizing Droop Variation of Converter-Connected Generation in Autonomous Microgrids with Virtual Inertia Control," *2018 IEEE Energy Conversion Congress and Exposition (ECCE)*, Portland, OR, 2018, pp. 3746-3753, doi: 10.1109/ECCE.2018.8557936.
 L. Subramanian and H. B. Gooi, "Stochastic Backward/Forward Sweep Power Flow Analysis for Islanded Microgrids," *2018 IEEE Innovative Smart Grid Technologies - Asia (ISGT Asia)*, Singapore, 2018, pp. 48-53, doi: 10.1109/ISGT-Asia.2018.8467763.

28-August-2020

.....

Date



.....

Lalitha Subramanian

To all the curious and seemingly lost seekers

Acknowledgment

Firstly, thanks to my supervisor, Assoc. Prof. Gooi Hoay Beng, for providing me the opportunity to pursue Ph.D. with NTU-IGP under his supervision. He constantly encouraged developing laboratory experiment skills and helped us access state-of-art equipment in our field to aid research. He has always supported me to exercise freedom over my research objectives and direction, without which I could not have built my interest, related skills, and mainly the confidence of performing independent research.

I am highly grateful to Assoc. Prof. Vincent Debusschere, Prof. Nouredine Hadjsaid, Asst. Prof. Alessandro Romagnoli, and Prof. Claude Guet for encouraging and supporting me throughout my joint Ph.D. journey. It has been a challenging yet a great learning experience in terms of time-management and working in two different research groups and environments. They have been particularly supportive in helping me manage thesis submission in the stipulated time despite the COVID-19 crisis.

I am thankful for the all the knowledge-sharing with my colleagues at the Clean Energy Research Laboratory (CERL) during our group meetings. Particularly, Dr. C.S. Lim, Dr. Eddy Foo, Dr. Ujjal Manandhar, and Dr. Wang Bengfei who introduced me to the OPAL-RT real-time simulator and helped me with my experiments at CERL in NTU. I am glad for the experience of working with Dr. Sathish Kumar on a lab prototype which helped me learn building the hardware from scratch.

I would like to thank Ms. Huang Minying, Ms. Lilly Lim Seok Kim, Ms. Lim Chia Huei, Dr. Bahulayan Damodar, and all the IGS staff for their timely support with administrative requirements. I would like to thank Mdm. Chia-Nge Tak Heng and Ms.

Lin Zhiren at CERL. I thank EarthlinkNTU, NTUGSC, TEDxNTU, IGS-SC, and my fellow NTU-PHP confidants for making my Ph.D. journey more than just research in Singapore.

I highly appreciate the efforts of Dr. Audrey Moulichon, Mr. Cedric Boudinet, and Mr. William Norris at the FLIRT facility and Mr. Antoine Labonne at the PDE-PREDIS facility, without which my experiments at G2Elab would not have been possible. I thank Mamadou and Audrey for helping me with the practical difficulties in Grenoble, not to forget the daily Français lessons, and all the SYRELchunians for making research and office so much fun and making me feel at home in Grenoble.

I am highly grateful to my parents and Shanks for being my team in all my journeys and my dear friends and family for being a part of my adventure. I thank my teachers whose words remain a constant drive to better myself.

Finally, thanks to NTU and the SINERGY Joint-Ph.D. programme for the financial support provided to support this research.

Abstract

The electric power system has been traditionally energised by synchronous machines like steam turbines, hydro turbines, and diesel engines. These rotating machines inherently contribute to the system resilience by providing rotational inertia. The grid frequency is indicative of the real-time power balance across the grid and can be treated as one of the primary grid health indices. On the occurrence of a fault, inertia helps the frequency to *gradually* deviate from the nominal value, i.e. the higher the amount of inertia, the slower is the rate of frequency deviation. The presence of an adequate inertia therefore provides the liberty of allowing a control delay for the governor-input valve controls to respond to the frequency deviation.

With the displacement of synchronous machines by converter-connected distributed intermittent renewable sources such as solar PV and wind turbine systems, the reduction of inherent system inertia is evident. However, there is also a counterpoised observation that the required amount of inertia in the transformed power system is reduced, given the faster response of the converter-based DERs. Therefore, the solution is to resort to synthetic inertia to improve the resilience of the power system, or to faster primary frequency response to improve the system reliability with the limited resilience of a low-inertia grid.

In this context, this thesis explores questions such as: What is the adequate synthetic inertia/frequency response capability for a stable power system? How can one quantify the flexibility required to provide this adequate inertia? Does synthetic inertia greater than the adequate level necessarily indicate a higher stability margin? How different is the effect of *distributed* synthetic inertia on the oscillatory stability compared to synchronous inertia?

Firstly, the aspects of flexibility and methods to characterize them for an adequate synthetic inertia and fast-frequency response are addressed. A generalized virtual storage flexibility model has been proposed to quantify the heterogeneous bidirectional flexibilities and their combination to provide a certain level of synthetic inertia. As an illustration, a hybrid energy storage system has been sized for synthetic inertia and fast-frequency response provision in an isolated power system.

The subsequent chapters discuss synthetic inertia and fast-frequency control actuated by PV systems with hybrid energy storage. In this thesis, inverter control has been explored with a complete DC-side model taking into account the effects of PV intermittency, unlike most research works on inverter control that assume a sufficiently large DC source/sink. Synthetic inertia controllers are categorized as grid-following and grid-forming topologies, which significantly affect their impact on system stability. Conventionally, the inertia and damping parameters are tuned and fixed over a scheduled time slot based on the available flexibility. It has been identified that a higher inertia is required on the occurrence of a disturbance to limit the rate of frequency deviation and a higher damping is required for a faster settling time. Therefore, for each of the control topologies, a rule-based real-time inertia tuner has been proposed to optimize the frequency deviation, its rate, and the settling time. The algorithm has been improved through a model predictive control with a rate-based linearization. The rate-based linearization extends the model validity to the transient zones. For systems with multiple grid-formers and multiple frequency responsive units, a distributed optimization problem has been formulated and solved to collectively tune the inertia and damping parameters which are constrained by the available flexibilities.

The efficacy of distributed grid-forming and grid-following synthetic inertia in replacing their synchronous counterpart in a microgrid has been compared. Microgrid regulation in grid-connected and islanded modes have been studied by modelling the DERS with discussed control strategies. The impact of the two types of synthetic inertia controls on the small signal stability of the system are examined by modal analysis and bifurcation plots to derive the conditions for oscillatory stability in a microgrid with distributed synthetic inertia reserves. The effectiveness of the proposed control strategies in restoring

the frequency stability of low-inertia systems has been validated by power hardware-in-the-loop experimentation.

Contents

Acknowledgment	i
Abstract	iii
List of Figures	xi
List of Tables	xiii
Abbreviations and Nomenclature	xv
1 Introduction	1
1.1 Background Information	1
1.1.1 Global Energy Scenario	1
1.1.2 Electricity Generation Mix	4
1.1.3 Concept and Architecture of Microgrids	6
1.2 Motivations	7
1.3 Research Objectives	9
1.4 Contributions	10
1.4.1 Experimentation	11
1.5 Summary	12
2 Literature Review	13
2.1 Microgrid Control	13
2.1.1 Relevant Standards	14
2.1.2 Classification of IBRs	15
2.2 Load Frequency Control	16
2.2.1 VI and FFR	17
2.2.2 IBR Control Topologies for LFC	19
2.2.3 Strategies for Parameter Adaptation	22
2.2.4 Cooperative Schemes	25
2.3 Modelling and Sizing Flexible Resources	26
2.3.1 Hybrid Energy Storage Systems	27
2.3.2 ESS Sizing Methodologies	28
2.4 Small Signal Stability Analysis	28
2.4.1 Power Flow Analysis of IMG	29

2.4.2	SSS Conditions on Frequency Response Parameters	31
3	Modeling and Sizing Flexible Resources for Frequency Response	33
3.1	Desired Frequency Response Characteristics	33
3.1.1	International Grid Codes on Frequency Containment	34
3.2	ESS for Frequency Response	36
3.2.1	Hybrid Energy Storage Systems	37
3.2.2	HESS Control	38
3.3	DER and Load Flexibility for Frequency Response	40
3.3.1	Frequency Responsive PV Control	40
3.3.2	Frequency Response with Controllable Demand	41
3.3.3	Virtual Battery Model of Heterogeneous DERs	42
3.4	ESS Sizing for Frequency Response	43
3.4.1	PFR with ESSs	44
3.4.2	Sizing Flexible Resources for Inertial Response	45
3.4.3	Illustration	47
3.5	Chapter Summary	48
4	Coordinated MPC Framework for Grid-following DERs	49
4.1	Grid-following Control	49
4.1.1	Grid-supporting Control	50
4.2	Local MPC Control	51
4.2.1	Model Predictive DC-DC Control	53
4.2.2	Model Predictive Inverter Current Control	56
4.2.3	Model Predictive Inertia Tuning	58
4.3	Coordinating Frequency-Responsive DERs	61
4.3.1	System Model	62
4.3.2	Consensus-based Coordination	64
4.4	Results and Discussion	66
4.4.1	System Description	66
4.4.2	Validation	68
4.5	Chapter Summary	77
5	Coordinated Predictive Control of Grid-forming DERs	79
5.1	Isochronous Grid-forming Control	80
5.1.1	Control Implementation with MPC	80
5.1.2	Synchronizing Control for Microgrid Transition	83
5.1.3	Coordinating Isochronous Grid-formers	84
5.2	Grid-forming Droop Control	86
5.2.1	Droop Laws with System Impedance	88
5.2.2	Virtual Impedance	89
5.2.3	Active damping	90
5.2.4	Inertia Emulation	91
5.3	Coordinated Predictive Framework	92

5.3.1	System Model	94
5.3.2	Rate-based Linearization of the Model	96
5.3.3	Cooperative MPC Framework	97
5.4	Results and Discussion	98
5.4.1	Isochronous Grid-forming Control	98
5.4.2	Droop Control in Resistive Microgrids	99
5.4.3	Synchronization Control for Microgrid Transition	102
5.4.4	Cooperative Predictive Droop Control	102
5.5	Chapter Summary	107
6	Small Signal Stability of IBR Microgrids	109
6.1	Small Signal Modelling	109
6.1.1	Modelling Inverter based Resources	110
6.1.2	Overall System Model	112
6.2	Power Flow for Islanded Microgrids	115
6.2.1	Deterministic Power Flow Analysis of Islanded Microgrids	115
6.2.2	Stochastic Response Surface Formulation	119
6.2.3	Illustration with Benchmark System	125
6.3	Modal Analysis	128
6.3.1	Clustering Eigenmodes	128
6.3.2	Impact of Parameter Variation on Eigen Traces	130
6.3.3	Interaction of Droop and Inertia Controllers	132
6.3.4	Design of Active Damping Parameters for SSS	133
6.4	Deriving Stability Limits for Droop Parameters	136
6.5	Chapter Summary	138
7	Conclusion	139
7.1	Research Outcomes	139
7.2	Recommendations for Future Works	141
	Bibliography	143
	References	143
	List of Publications	162
	Résumé de la Thèse	163

List of Figures

1.1	Evolution of Global Temperatures and Renewable Capacity.	2
1.2	Evolution of Singapore Energy Mix.	2
1.3	PV Generation Capacity [1].	3
1.4	PV Output Variation on an Average Day, Recorded per minute.	4
1.5	Impact of Synchronous Inertia on Frequency Response.	5
1.6	Hierarchical and Plug-and-play Control Structure.	6
2.1	Stages in Frequency Control.	17
3.1	Frequency Response Metrics.	34
3.2	Comparison of Storage Technologies.	37
3.3	Frequency Response Control with ESS.	39
3.4	Frequency Responsive PV Control.	41
3.5	3-node 100% IBR Microgrid.	47
4.1	Grid-following Control.	50
4.2	Proposed Control Scheme of a Grid-friendly DER.	52
4.3	MPC DC-DC Control Schematic.	53
4.4	MPC Inverter Control Schematic.	56
4.5	Control Structures for DERs as Multi-Agent Systems.	61
4.6	Modified CIGRE Benchmark Microgrid System.	67
4.7	Effect of the Synthetic Inertia on the System Dynamics.	69
4.8	Synthetic Inertia. Illustration of the Need for MPC.	70
4.9	Distributed Predictive Synthetic Inertia Control.	71
4.10	Response Characteristics of the Hybrid Energy Storage.	71
4.11	Comparison with other Controllers.	72
4.12	MPC Performance with Flexibility Constraints.	74
4.13	Non-uniform Frequency Control Dynamics among DERs.	75
4.14	PHIL Validation.	76
4.15	HESS Response Simulating PV and Load Disturbances.	77
5.1	Isochronous Grid-forming Control.	81
5.2	MPC Scheme for Isochronous Grid-formers.	81
5.3	IBR Multi-mode Control for Microgrid Transition	83
5.4	Inverter Droop Control Schematic.	87
5.5	Droop and Inertia Emulation with MPC Tuner	93

List of Figures

5.6	Schematic Diagram of the Local MPC.	94
5.7	Cooperative MPC Framework.	98
5.8	PHIL Experimental Setup	99
5.9	Isochronous Grid-former Response.	100
5.10	Operation of IBR in Different Modes.	101
5.11	Effect of R_v on Power Sharing Accuracy and Response Time.	102
5.12	Synchronization Control for Microgrid Transition.	103
5.13	Interdependence of Droop and Damping Parameters.	104
5.14	PFR and IR with ESS-based DERS.	105
5.15	Frequency Response of Parallel DERS	106
5.16	Grid-forming MPC Droop and Inertia Control Response.	106
6.1	3-IBR Islanded Microgrid.	113
6.2	Steps for Stochastic Power Flow.	124
6.3	Stochastic Power Flow Results.	127
6.4	Clustering the Eigenmodes of IBR Microgrid.	129
6.5	Effect of m_p Variation.	130
6.6	Effect of n_q Variation.	131
6.7	Interaction of Droop and Inertia Controllers.	133
6.8	Effect of Variation of Active Damping Parameters in IDCs.	135
6.9	Effect of Variation of Active Damping Parameters in Inertia Controllers.	136

List of Tables

2.1	Comparison of selected VIE topologies	23
3.1	Grid Codes on Frequency Containment.	35
3.2	ESS Sizing for PFR and IR.	48
4.1	Buck-Boost Converter Outputs.	55
4.2	Virtual Battery Model Parameters.	67
5.1	Droop Relations for Different System Impedances.	89
6.1	3-IBR Microgrid Initial Steady State Values.	125
6.2	Comparison of the Performance of SRS Method and MCS.	125
6.3	33-bus Microgrid - Droop-based BFS Power Flow Solution.	126

Abbreviations and Nomenclature

A. Abbreviations

AGC	Automatic Generation Control
BESS	Battery Energy Storage System
BFS	Backward Forward Sweep
CCS	Carbon Capture and Sequestration
CDF	Cumulative Density Function
CM	Cumulant Method
CP	Collocation Point
CSP	Concentrated Solar Power
DER	Distributed Energy Resource
DERMS	Dynamic Energy Resource Management Systems
DFIG	Doubly Fed Induction Generator
DG	Distributed Generation
DMPC	Distributed Model Predictive Control
DPFA	Deterministic Power Flow Analysis
ESS	Energy Storage System
EV	Electric Vehicles
FCS	Finite Control Set
FESS	Flywheel Energy Storage System
FFR	Fast Frequency Response
GHG	Greenhouse Gases
GJ	Gauss-Jacobi Weighted Sum Transformation
HESS	Hybrid Energy Storage System
HVAC	Heating Ventilation and Air Conditioning
IBR	Inverter Based Resources
IDC	Inverter Droop Control
IEA	International Energy Agency
IMG	Islanded Microgrids

IR	Inertia Response
LFC	Load Frequency Control
LQR	Linear Quadratic Regulator
LTI	Linear Time-invariant
MCS	Monte Carlo Simulation
MG	Microgrid
MPC	Model Predictive Control
MPP	Maximum Power Point
MPPT	Maximum Power Point Tracking
NDC	Nationally Determined Contribution
p2p	Peer-to-Peer
PDF	Probability Density Function
PDF	Probability Density Function
PEM	Point Estimate Method
PFA	Power Flow Analysis
PFR	Primary Frequency Response
PHIL	Power Hardware-in-the-loop
PID	Proportional Integral Derivative control
PLL	Phase Locked Loop
PnP	Plug and Play
SCCESS	Super Capacitor Energy Storage System
SFR	Secondary Frequency Response
SI	Synchronous Inertia
SM	Synchronous Machines
SMES	Superconducting Magnetic Energy Storage
SOC	State of Charge
SPFA	Stochastic Power Flow Analysis
SRS	Stochastic Response Surface
SSS	Small Signal Stability
TLC	Thermostatically Controlled Loads
UFLS	Under-Frequency Load Shedding
VBM	Virtual Battery Model
VIE	Virtual Inertia Emulation
VOC	Virtual Oscillator Control
VPP	Virtual Power Plant
VSG	Virtual Synchronous Generator
ZPP	Zero Power Point

$(df/dt)_{max}$	Maximum allowable ROCOF in Hz/s
α	Connectivity matrix of the DER communication network
l	Laplacian matrix of the DER communication network
w	Weight matrix of the DER communication network
Δf_{ss}	Quasi-steady state frequency deviation in Hz
ΔP_d	Power imbalance due to disturbance in the system in p.u.
ΔP_{d-max}	Power imbalance due the worst case contingency
δ	Duty cycle of the converter control
η_c, η_d	Charging and discharging efficiency of ESS in %
γ_1	Kurtosis
γ_1	Skewness
λ	Power-frequency characteristics of the system
μ	Probabilistic mean
ϕ_d	Angle difference for disconnection synchronization
ϕ_r	Angle difference for reconnection synchronization
σ^2	Probabilistic variance
θ	Voltage phase angle
ζ	Damping ratio
$bcbv$	Nodal current-nodal voltage matrix
$bibc$	Nodal injection-nodal current matrix
C_{min}, C_{max}	SOC limits of ESS in %
D	Damping coefficient in p.u.
d_s	Self-dissipation rate of ESS in s^{-1}
E^-, E^+	Energy capacity limits of ESS in kWh
E_{pfr}, E_{ir}	Estimated energy ratings of the ESS for PFR and IR respectively
f_0	Nominal steady state frequency in Hz
f_{nadir}	Extrema of the frequency transient in Hz
H_m	Hermite polynomial of m^{th} order
H_s	System inertia constant in s
J	Moment of inertia in p.u.
K_d	Damping control gain
K_i	Inertia control gain
m_p	Active power-frequency droop
m_{ess}	Designed PFR droop characteristic

Abbreviations and Nomenclature

N	Number of time intervals in the prediction horizon of MPC
N_c	Number of time intervals in the control horizon of MPC
n_q	Reactive power-Voltage droop
P^-, P^+	Power capacity of ESS in kW
$rocof$	Rate-of-change-of-frequency in Hz/s
S_{pfr}, S_{ir}	Estimated power ratings of the ESS for PFR and IR respectively
T_r	Time of delay of response by ESS in s
T_s	Control step time in s
$W(x)$	Lyapunov function
Y	Admittance matrix
Y_r	Power flow response vector
Z	Collective decision variable of the consensus algorithm

Chapter 1

Introduction

1.1 Background Information

1.1.1 Global Energy Scenario

As a response to the threat of global climate change, 189 states have joined the party to the 2016 Paris agreement. Each of these states are committed to reducing their greenhouse gas emissions as per their enlisted nationally determined contributions (NDCs) with a maximum estimated increase of 1.5°C in global temperature. However, the estimated global increase in temperature based on the signed NDCs project a global emission level of 55 gigatonnes corresponding to a temperature increase much beyond 2°C [2]. Thus noting that even if the NDCs are met, much greater efforts will be required for an emissions target of 40 gigatonnes corresponding to 2°C . Currently the human induced increase in temperature of about 0.2°C every decade as shown in Fig. 1.1a, assuming that reductions in emissions were to begin immediately and reach zero by 2055.

Electricity production being one of the main contributors of greenhouse gas (GHG) emissions, the average CO_2 intensity in the global electricity supply is currently $504 \text{ gCO}_2 \text{ kWh}^{-1}$, whereas the targetted CO_2 emission estimate for the 2°C criterion in 2050 is $15 \text{ gCO}_2 \text{ kWh}^{-1}$ [3]. To address this large gap and the necessary transformation in

power production, several countries around the world are investing on new installations of renewable energy technologies, with solar PV installations increasing over the last decade as shown in Fig. 1.1b. As this thesis was started in Singapore, the Singapore emissions and energy scenarios are described below.

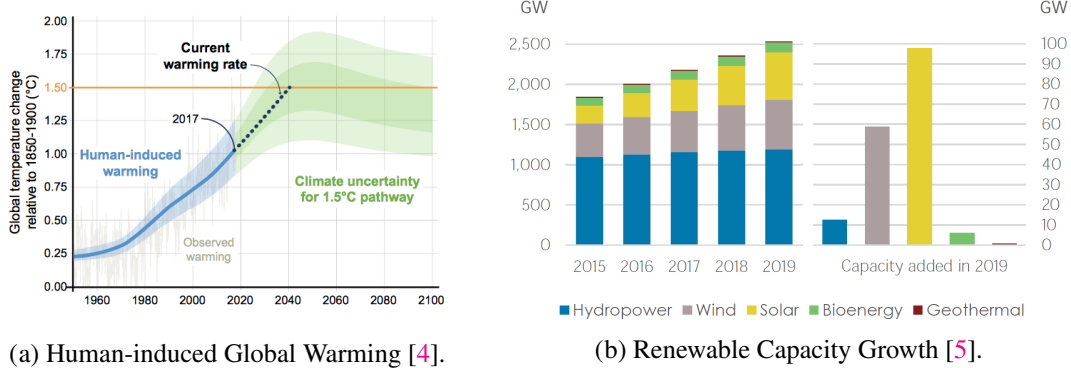


Fig. 1.1: Evolution of Global Temperatures and Renewable Capacity.

1.1.1.1 Singapore Context

Singapore ranks 27th in the global per capita emissions based on the 2018 International Energy Agency (IEA) report, with its emissions per capita showing a steep increase over the years of steep gross domestic product (GDP) growth. Singapore ratified the Paris agreement by committing to a 36% emission reduction over GDP from the 2005 levels, which is estimated as 0.176 gCo_2eq/SGD by 2030. The Singapore government has also indicated to update its NDC to peak at 65 $MtCO_2eq$ in 2030. The energy mix of Singapore is shown in Fig. 1.2 [1].

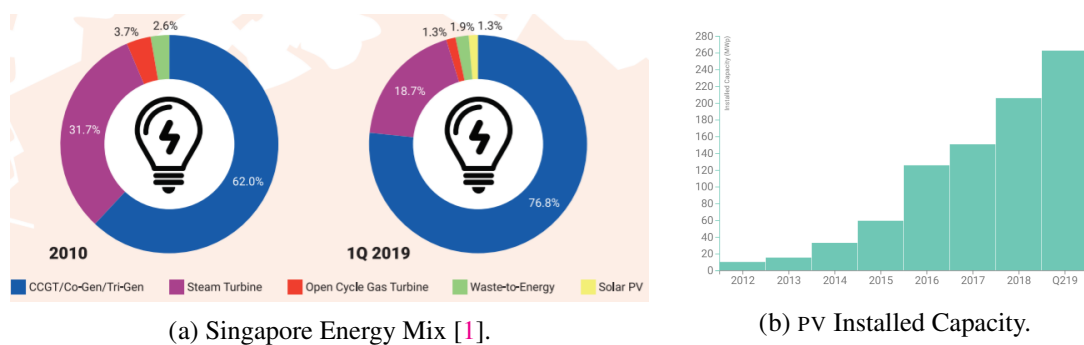


Fig. 1.2: Evolution of Singapore Energy Mix.

Based on the IEA 2018 report, the energy sector in Singapore amounts to 38% of the emissions, fuel combustion from the industries 40%, transport sector 14%, buildings and waste management upto 2%. As a response to these emissions target, the National Climate Change Secretariat of Singapore, has introduced a carbon tax of \$5/ tCo_2eq upto 2023 targetting large emitters to shift to renewables. However, a higher carbon tax is required to incentivise a significant shift to decarbonising the energy and industry sector. The energy sector being the main contributor of the emissions, renewable expansion in terms of solar PV has been growing over the last decade. Singapore is a geographically small island with relatively flat landscape, low-winds, small land area with high population density, which leaves it with solar PV as the only economical renewable energy avenue. Therefore, Singapore is currently focussing on expanding its PV penetration level. The regionwise PV generation capacity is shown in Fig. 1.3.

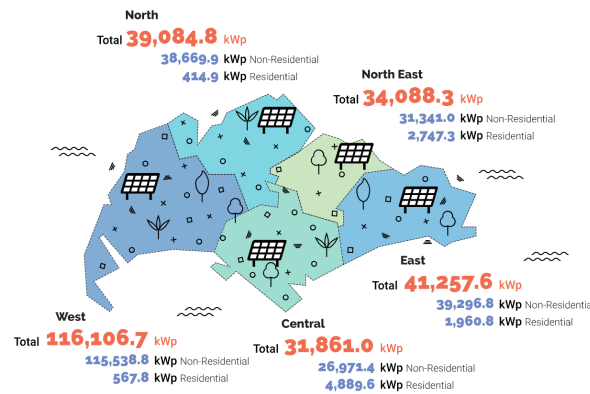


Fig. 1.3: PV Generation Capacity [1].

The main hindrances to PV deployment in Singapore is its high intermittency. Fig. 1.4 shows the PV output with a 10 kWp installation and the aggregated output of 10,000 such units. The high intermittency of renewables challenges the conventional methods used for power system planning and operation, which are only designed to handle unidirectional load intermittencies. Unlike the conventional load-following methods of generation control, there is a need for a generation and load following approach, which requires sufficient predictability and flexibility services that buffer such fast changes in the power production and consumption. Therefore, a need arises for a reliable system for integrating a large number of intermittent PV systems whilst secure the grid stability, which is the main drive of this work.

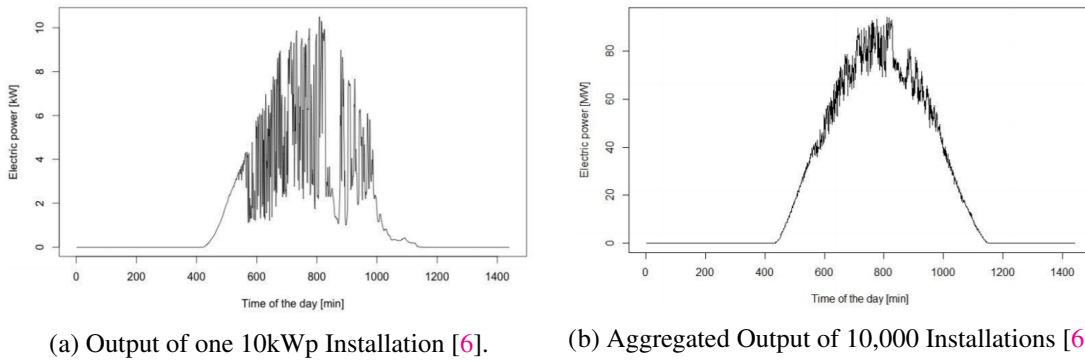


Fig. 1.4: PV Output Variation on an Average Day, Recorded per minute.

1.1.2 Electricity Generation Mix

The conventional electricity generation mix mainly comprises of dispatchable generation including coal-fired thermal, natural gas, and nuclear power plants; all of which are non-renewable, including the nuclear plant based on the argument that the Uranium-235 resources are limited. On the other hand, dispatchable renewable generation includes hydro, biomass, geothermal, concentrated solar power (CSP), and ocean thermal power plants, while PV, wind turbine generators and tidal are non-dispatchable or intermittent, carbon neutral renewable energy contestants. The carbon emissions of the coal and natural gas power plants with 90% carbon capture and sequestration (CCS) are 86 and 36 $gCO_2 kWh^{-1}$ respectively, with an additional 7-21 $gCO_2eq kWh^{-1}$ from the CH_4 emissions in the mining process [3]. Considering the energy required for the construction and operation of the plant, the specific GHG emissions of coal, gas, hydropower, and biomass plants (78-109 $gCO_2eq kWh^{-1}$) are significantly higher than those of the nuclear, wind, CSP, and PV production (3.5-11.5 $gCO_2eq kWh^{-1}$) [3], thus favouring the growth of PV and wind plants on a large scale. In this work, we have mainly focussed on the integration of PV systems in the distribution network.

1.1.2.1 Inverter-based Resources

Solar PV and wind-energy systems are connected to the AC power grid through converters, whereas the gas turbines, steam turbine-generators, and diesel generators are synchronous machines (SMs) that are directly connected to the AC grid. The rotating

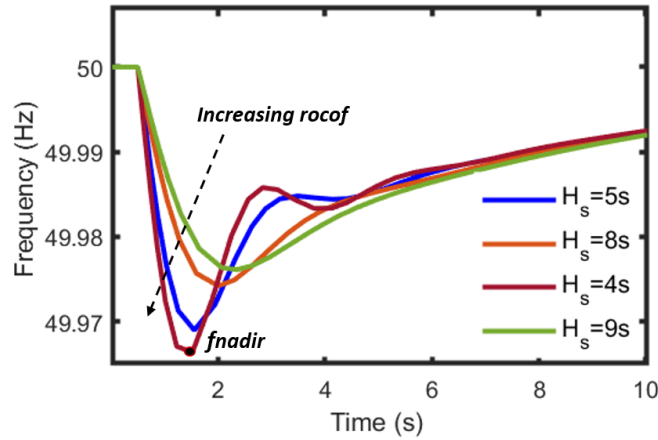


Fig. 1.5: Impact of Synchronous Inertia on Frequency Response.

machines in the power systems inherently possess inertia in the form of stored kinetic energy that resists the changes in the system. Thus, disturbances in the power system do not affect the synchronous torque immediately as the machines continue to dissipate their stored kinetic energy to maintain the power balance. This causes the grid frequency, the power balance indicator, to decrease *gradually* on the occurrence of a contingency. Fig. 1.5 shows that the effect of system inertia H_s on the rate of frequency deviation ROCOF. The lowest or highest point of frequency deviation is referred to as f_{nadir} . The inherent synchronous inertia therefore buys time for the primary frequency controls to respond without challenging the grid stability.

With the high displacement of SMS with inverter-based resources (IBRs) such as PV plants, there is no stored kinetic energy that instantaneously acts on the occurrence of a disturbance. This causes the rate-of-change-of-frequency to be very high, which can trigger the designed power system protection. Synthetic inertia therefore becomes an obligatory ancillary service in the low-inertia power system. It is to be noted that, high renewable penetration, does not necessarily mean a low-inertia system. A low-inertia system is a system with less or no synchronous machines, with numerous power electronics interfaced components. To compensate for the lack of inertia, energy storage or other rapidly-controllable flexible components may be utilized. The control strategy that emulates synchronous inertia in converter-interfaced DERs is referred to as synthetic inertia control[7]. On the other hand, the lack of inertia can also be tackled by implementing a very fast primary frequency response (PFR) using the rapidly-controllable

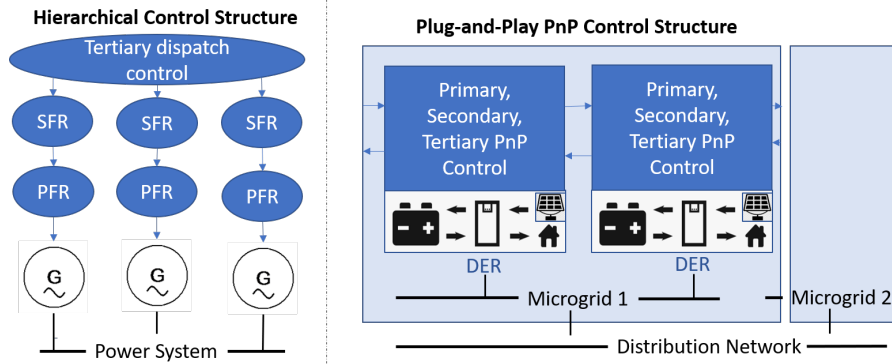


Fig. 1.6: Hierarchical and Plug-and-play Control Structure.

flexible components. This is known as fast-frequency response (FFR) [7]. In this thesis, we explore the control strategies and flexible components for emulating synthetic inertia and FFR for a resilient inverter-dominated power system.

1.1.3 Concept and Architecture of Microgrids

Unlike large centralized generation, distributed energy resources (DERs) supply the local demand, which leads to the concept of microgrids (MGs) and virtual power plants (VPPs). MGs serve as a concept to integrate a distributed generation and is referred to as building blocks of a smart grid [8]. They are independently controlled systems capable of operating in grid-connected and autonomous modes, typically located at the LV distribution level with DERs, ESSs, and flexible demand, which when coordinated efficiently brings definite advantages to the system operation. VPPs on the other hand are not restricted to the same local network. Unlike MGs, VPPs are a collection of DERs that are controlled by a centralized entity over a large geographical area like an aggregated production [8]. With numerous DERs interacting to form a microgrid, and with different microgrids interacting to form a local distribution network, power system is transforming to a nested control architecture, which largely requires plug-and-play control structure replacing its hierarchical counterpart as shown in Fig. 1.6.

Microgrids have existed in the past in remote islanded applications, where building transmission corridors was not economically viable, such as in islands, military bases, etc.

However, with the motivation of self-consumption in the energy policies of many countries using household solar power has led to local energy community microgrids that use local energy management systems [9].

1.2 Motivations

Decentralized energy production, consumer co-ownership, and development of the buffer ESSs have been driving changes in the energy policies over the last decade [10, 9]. Self-consuming energy communities development initiatives are being introduced in the recent European renewable energy directive (RED II) 2018, in which the 28 member states have to transpose into the national energy policies by June 2021 [11]. The idea of collective self-consumption is modular and revolves around the idea of a sharing economy, where under-utilized resources under individual ownership are shared for the benefit of the community in exchange for energy or monetary benefits [12].

With the growing popularity of self-consumption, firstly there is an imminent the need for identifying, quantizing, and controlling the heterogeneous aggregated flexibility options for the different levels of balancing control in the local community. One of the main tasks of the power system operations is the balancing load frequency control (LFC) that responds to the dynamic characteristics of the load and minimizes deviations in the system frequency, which is the indicator of the active power balance in the system [13]. The aggregated generation must supply the overall electrical loads and the losses involved in transporting the electricity to the loads via the transmission and distribution lines to maintain the power balance. The conventional electric power system has been a network of highly dynamic loads supplied by controllable generation. Therefore, frequency controls are primarily implemented as *load-following* automatic generation control (AGC) strategies [14, 15]. However, with an increase in the intermittent generation ratio in the power system, the load variation is coupled with the intermittency of PV generation rendering the AGC unreliable to maintain the power balance. In a power system with very high penetration of intermittent non-dispatchable generation, load-following operation and control becomes obsolete. Thus, for the operational feasibility of the system,

there is a need for sizing and control of flexible resources for the balancing control such as: dispatchable DERs like microturbines and fuel cells, energy storage systems (ESS) [16, 17, 18], PV/wind curtailment [19, 20, 21], and generation-following load controls (demand response) [22, 23, 24], and load curtailment [25].

Secondly, newer control frameworks have to be developed and tested for the reliable operation of power systems with a large share or 100% IBRs. Traditionally, the synchronous generators with the governor systems provide an implicit inertia and primary frequency support in the conventional power system, which restricts the steepness of the frequency derivative and the frequency deviation respectively. Smaller independent power systems have an evidently lower inertia, due to which its reliable operation with intermittent converter-interfaced DERs is very challenging. Reduced inertia and fast-frequency reserves in these systems are compensated by dedicated inverter-connected storage units, controlled as grid-following virtual inertia controllers [26], grid-forming droop controllers [27, 28], and virtual synchronous generators [29]. Grid-forming units serve as the primary voltage source of the microgrid during autonomous operations, while grid-following units depend on the main grid or the grid-formers to serve as the voltage reference.

In the context of microgrids/energy communities, the installation of a dedicated storage capacity for fast-frequency response may not be an optimal solution [12]. So, there is a need for both grid-forming and grid-following control strategies that utilize distributed time-varying flexibility resources in the community grid to perform the fast-frequency control actions. Unlike the conventional power system, where a number of machines proportionally share the task of frequency control, the exploitable flexibility in distributed energy resources (DERs) can be time-varying and may or may not be suitable for providing fast frequency response [30]. Hence, the main objective of this work is to develop cooperative fast-frequency and inertia control strategies for an optimal frequency response while addressing the constraints of the available flexibilities in the system.

Finally, the effect of distributed inertia and damping in PFR, FFR, and synthetic inertia

response has to be analyzed for stability from the system perspective. The effect of inertia emulation on the frequency stability enhancement in terms of the f_{nadir} and the ROCOF have been studied in [31, 32]. In addition, a handful of recent studies [33, 34, 35] have shown that the interaction of inertia emulators and droop-controlled IBRs may lead to new oscillatory modes, which if left undamped may lead to oscillatory instability. Considering systems with synchronous and synthetic inertia, a new power oscillation against the SMS in the same area is induced by the inertia control. At a higher value of virtual inertia, this oscillation may become unstable [33]. This is a very interesting observation that shows that inertia emulation beyond a prescribed level may have an adverse impact on the power system oscillations. Therefore, there is a need to derive the small signal stability constraints in systems with frequency-responsive IBRs.

1.3 Research Objectives

The overall aim of this research is to investigate the relevance of traditional inertia-droop concepts from a system perspective in the context of inverter-dominated power systems and their stability, with particular interest in the case 100% inverter-based resources (IBR) in a microgrid operating with no synchronous inertia. As the 100% IBR microgrids are futuristic, there is a lack of rigorous standards for their regulation. Listed below are the main research objectives.

1. To study the energy mix and characterise the different flexible resources that can deliver balancing services in a potential flexibility reserve market. The interesting challenge here is to quantify and aggregate the heterogeneous flexibilities to fit a generalized flexibility model to define the actuator constraints by accounting for the control boundaries of the individual DERs.
2. To rigorously study and compare the effectiveness of current-controlled (grid-following) and voltage-controlled (grid-forming) inertia emulation strategies to displace synchronous inertia by monitoring the frequency response characteristics.

3. To explore predictive control strategies for frequency response beyond proportional-derivative i.e. droop-inertia approach for converter-based microgrids and implement them in a power hardware-in-the-loop test bench.
4. To study the interaction of optimal control strategies implemented on grid-forming and grid-following DERs and to develop a resilient regulation strategy for 100% inverter-based power systems that fit a plug-and-play control architecture, unlike the common hierarchical approach.
5. To examine the oscillatory stability of the system devoid of synchronous inertia with frequency responsive inverter-based resources.

1.4 Contributions

The main contributions of the thesis to the energy research community is as follows. Each of these contributions are elaborated in the corresponding main chapters of the thesis.

1. Chapter 3 presents a sizing methodology to design the supplementary storage flexibility required meet a set of desired frequency response characteristics in addition to the available heterogeneous flexibilities such as dispatchable resources, demand response, and renewable curtailment options.
2. A cooperative predictive grid-following frequency response control scheme has been proposed in Chapter 4. It tunes the inertia and damping parameters in real-time based on the control constraints obtained by the coordination of available resources through a consensus algorithm. The proposed control and regulation scheme has been tested on the power hardware-in-the-loop (PHIL) test bench.
3. An isochronous grid-forming control has been implemented using model predictive control (MPC) strategy in Chapter 5. A power sharing algorithm for coordinating multiple isochronous IBRs has been presented.

4. The conventional droop-based grid-formers have been improved by a rate-based MPC in Chapter 5. The rate-based linearization of the MPC extends the model validity to transient zones. The control has been implemented in a multi-converter setting accounting for the transition between interconnected and islanded operation modes of the microgrid.
5. In Chapter 6, a stochastic backward/forward sweep power flow method has been proposed for obtaining the steady-state operating points of the islanded microgrid with droop control. The small signal model of an 100% IBR microgrid with grid-forming and grid-following controls has been presented and the eigen modes have been analyzed to examine the oscillatory stability of the IBR microgrid. The stability criteria derived from the small signal analysis are reflected on the proposed optimal control strategies.

1.4.1 Experimentation

PHIL experiments using the OPAL-RT[®] real time simulator, dSpace[®] controller, and power amplifier, have been an integral part of this work for validating the proposed control strategies and microgrid regulation framework. The power system considered in this work is a 100% inverter-based microgrid. Modelling such power systems with a large number of power electronic devices for real time simulation is a challenge as the system consists of a large number of controlled components with switches, while the control of power electronics has to be sufficiently fast. The microgrid component is present as a hardware, controlled by the proposed regulation strategy programmed in the dSpace[®] controller, while the rest of the microgrid is emulated by the OPAL-RT[®] - power amplifier setup. This experimental design allows us to test the response of the component to various critical system scenarios that can be simulated.

1.5 Summary

In this chapter, the topics covered in the thesis have been introduced with a description of the background information and motivations that lead to the objectives of the research. The contributions made by the thesis have been described briefly with a short note on the experimental setup. The following chapter reviews the state of art in sizing and control of flexible IBRs for synthetic inertia and frequency response, and their interaction and impact on the system stability.

Chapter 2

Literature Review

This chapter introduces the definitions and theories of the different topics covered in this thesis and the review of the corresponding state of art.

2.1 Microgrid Control

MGs are LV distribution networks with DERs, ESSs, and loads capable of operating autonomously from the main grid. The autonomous operation maybe due to a planned islanding or due to a fault in the utility grid, or any other emergency events [36]. With the intermittency of distributed generation, the autonomous mode of operation particularly experiences frequency fluctuations [37]. DERs generate DC power (PV, ESS) or variable frequency AC (DFIG wind generators, microturbine) and are connected to the distribution system using DC-AC inverters. These inverter-based resources (IBRs) must be controlled cooperatively for voltage/frequency regulation and energy management tasks. Dynamic energy resource management systems (DERMS) [38] and MG control architectures may be centralized with a MG controller [39, 40, 41, 42], distributed with a peer-to-peer communication network [43, 44, 45, 46], or completely decentralized [47, 48, 28].

The control hierarchy comprises the primary, secondary, and tertiary control layers through which the operating point is stabilized. The foundation of hierarchical control

stems from the control of transmission systems. However, the control challenges and architectural limitations of microgrids are diverse [36], and therefore require controllers that can adapt in real time to the variability of load and network conditions, which, in other words, refer to controls that are suitable for plug-and-play (PnP) operation to seamlessly operate without separation of time scales.

2.1.1 Relevant Standards

The **ANSI/ISA-95** standard is the general standard for developing an automated interface between the enterprise and the control system [43], which provides the foundation and theory of multilevel hierarchical systems with the highest level being the enterprise level and the lowest level being the device and actuation level. The higher levels provide supervisory control over the lower level, i.e. the higher the control level, the lower is the control bandwidth to ensure that the reference signal of the higher level has low impact on the stability of the lower control level. Adapting the ISA-95 to MGs leaves us with the following control layers.

1. DC-side control - Control of DC-DC buck-boost converters coupling the PV unit for MPPT or curtailment control and the control of buck-boost converters of energy storage systems to regulate the DC-bus voltage compensating for the intermitencies.
2. Inverter inner control loops - Regulation of output voltage and current of the inverter by feedback/feedforward, and linear/non-linear control.
3. Primary control - The primary control layer could be a grid-forming or grid-following layer. The IBR is controlled as a voltage source for grid-forming operation and as a current source for the grid-following operation. The primary control layer comprises immediate frequency response controls, such as droop and synthetic inertia emulation.
4. Secondary control - Serves as a synchronization and voltage/frequency restoration layer, i.e ensuring that the V/f characteristics in the steady state are within

the respective limits. The synchronization layer allows the transition of the MG operation from grid-tied to islanded modes.

5. Tertiary control - This layer manages the economic dispatch of the DERs during the autonomous operation and manages the power flow between the MG and the main grid or other microgrids during the interconnected operation.

In this work, we extend the adaptation of the microgrid control layers in [43] with the DC-side control layers and the consideration of the actuator limits at the device level by means of the tertiary dispatch control. The grid-forming droop control layer adopted for the primary control layer in [43, 27, 44] is modified to emulate inertia. In case of grid-following operation, the primary layer can still respond to power imbalance with inertia emulation and fast-frequency response (FFR) and act as grid-supporting control. During autonomous operation, the voltage reference for the grid-following IBRs are provided by the grid-formers.

In the grid-connected mode, the grid-interconnection standards such as **IEEE 1547**, **UL 1541** in the U.S., and **VDE 4105**, **RD 1565** in Europe [49], provide the foundations for the interconnections of smart inverters, especially PV units capable of providing grid-support functions.

2.1.2 Classification of IBRs

IBRs in the microgrid may be classified based on the control and operation of the power converters coupling the resources to the distribution network. The terms used for classifying the different types of IBRs and their control strategies in this work are defined in this section.

Grid-following IBRs are controlled as a current source and is dependant on a generator or the grid-voltage, or another voltage-source controlled power converter to operate [50]. Converters controlled as current sources present a high parallel output impedance and are controlled to deliver the reference active and reactive power setpoints. The operation

of the grid-following IBRs are often regulated by a higher level control that determines the power setpoints to be tracked by the inner control loop layer.

Based on the frequency responsive capability, grid-following IBRs are further classified as grid-feeding and grid-supporting/grid-friendly IBRs [50, 51]. If the higher level control is set the reference power settings based on an MPPT control for PV units or based the economic dispatch/tertiary control layer that is scheduled for a desired interval for PV units equipped with ESS, it is defined as a *grid-feeding* DER.

Grid-supporting IBRs on the other hand are those that are capable of adjusting the active and reactive power setpoints to respond to the frequency and voltage deviations. They are controlled current sources with parallel impedance for power sharing that are designed to provide a share of flexible power for regulatory functions [52, 53]. Conventionally, the frequency response of current-controlled grid-supporting inverters are slow since the active power set-point has to be calculated after the measurement of the frequency and sometimes its derivative [54].

Hence, voltage source controlled IBRs known as *grid-forming* IBRs are more appropriate for fast frequency response. The grid-formers are converters capable of controlling the terminal voltage and frequency of the microgrid if the required flexible reserves are available. Grid-forming controls may be implemented as isochronous primary control [55, 56] or droop controllers [47, 48, 27]. Further details on the state of art control strategies are presented in the following section.

2.2 Load Frequency Control

Load frequency control (LFC) is the control of active power balance in the system. With a large share of intermittent distributed generation in the autonomous operation of MGs, frequency regulation is very crucial to assure the stable operation of the MG. The power balance of the microgrid is restored by the control layers acting in different time-scales as shown in Fig. 2.1 [57]. Various control strategies may be applied for the primary frequency control (PFR) and secondary frequency control (SFR).

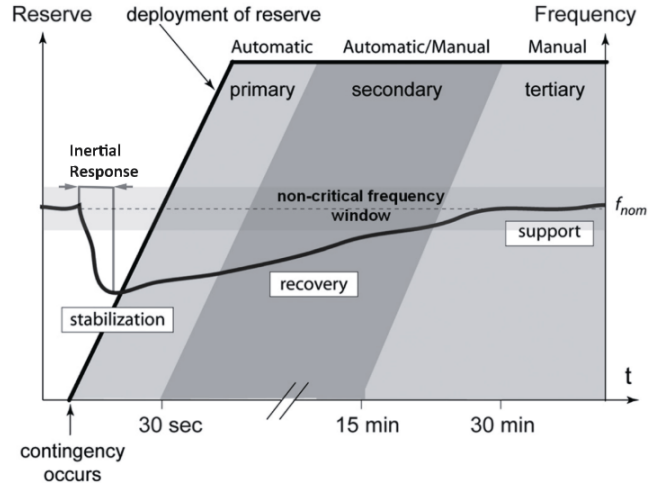


Fig. 2.1: Stages in Frequency Control.

Consider a generation outage that causes the system frequency to drop. The rate of the frequency drop is determined by the synchronous inertia (SI) in the system. SI resists the frequency change until the controllers respond and therefore allows the liberty of control delay in PFR. The higher the SI, the lesser the initial rate-of-change-of-frequency (ROCOF) and the lowest frequency dip f_{nadir} as explained in section 1.1.2.1. The SI a natural consequence of the presence of synchronous rotating machines in the system caused by the stored kinetic energy in synchronous machines is absent in IBRs. Therefore, power systems with a large share of IBRs and 100% IBR microgrids are referred to as low inertia systems. The lack of SI in low-inertia systems may be compensated by virtual inertia emulation (VIE) using other forms of stored energy. Yet another approach is to compensate the lack of inertia by sufficiently faster primary frequency response, known as fast frequency response (FFR). Many studies do not focus on the distinction between synthetic inertia and FFR [58]. For a clearer picture of the different stability enhancing services, synthetic/virtual inertia (VI) and FFR services are defined below.

2.2.1 VI and FFR

To describe VIE, consider the dynamic behaviour of the system with system inertia given by (2.1), where, H_i and S_i refer to the inertia constant and power rating of the i^{th} SM respectively. The swing dynamics of the i^{th} machine is given by (2.2), where

$J_i, \omega_{m,i}, T_{m,i}$ and, $T_{e,i}$ represent the moment of inertia, angular velocity, mechanical, and electrical torques respectively. Further, the swing equation can be written as (2.3), where $H_i, \omega_i, P_{m,i}$ and, $P_{e,i}$ represent the machine inertia constant in seconds, electrical frequency of the machine, mechanical, and electric power of the generator in per unit (p.u.) respectively. For a power imbalance of ΔP due to the disturbance in this system, the initial time derivative of the frequency ROCOF is given by (2.4).

$$H_s = \frac{\sum_{\forall i} H_i S_i}{\sum_{\forall i} S_i} \quad (2.1)$$

$$J_i \frac{d\omega_{m,i}}{dt} = T_{m,i} - T_{e,i} \quad (2.2)$$

$$2H_i \omega_i \frac{d\omega_i}{dt} = P_{m,i} - P_{e,i} \quad (2.3)$$

$$ROCOF = \frac{df}{dt} = \frac{\Delta P f_s}{2H_s} \quad (2.4)$$

Since the inertia emulated is proportional to the ROCOF, ROCOF measurements are necessary for VIE. The ROCOF calculation is challenging as it is susceptible to disturbances and the calculated value depends on the time window over which it is calculated. Yet there is no appropriate standardization for ROCOF measurement and testing [58]. In this work, VI refers to frequency response services emulating the swing equation in (2.3), i.e. the inertia response emulated is proportional to the frequency deviation and its time derivative, whereas faster PFR options that respond with a controlled contribution of electric torque T_e for quick changes in frequency [58], with very short delay in response time are referred to as FFR.

On the other hand optimal frequency response control strategies [59, 60], are not restricted to a proportional-derivative i.e. droop-inertia response and can involve complex control. However, it is interesting to note that a high inertia response restricts the inertia frequency swing due to the disturbance, however, persistent high inertia response leads to a higher peak overshoot and a larger settling time [61]. A higher damping is required once the frequency controls are active to damp the frequency oscillation for a quicker settling time. Therefore, the VI, FFR and damping controls collectively manage the different frequency characteristics. Procuring additional damping reserves to compensate

for the over compensation of the VI and FFR services requires unnecessary investment in additional storage reserves to support each of these services. Hence, in this work we explore optimal adaptation of VI and FFR parameters to avoid the requirement of additional damping services to ensure the stability. The following section reviews the existing FFR and VI control strategies that can be implemented in grid-following and grid-forming IBRs.

2.2.2 IBR Control Topologies for LFC

From the simplest droop control [27] to the recently popular virtual oscillator control [62], there are several notable contributions to the first generation of control topologies for low-inertia systems. Each of these topologies has its own set of merits and demerits and is highly application specific [63]. The control topologies mainly fall under one of the categories described below.

2.2.2.1 Droop based Topologies

Droop-based control adopts the traditional droop control concept of SM [47] is shown to have a slow and inefficient transient response as the response of the control is not proportional to the time derivative of the frequency deviation. With a fast-responding ESS such as supercapacitor bank or flywheel systems, the control can act as an FFR reserve.

The droop control facilitates the autonomous operation of inverter-based microgrids [27, 64] by means of a frequency-active power droop and a reactive-power voltage droop as shown in the equations below [37]. The active power output of the inverter is measured with the help of a low pass filter with time constant T_f . When the low pass filter transfer function is accounted for in the droop equation (2.6), it is inferred that the equivalent inertia and damping contribution of the droop controller are as given in the (2.7). Thus the power measurement delay in the filter along with the droop coefficient m_p contributes to the virtual inertia J and the droop coefficient contributes towards the damping D . The

virtual inertia is not fully controllable and the ratio J/D is constant for a system. Thus, droop controllers tend to have a poor transient response in terms of inertia.

$$\omega_i^* = \omega_n - m_p \left(\frac{P}{(1 + T_f s)} - P_b \right) \quad (2.5)$$

$$P_b - P = \frac{T_f}{m_p} s(\omega_i^*) + \frac{\omega_i^* - \omega_n}{m_p} \quad (2.6)$$

$$J = \frac{T_f}{m_p}; D = \frac{1}{m_p} \quad (2.7)$$

where, ω_i^* is the reference frequency of the inverter i ; ω_n is the grid frequency; P is the active power injected by the inverter and P_b is the base power of the unit.

2.2.2.2 Frequency-Power Response/ Vsync Topologies

Frequency-power response based control technique popularly referred to as *Vsync* [63] or virtual synchronous generators (VSGs) [65, 66, 67], is typically a current-source implementation (grid-following) with inherent over-current protection. However, since the control is based on the frequency derivative, the system may be more susceptible to noise and is slower compared to its voltage source counterparts. In weak power networks, it may also result in instability due to dependence on phase locked loops.

In comparison to the droop controller, *Vsync* topology provides a better dynamic response by sensing the change in frequency and the RoCoF and accordingly responding to it by releasing or absorbing inertial power similar to a synchronous generator as shown in (2.8) where, K_i and K_d are inertia and damping control parameters [68]. Since the frequency and ROCOF measurements are taken from the PLL, this topology relies on the accuracy of the PLL measurements and thus require a robust PLL. PLLs often pose problems in terms of stability in weak grids with harmonic distortions and voltage swell/sag [63]. These conditions will affect the performance of this controller. Another important disadvantage of this control topology is that the controller cannot be implemented for a grid-forming unit as it is a current-controlled implementation based on the PLL measurements.

$$P_{vsg} = K_i \frac{d\Delta\omega}{dt} + K_d \Delta\omega \quad (2.8)$$

2.2.2.3 Swing Equation based Topologies

The swing equation-based topology uses a simpler model of the synchronous generator and does not require the measurement of frequency derivative. It is typically based on a voltage source implementation with phase locked loops which are only used for synchronization. The basic swing equation-based topology was implemented by the Ise lab group in [69, 70, 71]. The inertial response of the synchronous generator is emulated by solving the swing equation using the measured inverter output current and voltage at the point of connection to compute the active power output of the inverter P_{out} and thus calculate the angular velocity of the virtual rotor ω_m using (2.9) by numerical integration. The input power or the prime mover input is defined by a governor model using (2.10) [70, 72].

$$P_{in} - P_{out} = J\omega_m \frac{d\omega_m}{dt} + K_d(\omega_m - \omega_g) \quad (2.9)$$

$$P_{in} = P_{out} + \frac{K(\omega_{ref} - \omega_g)}{1 + T_d s} \quad (2.10)$$

Unlike the previous method, the swing-based emulation can be implemented for grid-forming controllers. The controller does not rely on ROCOF measurements from PLL and is thus more robust to PLL accuracy and noise. However, oscillatory stability issues may arise due to the improper tuning of J and K_d parameters [63]. Since the control is based on the swing equation, the use of this topology may result in power oscillations which have to be damped using a damping controller [73].

2.2.2.4 Machine Model based Topologies

Synchronous generator model-based topologies, popularly referred to as synchronverters try to mimic the actual SM using an accurate model popularly known as synchronverters [74, 75, 76]. Unlike the above swing equation-based topology, the synchronverter

solves the entire synchronous generator equations in every control cycle for a better performance.

The most interesting aspect of the synchronverter is its inherent capability to maintain synchronism with the terminal voltage [77]. The equations of the synchronverter form an enhanced PLL that helps with the auto-synchronism. Thus, it is most-suited for grid forming units in islanded microgrids. However, there is no inherent protection against severe transients because of the voltage-source implementation [63]. It requires additional current protection units to ensure safe operation. Numerical instability is another significant problem associated with this topology due to the high real-time model computation requirement.

2.2.2.5 Oscillator based Topologies

Virtual oscillator control (VOC) emulates the dynamics of coupled non-linear dead-zone oscillators to enable communication-less synchronization and power sharing in a system of parallel inverters [62]. Due to its communication-free auto-synchronizing capability, this control is suitable for islanded IBR microgrids [78, 79]. Droop control being a special type of VOC [80], has clear advantages in the application to low-impedance networks. VOC is also capable of providing a faster transient response as it is a time domain control that reacts to instantaneous power measurements [81], unlike the droop control which relies on average measurements. However, VOC is shown to have a very large settling time with reduced damping and is unable to control the frequency as precise as the droop control.

Table 2.1 presents the comparison of the response of the selected topologies to a 2 kW step load change in a simple 2-inverter microgrid from [82].

2.2.3 Strategies for Parameter Adaptation

In this work, we focus on swing-based VIE and FFR techniques for grid-formers and frequency-power response topology for grid-following IBRs. The main concern in these

Table 2.1: Comparison of selected VIE topologies

No-VI case: $f_{nadir} = 56.9\text{Hz}$, $RoCoF_{max} = 2\text{Hz/s}$, $t_{settle} = 9.2\text{s}$					
	Droop	V_{sync}	Swing-based	Synchronverter	VOC
$f_{nadir}(\text{Hz})$	57.3	58.2	58.4	58.4	57.3
$RoCoF_{max}(\text{Hz/s})$	1.7	1.5	1.4	1.4	1.5
$P_{peak}(\text{W})$	1560	1844	1765	1770	1565
$t_{settle}(\text{s})$	10.1	13.6	12.8	12.9	15.8
Grid-forming	✓	X	✓	✓	✓
Numerical instability	X	X	✓	✓	X
Noise susceptibility	✓	X	✓	✓	✓

topologies is the appropriate tuning of control parameters. Research efforts in the area of fast frequency control and inertia control of microgrids are vast, however relatively very few research efforts have been taken to exploit the controllability of droop and inertia in inverter-based DERs beyond proportional sharing of frequency support responsibilities.

Unlike the implicit inertia property of synchronous machines which is fixed and proportional to the machine capacity, synthetic inertia offered by a converter-based DER can be varied to optimize the frequency response characteristics. Dynamic variation and distribution of the droop and inertia parameters are shown to have an impact on the microgrid stiffness and the small signal stability [83, 37]. Solutions that decouple the droop parameter into a fixed steady-state droop and an adaptive transient droop have been proposed to mitigate low-frequency oscillations [84]. A synthetic inertia control for optimal frequency response in wind power plants has been proposed in [85]. Methods such as bang-bang control [70] and LQR optimization [59] have been proposed for inertia tuning. Moreover, the current attempts on optimizing inertia and damping and the attempts to tune droop parameters based on the required balancing support and power and energy capabilities of the corresponding DERs for loss reduction [86] are not mutually exclusive. The damping parameter and the droop characteristics constrain each other [87]. Hence, there is a trade-off between the local stability and the balancing support provided by the DERs.

It has been shown in [59] that on the event of the disturbance, inertia plays a crucial role in minimizing the transient frequency extrema f_{nadir} , while the damping constant plays a crucial role in optimizing the settling time. Therefore, there is an evident need

for predictive tuning of inertia and damping parameters using model predictive control (MPC) to optimize the frequency response characteristics.

2.2.3.1 Optimal Frequency Response using MPC

Compared to the PID and pole-placement control, MPC control has the inherent ability to handle input/output constraints and predict the evolution of the system over a finite time horizon. The predictive control gives access to the trajectory information, which allows the MPC to conduct an optimization over the prediction horizon, avoiding pre-determined constraints based on safety-margins. The MPC is a receding horizon control that relies on the plant model for the prediction and has proven its superior performance over a PI control in several process control applications.

The authors of [88] have recently shown that the energy storage requirement for synthetic inertia is reduced by the model predictive control (MPC) formulation compared to PI control. However, the MPC control proposed in [88] is only for ESS sizing. MPC has been shown to have a superior performance over the conventional and fuzzy controllers in [60, 26]. An MPC-based active frequency response using wide area measurements in a bulk power system has been proposed in [89]. However in these works, the MPC controller is assumed to be actuated by a dedicated and sufficient ESS, that is operating as a centralized entity for frequency support in the power system. MPC optimization yields the best set of parameters for frequency response, however, in practical applications the control parameters obtained from the MPC is constrained by the limits of the flexibility constraints of the actuator. In a sharing economy with limited resources to be collectively controlled, unconstrained MPC is impractical and needs further research. Methods for coordinated control are discussed in the section below.

While the inertia parameter is optimized by model predictive control in [26, 88], it has been highlighted that the linearized model does not adequately capture the adaptivity of the controller, the problem of simultaneously optimizing inertia and damping parameters. Hence, we attempt to approach this problem with a rate-based linearization. The rate-based linearization for fast-frequency control proposed in this work is inspired from

[90, 91]. The idea of introducing the rate-based model is that the state derivatives are directly propagated through the prediction horizon rather than the states as in a regular jacobian linearization. This in turn holds the model fidelity not only in the near equilibrium region but also in the transient regime.

2.2.4 Cooperative Schemes

With the decreasing cost of storage systems, there is an extensive transformation of the DER capabilities from a passive grid-feeding DER to actively-controllable DERs that can support the autonomous operation of the grid. Grid supporting control and regulations have been widely studied in energy communities with individual storage resources [12]. With the growing number of ESS-based DERs, the possibilities of distributed control of energy storage systems are of recent interest [12, 92]. In this work, we extend the sharing economy principle to DERs in an energy community to collectively perform the tasks of an ancillary service provider.

DERs may be coordinated in a cooperative or competitive manner [12]. Since the problem addressed in this work is a grid-supporting function, the cooperative method becomes an obvious choice for resource coordination. In order to mitigate the need for a centralized authority in every energy community, we aim to coordinate the flexible DERs by formulating a peer-to-peer distributed optimization problem. Distributed control can be performed by methods such as the consensus, game theoretic approaches, and distributed MPC.

Consensus is a distributed average-based cooperative control technique that relies on information-sharing on sparse communication networks. Reference [93] describes a basic asymptotic consensus framework that performs the primary and secondary frequency control. The convergence time t_c of asymptotic consensus algorithms can vary depending on a range of system parameters and does not guarantee finite-time stability. This has been improved by [94], where the authors present a leader-follower or aggregator approach that guarantees finite-time frequency support and state-of-charge (SOC) balancing. However, the t_c of a finite-time consensus is also sensitive to the agent dynamics and

the initial states [94, 95]. Game theoretic approaches on the other hand can be designed as cooperative frameworks that enforce coalition [12, 92] or non-cooperative games that model the competitive nature of the co-existing beneficiaries [96, 97]. Reference [97] models the multi-microgrid energy management system as a non-cooperative differential game where both the global objective and the benefits of the individual agents are formulated. However, the non-cooperative game model is based on the assumption that no agent has market power and it can be challenging to guarantee a nash equilibrium [98]. A comparative study presented in [92] confirms that in scenarios where the global benefits are shared by the individual beneficiaries, it is likely that coalition outperforms a competitive framework in terms of overall resource utilization and individual benefits.

The possibilities of the cooperative control techniques can be enhanced with predictive adaptability by designing a distributed MPC (DMPC). DMPC has been employed successfully for secondary frequency restoration [99, 100] and microgrid energy management problems [101]. The results of [101] show the obvious superiority of the DMPC technique over the consensus and game theoretic frameworks due to the predictive control. To the best of our knowledge FFR and VI control problems have not been addressed using a coordinated MPC framework. The challenge in this implementation is the required speed of control, whilst addressing the individual IBR constraints.

2.3 Modelling and Sizing Flexible Resources

Considering VIE and FFR in DERS, [102] has defined an effective inertia term that is representative of the equivalent aggregate value of inertia of synchronous generators and the distributed energy storage reserves. From a planning perspective, [103] has formulated a reserve placement problem addressed for larger power systems by modelling dedicated converter-based frequency reserves. From power systems operations perspective, [104] has designed synthetic inertia and damping using the system model and then disaggregated them using economic dispatch. However, considering that inertia uses fast-responding reserves, while droop and damping require slower responding reserves, the inertia and damping requirement cannot be disaggregated proportionally based on

the steady-state economic dispatch. The distinction that frequency response reserves utilize bi-directional flexible reserves, whereas the proportional method is based on the sustained injected power capacity is lacking in the former works. We consider resources with time-varying flexibility that is not essentially proportionate to the steady state injected power, for which heterogeneous flexibility models play a crucial role.

With ESS, the flexibility limits are obvious, however with curtailable and shiftable loads, electric vehicles and aggregation of different types of flexibility reserves, the flexibility limits and the corresponding parametric constraints when implementing frequency controls are not very apparent. For this application, virtual battery models (VBM) maybe applied to model the demand flexibility available in the microgrid. Virtual battery parameters may be computed for electric vehicles (EV) [105], thermostatically controlled loads (TLC) [106, 12], heating ventilation and air conditioning (HVAC) loads [107]. Uncertainties in flexible load models are considered in the VBM in [108]. VBM parameters for a combination of heterogeneous flexibilities can be obtained using the method in [109, 30]. Once the available flexibility in the available loads is assessed, ESSs have to sized for the additional flexibility for the desired frequency response characteristics.

2.3.1 Hybrid Energy Storage Systems

Supercapacitor banks (SCESS) [110, 18] and flywheel energy storage systems (FESS) [111, 112] have a faster response and high power capacity which are crucial for FFR and inertia response. Battery energy storage systems (BESS) on the other hand has a relatively lower power capacity and a slower response but a large energy capacity. Thus an intelligent energy mix specific to the application gives an edge on managing the FFR requirements as well as to provide steady-state response. Therefore, in this work hybrid energy storage systems (HESS) are optimally sized for the computed FFR and VIE parameters. The most HESS combination are the BESS-SCESS and BESS-FESS systems for frequency response services [113, 114] or managing renewable intermittency [115, 116].

2.3.2 ESS Sizing Methodologies

The ESS requirement for utility scale systems with high renewable penetration to operate at a desired frequency response has been computed in [57, 117], while the computation is optimized for a set of scenarios in different time zones in [118]. With regard to micro-grids, fourier transform has been applied to size storage systems for the different levels of balancing control [119, 120]. Reference [17] discusses the adequacy evaluation of a PV-based islanded microgrid in a minute-scale in terms of reliability indices. Other algorithms for islanded microgrids have been presented for sizing and placement of ESS from the perspective of energy management [121, 122]. The ESS placement problem is significant in cases where some area of the power system is supported by synchronous generators [103], while the rest of the system is a low-inertia system. However, in the case of 100% converter connected system with fewer units, the microgrid stiffness is uniformly low and the placement of ESS does not affect the performance significantly.

Discrete fourier transform method has been widely used for sizing storage for renewable intermittency management [115, 116]. In [114], a cost-benefit optimization problem is formulated to solve for the sizing of HESS, while a linear programming approach has been formulated in [113]. However, with regard to storage sizing exclusively for FFR and VIE, very few works such as [57] present the computation methodology, however it has been applied for sizing utility-scale ESS. Hence, there is a need for storage sizing methods specifically for FFR and inertia services.

2.4 Small Signal Stability Analysis

Although there is a plethora of work on the VIE control strategies, small signal stability analysis of low inertia systems with IBR inertia emulation is relatively less. Inertia emulation is primarily associated with the enhancement of frequency stability. From the system perspective of installing VIE devices, the number of research works carried out is relatively less. It has been shown that the interaction of inertia controllers may enhance

the frequency stability but deteriorate the small signal stability (SSS) of the system causing power oscillations [33, 34]. Hence, inertia and damping parameters of the controller have to be designed whilst ensuring the SSS of the system. The steady-state operating points of the system have to be known for small signal stability analysis. As we study the impact of FFR on the system, the power flow analysis (PFA) has to be formulated taking into account of frequency as a state variable.

2.4.1 Power Flow Analysis of IMG

2.4.1.1 Deterministic PFA with Droop Formulation

Various established techniques such as Gauss-Seidel, Newton-Raphson, and fast-decoupled methods may be employed to solve the power flow problem in well-meshed transmission power systems. The Jacobian matrix may be ill-conditioned or singular for radial and weakly-meshed power systems. Hence, derivative-based techniques may not serve as reliable power flow analysis tools for microgrids. In [123], the authors have developed a power flow analysis tool based on the Newton trust region method for islanded microgrids (IMGs). The droop equations of the microgrid have been incorporated into the power flow equations and solved using the Newton-Raphson power flow in [124]. However, this method is only suited for a well-meshed microgrid and may result in singular Jacobian matrices when applied to radial and weakly-meshed microgrids [125].

In this paper, we apply a backward/forward sweep (BFS) algorithm based on the direct approach described in [126]. The method involves the formation of two simple matrices based on the system topology: the nodal injection-nodal current matrix (*BIBC*) and the nodal current-nodal voltage matrix (*BCBV*), that eliminate the time-consuming decomposition and the backward/forward substitution of the *Y* matrix in the power flow algorithm. This step greatly simplifies the computation steps in the algorithm and enhances its time efficiency [126]. The inverter control is modelled by the droop equations [47] and these equations are incorporated in the BFS algorithm in this work. Since the BFS algorithm is only suited for radial distribution systems, it has to be modified for its

applicability to weakly-meshed microgrids. To facilitate this, we modify the *BIBC* and *BCBV* matrices of the BFS algorithm.

2.4.1.2 Stochastic PFA

Stochastic factors such as the load and renewable generation uncertainties may not be ignored as they become significant in smaller power systems like the microgrids. Moreover, as the microgrid operation is mainly dependent on DGs in IMGs, their uncertainties will have to be taken into account in power systems stability and security studies [127]. In this work, we extended the BFS-based IMG power flow tool to work in the stochastic domain, i.e. by modelling the uncertainties in the system. The stochastic power flow analysis (SPFA) yields each of the state variables and dependent variables of the system as a probability density function (PDF). Probabilistic power flow methods may be mainly classified into Monte Carlo Simulation (MCS) [128], analytical methods such as cumulant method (CM) [129] and approximation methods such as the '2m' and '3m' point estimate methods (PEMS) [130]. MCS requires several thousands of deterministic power flow analysis (DPFA) runs with random samples generated from the probability distributions of the input variables to maintain a high accuracy [128]. The CM uses cumulants of the input variables to compute the cumulants of the state variables.

Series expansions such as the Gram-Charlier and Cornish-Fisher series are used to obtain the PDFs of the state variables in CM and PEM techniques [131]. The main limitation of using the series expansion is that their convergence cannot always be guaranteed [132]. In this work, we utilize a polynomial chaos expansion based on the Hermite polynomials described in [132] to approximate the deterministic BFS by a polynomial stochastic surface. The principle of this method is that the computationally intensive deterministic runs of the power flow analysis may be replaced by a set of polynomial calculations, thus reducing the computational complexity. As the number of stochastic variables in the system increases, the computation time of the MCS also increases exponentially. The computation time requirement for the same accuracy will be far lesser than the MCS due to the polynomial approximation of the stochastic response surface method.

2.4.2 SSS Conditions on Frequency Response Parameters

The small signal model of an islanded microgrid with 100% droop based IBR has been modelled in [48, 28, 27] and analyzed using modal analysis. Small signal stability of microgrids has been studied in the literature to ensure the reliable operation of MGs as they are low-inertia systems [133, 134, 135, 136]. However, all the above SSS analysis has been made on droop controlled microgrids. Recently, the small signal model of DERs with virtual inertia control has been derived in [137, 138].

The objective of the stability analysis in the thesis is however, to derive the stability conditions imposed on the FFR and VIE control parameters. The droop parameter is optimized with stability constraints in [28], however the requirement in this case is the parametric condition as it corresponds to a very fast control loop. Recently, conditions on the droop parameter has been derived for the lossless microgrid assumption using a Port-Hamiltonian representation [139, 140]. Unlike modal analysis, for which the analysis has to be carried out for different steady-state operating conditions, the Lyapunov function method is used to obtain the robust parameter space to ensure stability [141, 142]. In [143], a barrier function approach is taken to provide the safety conditions of the parameters in the microgrid. In this work, a modal analysis approach is first taken to demonstrate the impact of control parameters on the oscillatory stability with the help of bifurcation plots, following which the closed form expressions, which can be used as parametric stability constraints in the higher level problems such as scheduling and reserve allocation, are derived.

Having discussed the state-of-art techniques in the relevant topics and the definitions of terms and concepts used in this thesis, the following chapters discuss the proposed control methods and analysis in the respective chapters. The following chapter presents the flexibility model used in this work and the proposed storage sizing algorithm.

Chapter 3

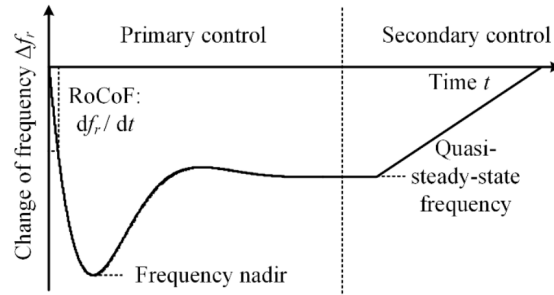
Modeling and Sizing Flexible Resources for Frequency Response

This chapter presents a brief study on the available flexible resources in a power system and a virtual battery model (VBM) to represent aggregated flexibility of different resources. A simple computation method has been presented for sizing hybrid ESSs to provide the additional balancing support to the system for a desired frequency response.

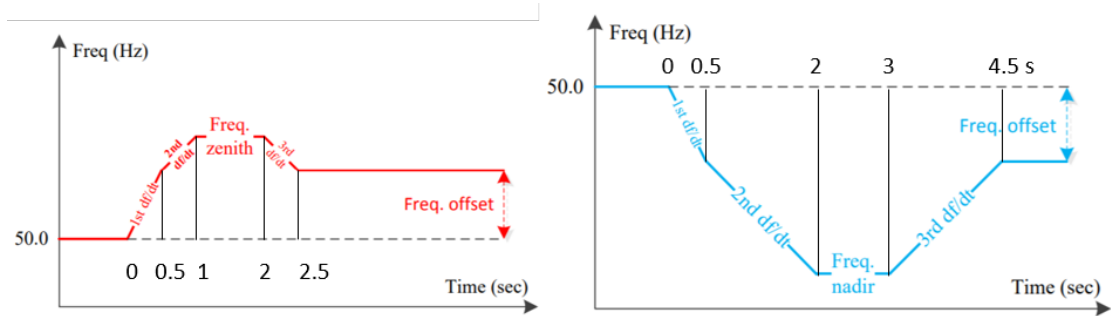
3.1 Desired Frequency Response Characteristics

With the replacement of synchronous machines by IBRs, the frequency response is deteriorated due to the absence of synchronous inertia in the systems. This causes large and sudden frequency deviations on the occurrence of contingencies. Microgrids being small distribution systems primarily fed by DERs with few or no synchronous generators, are low-inertia systems. During the grid-connected operation of the microgrid, the microgrid frequency is controlled by the grid. However, frequency reserves are crucial for a stable autonomous operation of the microgrid. The different stages of frequency control has been described in section 2.2. A typical frequency response characteristic on

the occurrence of a generator contingency is shown in Fig. 3.1a along with the ENTSO-E proposed frequency metric calculation. The frequency metrics of interest from the response are the initial ROCOF (maximum ROCOF occurs on the occurrence of the contingency), f_{nadir} (the extrema of the frequency transient), quasi-steady-state deviation Δf_{ss} (before the SFR is activated), and the nominal steady-state frequency f_0 (once the frequency is restored by the SFR).



(a) Typical Frequency Characteristics with Response Metrics [144].



(b) ENTSO-E Calculation of Metrics.

Fig. 3.1: Frequency Response Metrics.

The recommended approach by ENTSO-E for frequency reserve allocation and assessment is based on the compliance curves shown in Fig. 3.1b. It can be observed that the ROCOF limits depend on the measurement window. Some of the international grid codes of frequency compliance standards are presented below.

3.1.1 International Grid Codes on Frequency Containment

The nominal frequency of a power system is a standardized compromise on the requirements of loads, generators, transformer, and transmission. The electric power systems

Table 3.1: Grid Codes on Frequency Containment.

Region	Instantaneous Δf limits (Hz)	Δf_{ss} limits (Hz)	ROCOF limits (Hz/s)
Europe	49.2-50.8	± 0.2	($\pm 2, 1.5, 1.25$) for (0.5, 1, 2s) window
Australia	49-51	Interconnected - ± 0.15 Islanded - $\pm 0.15, 0.5$	± 1 for 1s window
UK	49-51, 48.8 UFLS	± 0.5 (target: ± 0.05)	± 0.5 for 500 ms window
China	49-51	System ≥ 3 GW: ± 0.2 System < 3 GW: ± 0.5	-
India	49.4 UFLS	± 0.5 (target: ± 0.05)	± 0.2 in stage-1
Singapore	49.7 UFLS	± 0.2	± 1 for 500s window
North America*	59.5, 59.5, 59.3, 58.5 UFLS	$\pm 0.018, 0.0228, 0.03, 0.02$	-

*E- Eastern, W- Western, T-Texas, Q-Quebec Interconnection

around the world are mostly 50-Hz systems, except for the American continents and Japan that employ 60 Hz systems. Meanwhile, traction systems operate at lower nominal frequencies such as 25 or 16.6 Hz due to their historical origin, while weight-sensitive microgrids such as aircraft and marine applications may employ high frequencies such as 400 Hz.

In any of these systems, frequency containment is one of the primary tasks that ensures the generation-load balance of the system, with the continuous instantaneous variation of loads and intermittent generation. The frequency containment grid codes, shown in Table 3.1 [144, 145, 146] help avoid damage of frequency sensitive loads, blackouts in the power system and serve as standards for designing the required containment reserves.

The instantaneous Δf tolerance band gives the allowable f_{nadir} . In most grid codes, the instantaneous limit is specified in terms of the frequency limit on which the under-frequency load shedding (UFLS) is activated. In traditional systems, generator outages and sudden overloads are commonly encountered and therefore the UFLS is popular. However, with the high penetration of intermittent generation, studies of over-frequency

events and the corresponding compliance standards are required. The operating constraints for the quasi-steady state value after the PFR response is given by the Δf_{ss} limits, and the ROCOF limits are defined based on the measurement window in [Table 3.1](#). Very large interconnected systems such as the North American power system does not suffer low-inertia and hence there are no ROCOF restrictions yet. The worst case ROCOF recorded so far is 0.4 Hz/s (Texas interconnection).

The standards and grid codes discussed above target larger power systems. According to the IEEE 2030.7-2017 standard for specification of microgrid control, grid-connected microgrids follow the respective distribution grid standards. For the islanded operation, however, the requirements may be relaxed as they are subjective to the local load requirements and the available resources.

3.2 ESS for Frequency Response

With a growing share of intermittent and non-dispatchable resources in the power system and the lack of synchronous reserves to perform the frequency response services, there is a need for additional controllable resources. Energy storage systems (ESS) offer flexibility by offering a dynamically controllable power response to the system disturbances. Based on the stored energy, ESS technologies can be classified as chemical (fuel cells (FCs)), electrochemical (battery energy storage systems (BESSs) such as Li-ion, Lead acid, NiCd, ZnBr, NaS, Vanadium redox battery (VRB)), kinetic (flywheel ESS (FESS)), potential (pumped hydro storage (PHS)), magnetic (superconducting magnetic energy storage (SMES)), and electrostatic storage (supercapacitor banks (SCESS)).

Storage technologies can be compared in terms of their characteristics such as specific power and energy, which are the power and energy weight density, capacity, and cycle life as shown in [Fig. 3.2a](#). While the BESSs have a high specific energy with low specific power, SCESS, and FESS have low specific energy with high specific power. This implies the high power-low energy rating of SCESS, and FESS and a high energy-low power rating of BESS. Given this difference, supercapacitors and flywheel systems can support

application that require a faster response, while the battery systems can be a better option to support applications that require a sustained response. The chart in Fig. 3.2b depicts the power and discharge time characteristics based on which they are chosen for the specific power system application.

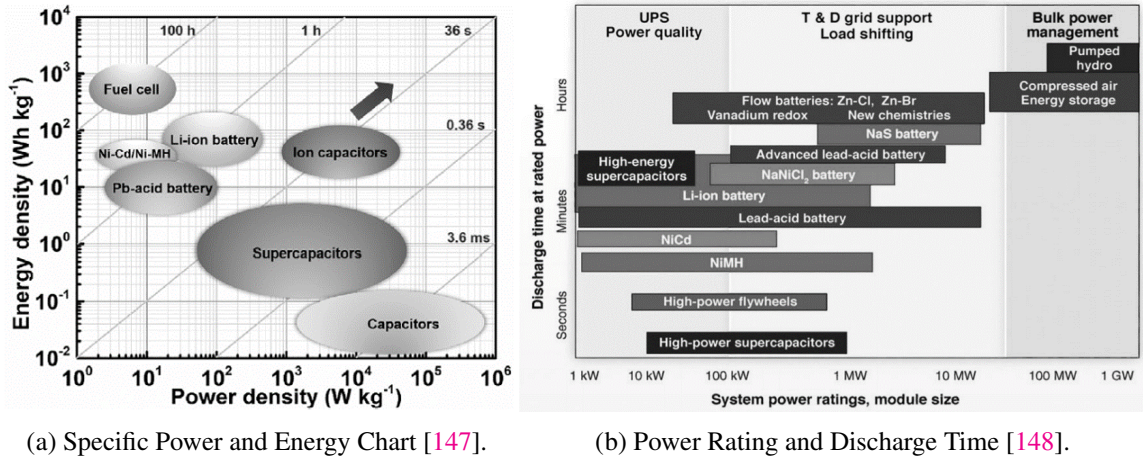


Fig. 3.2: Comparison of Storage Technologies.

3.2.1 Hybrid Energy Storage Systems

For inertia response (IR), there is a need for a very fast-responding ESS with high power capacity for curbing the initial ROCOF on the occurrence of the disturbance. Hence supercapacitors or flywheel systems can be suitable options, among which the SCESS has a high charging/discharging rate, but also a larger self dissipation. However they both have a very low energy capacity. Due to this reason, their response cannot be prolonged over longer periods.

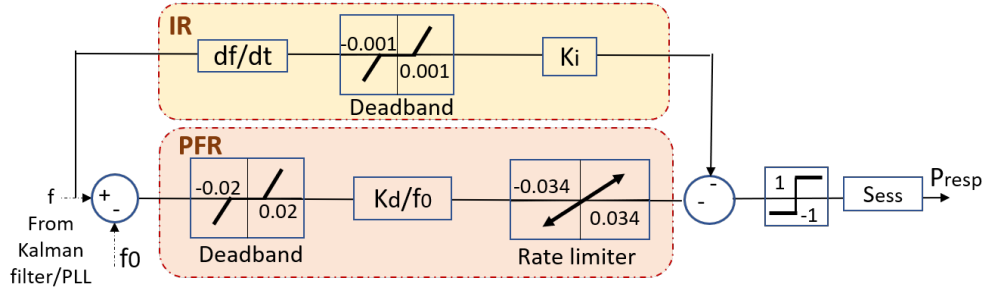
On the other hand, PFR requires a sustained response until the secondary reserves join the controlled response. For participating in the PFR in the ENTSO-E, the reserves must be able to cater to a 15-minutes of sustained response from the start of action. Hence, either of the very fast-responding technologies may not be a good fit for the FFR and PFR requirements. BESS such as Li-ion, can offer a high power capability, whilst having a high energy capacity. Hence, a combination of these storage technologies may be appropriate for inertia emulation and FFR applications.

The choice of storage mix for frequency regulation may also depend on whether the supporting functions are for grid-connected, or off-grid applications. The off-grid regulation services demand a faster charge/discharge rate r , which limits the shelf-life of the storage. SMES-BESS mix may be used for highly demanding off-grid applications, where the long cycle life of SMES addresses the high r . These system requirements are largely dictated by the requirements to actuate the desired control.

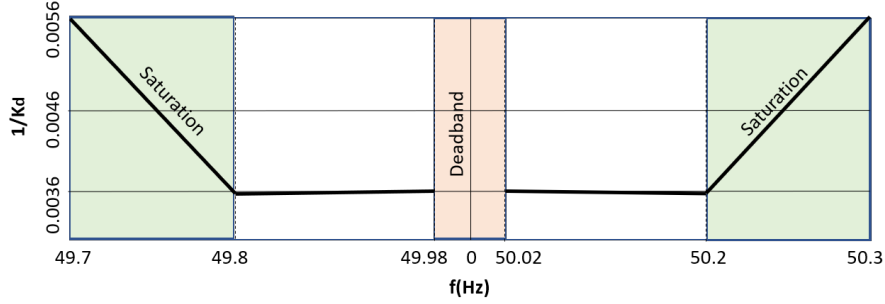
3.2.2 HESS Control

This section describes the inertia emulation and FFR control scheme of HESS shown in Fig. 3.3a, with the effect of the control parameters on the demand from ESS. The control scheme comprises of an inertia response (IR) loop which allows a derivative power response, while the PFR loop allows a proportional response. The control deadbands limit the activation of the control for beyond a frequency deviation and rate limit set based on the grid code. In this control, the ENTSO-E grid code for frequency has been employed to set the deadband limits. The control parameters are K_i and K_d for the IR and PFR respectively. All parameters and variables depicted in Fig. 3.3a are in per unit of the ESS power rating. Therefore the saturation block curbs the control signal to $[-1, 1]$ p.u.

If the PFR is designed for a maximum frequency deviation of $\pm\Delta f_{max}$ and a deadband of $\pm\Delta f_{db}$ at a nominal frequency of f_0 , the corresponding PFR control parameter is given by (3.1). If the ESS is designed to supply its rated power S_{ess} for $\pm\Delta f_{max}$, the power response of the ESS is curtailed to 1 p.u. for disturbances causing deviations beyond the designed value of $\pm\Delta f_{max}$. This implies that the droop parameter starts to decrease beyond $\pm\Delta f_{max}$ and is no more the designed droop K_d . This concept has been depicted in Fig. 3.3b.



(a) Control Scheme.



(b) PFR with Design Constraints.

Fig. 3.3: Frequency Response Control with ESS.

$$K_d = \frac{f_0}{\Delta f_{max} - \Delta f_{db}} \quad (3.1)$$

$$H_{ess} = P_{ir} \frac{f_0}{2} \left(\frac{df}{dt} \right)_{max}^{-1}; \quad P_{ir} = K_i \left(\frac{df}{dt} \right)_{max} \quad (3.2)$$

$$K_i = 2H_{ess}/f_0 \quad (3.3)$$

$$H_{max} = \frac{f_0}{2} \left(\frac{df}{dt} \right)^{-1}, \quad \text{if } |P_{ir}| > 1 \quad (3.4)$$

The IR control is proportional to the derivative where the deadband prevents the control action for small frequency deviations. The inertia contribution of IR control is given by (3.3). Similar to the PFR, the IR control can be designed for a given inertia H_{ess} for a maximum ROCOF $(df/dt)_{max}$ controlled by the gain K_i as shown in (3.2). When the power response P_{ir} exceeds 1 p.u, the response is restricted to the maximum power of the system with H_{max} given by (3.4).

3.3 DER and Load Flexibility for Frequency Response

Apart from dedicated ESS, the flexibility in loads and DERs may be utilized for frequency support in order to minimize the investment on new storage systems. Available flexible resources in IBR power systems among the DERs and loads including: PV, wind curtailment, electric vehicles (EVs), curtailable or shiftable demand such as LED smart lighting loads, thermostatically controlled loads (TCLs) in heating/cooling, ventilation, and air-conditioning (HVAC). Curtailable or shiftable demand has to be modelled and assessed as potential balancing reserves.

3.3.1 Frequency Responsive PV Control

PV curtailment can provide flexibility services, however only by operating below the maximum power point (MPP), which is not at its economic optimality. However, a balance between the DERs and demand can highly reduce the investment on ESS, thus reducing the system operations cost. In some networks, the grid code for PV interconnection force the PV to reduce their output beyond a threshold over-frequency limit f_{ih+} such as reduction by 40% per Hz deviation starting from 50.2 Hz in the German grid code [149]. A frequency-response power control of a PV-IBR without ESS is presented below.

The PV module is connected to the microgrid through a DC-DC boost converter and an inverter as shown in Fig. 3.4. The inverter is current controlled to maintain unity power factor (UPF) with the grid AC voltage as the reference. The power output of the module is adjusted by controlling the output voltage of the DC-DC converter. Ideally, an MPP tracking control is implemented to match the output impedance characteristics with the load impedance characteristics for a maximum power transfer. In this work, the MPPT control is implemented by a simple perturb and observe algorithm [150], where the operating point oscillates around the MPPT. For opposite polarities of ΔP_{pv} and ΔV_{pv} , the voltage reference is reduced and a PI controller is used to track the reference by adjusting the duty cycle of the converter.

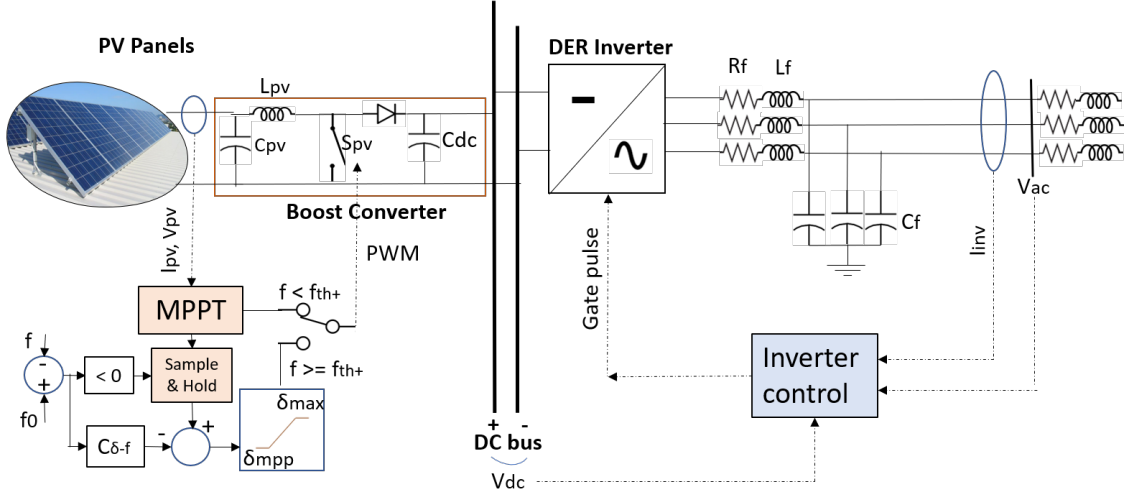


Fig. 3.4: Frequency Responsive PV Control.

In order to account for the frequency-based curtailment control, the voltage reference is calculated for a given PV output power reference P_{ref} based on the frequency droop. However, for frequency responsive control, where P_{ref} varies with the system frequency, it is important to determine the zero power point (ZPP) similar to the MPP. The ZPP occurs at duty cycle $\delta = 1$, while δ_{mpp} for the MPP is determined by the MPPT algorithm. To ensure the output voltage of the PV array is well beyond its open-circuit voltage V_{oc} to avoid injecting power to the panel and damaging it [149], the maximum duty cycle is set as 0.95, with a safety margin below the ZPP. By implementing the required power-frequency droop C_{P-f} for PFR, the frequency-dependent δ of the boost converter can be obtained by (3.5), where $C_{\delta-V}$ and C_{V-P} may be obtained by the PV characteristics based on the irradiance levels.

$$\begin{cases} C_{P-f} = \frac{P_{mpp} - P_{min}}{f_0 - f_{max}} \\ \delta_{pv} = \delta_{mpp} - C_{\delta-f}(f_0 - f) \\ \text{With } C_{\delta-f} = C_{P-f} * C_{\delta-V} * C_{V-P}; C_{\delta-V} = \frac{\delta_{mpp} - \delta_{max}}{V_{mpp} - V_{min}}; C_{V-P} = \frac{V_{mpp} - V_{min}}{P_{mpp} - P_{min}} \end{cases} \quad (3.5)$$

3.3.2 Frequency Response with Controllable Demand

Similarly, a frequency responsive load control can be implemented taking into account the thermostatically-controlled loads and dimmable LED loads. The TCLs have to retain

a certain comfort temperature range which requires the room heating dissipation model-based calculation in the control [151], while the LEDs have to retain certain comfort illumination ranges [152], which gives the corresponding reference power P_{ref} without the frequency response. The power drawn by the controllable loads based on the frequency droop K_{load} is given by (3.6).

$$\begin{cases} K_{load} = \frac{P_{ref} - P_{min}}{f_0 - f_{min}} \\ P_{load} = P_{ref} - K_{load}(f - f_0) \end{cases} \quad (3.6)$$

3.3.3 Virtual Battery Model of Heterogeneous DERs

The aggregated flexibility of DERs are modelled as a virtual storage/battery model (VBM) in this section. The generalized model of heterogeneous DERs serves as an assessment of the frequency response capability of the available resources in the power system. The first order VBM model is given by (3.7), where $C(t)$ is the time-varying state-of-charge (SOC) in % with initial value C_0 and limits $(C_{min}; C_{max})$; $P(t)$ is the power control signal within the limits (P^-, P^+) ; and d_s is the self-dissipation rate of the battery. Therefore the VBM parameter set includes $\phi_{der} = [C_0, C_{min}, C_{max}, P^-, P^+, d_s]$. The parameters are determined by model approximation techniques.

$$\begin{cases} \dot{C}(t) = -d_s C(t) - P(t) \\ C_{min} \leq C(t) \leq C_{max} \\ P^- \leq P(t) \leq P^+ \end{cases} \quad (3.7)$$

Let the minimum time at which either the power or capacity constraints is violated with a control signal $P(t)$ from the initialization is τ_{min} . Then, the quality of the model fit is inversely proportional to the difference in the violation times given by the non-linear model of the load or heterogeneous DERs and that of the corresponding VBM. Thus, the model fit optimization problem can be formulated as shown in (3.8), where B_{der} is the violation time function of the VBM in (3.9), and fn is the violation time function of the non-linear load/DER model to be approximated shown in (3.10).

$$\text{Min } \max_{P(t)} |B_{der}(P(t), \phi_{der}, \tau) - fn(P(t), \tau)| \quad (3.8)$$

$$\text{s.t. } B_{der}(P(t), \phi_{der}, \tau) \leq fn(P(t), \tau)$$

$$B_{der} = \begin{cases} \tau_{min} & \text{if violated} \\ \infty & \text{if } \exists \text{ solution to VBM } \forall t \leq \tau \end{cases} \quad (3.9)$$

$$fn = \begin{cases} \tau_{min} & \text{if violated} \\ \infty & \text{if } \exists \text{ solution to model } \forall t \leq \tau \end{cases} \quad (3.10)$$

It is to be noted that in modelling PV inverter flexibility, there is no capacity limit in the VBM as it is technically an unlimited energy, however the PV model specifications yield the power limits and the self-dissipation. The flexible load models for the heating/cooling and lighting loads, on the other hand, have both the capacity and rate constraints of the control signal given by the temperature and illumination requirements. Estimation of the VBM parameters may be obtained mathematically by formulating an optimization problem [106, 109] or using neural network approximation methods [12].

3.4 ESS Sizing for Frequency Response

The overall methodology for ESS sizing in this work has been described in the algorithm given below. The methodology and the computed parameters are described in the subsections that follow.

1. Identify the expected grid code requirements of frequency response including Δf_{max} and $(df/dt)_{max}$.
2. Analyze the available flexibility using DERS and loads in the system and their plausible contribution to the frequency response requirements of the system. One such methods could be to evaluate them using their corresponding VBM models described in Section 3.3.3.

3. Estimate the existing power-frequency characteristics λ and inertia characteristics H_s of the system.
4. Compute the target power-frequency characteristics λ^* and inertia characteristics H_s^* of the system.
5. List the set of worst case contingencies ΔP_{d-max} for ESS design.
6. Compute the PFR and IR control parameters (K_d^*, K_i^*) based on the data from the previous steps.
7. Estimate the ESS power rating S_{pfr} and S_{ir} for PFR and IR respectively.
8. Estimate the ESS corresponding energy ratings E_{pfr} and E_{ir} based on the required response times.

3.4.1 PFR with ESSs

In this work, the ESS is sized for a maximum allowable quasi steady state frequency deviation of ± 0.2 Hz. Based on the ENTSO-E grid code, the PFR reserve has to act within 30 s when the frequency deviation crosses the ± 0.02 Hz deadband and should be capable of providing a sustained response for at least 15 minutes as described in Section 3.2.2. For a frequency deviation range of ± 0.02 Hz to ± 0.2 Hz, the ESS droop parameter is designed to follow the designed PFR in (3.11).

$$K_d^* = \frac{1}{m_{ess}} = \frac{f_0}{\Delta f_{max} - \Delta f_{db}} ; m_{ess} = (0.2 - 0.02)/50 = 0.0036 \quad (3.11)$$

The power-frequency characteristic of the system λ determines the steady-state frequency error Δf_{ss} for a given disturbance ΔP_d . λ is determined, as shown in (3.12), by the available PFR reserve capacity in the system, such as synchronous machine droop characteristic R_i or the droop response P_i that can be provided by the available flexibility of the i^{th} DER at a rated power of S_i as discussed in Section 3.3. The desired power-frequency characteristic λ^* is calculated in (3.13) for a given worst case contingency.

$$\lambda = -\frac{\Delta P_d}{\Delta f_{ss}} = \sum_{i=1}^n \frac{1}{R_i} \frac{S_i}{f_0}; R_i = -\frac{\Delta f/f_0}{\Delta P_i/S_i} \quad (3.12)$$

$$\lambda^* = -\Delta P_d/\Delta f_{max} \quad (3.13)$$

From the required λ^* and the available λ of the power system, the power and energy rating of the ESS can be computed from (3.14) and (3.15) [57] respectively, where the ESS charging and discharging efficiency are η_c and η_d respectively and the target time to sustain the response t_{reqd} (15 minutes) for the required PFR control action. This calculation also means that for any frequency deviation larger than ± 0.2 Hz, the balancing power supplied or drawn by the ESS will be limited by its rating and the droop value will vary accordingly.

$$S_{pfr} = m_{ess} f_0 (\lambda^* - \lambda) \quad (3.14)$$

$$E_{pfr} = \frac{t_{reqd} S_{pfr} \sqrt{\eta_c}}{3600} + \frac{t_{reqd} S_{pfr}}{3600 \sqrt{\eta_d}} \quad (3.15)$$

3.4.2 Sizing Flexible Resources for Inertial Response

The frequency dynamics of the system is described by the swing equation in (3.16), in which H_s is the existing system inertia. From (3.16), the controlled inertia response of ESS may be computed as shown in (3.17) which has been described in Section 3.2.2. The desired system inertia H_s^* is determined by the constraints on the initial ROCOF estimate $(df/dt)_{max}$ given by the grid code for the worst case contingency in (3.18).

$$\frac{2H_s}{f_0} \frac{df}{dt} = \frac{\Delta P_d}{S_s}; H_s = \frac{\sum_{i=1}^n H_i S_i}{S_s} \quad (3.16)$$

$$H_{ess} = P_{ir} \frac{f_0}{2} \left(\frac{df}{dt} \right)^{-1}; P_{ir} = K_i \left(\frac{df}{dt} \right) \quad (3.17)$$

$$H_s^* = \frac{\Delta P_{d-max} f_0}{S_s} \frac{f_0}{2} (df/dt)_{max} \quad (3.18)$$

For the ESS to deliver the rated power for a frequency derivative of $(df/dt)_{max}$ for a worst case contingency of ΔP_{d-max} , the inertia control coefficient can be designed as

shown in (3.19). Until the allowable ROCOF limit, the ESS is designed to supply the rated power. When the ROCOF value exceeds $(df/dt)_{max}$, the power output of the ESS is curtailed to its rated value, in which case the inertia contribution H_{ess} is given by (3.20). On the other hand, if the control coefficient K_i is varied beyond the designed value, the inertia contribution of the ESS is higher than the corresponding contribution of K_i^* , however the power output of the ESS is curtailed to the rated power well below $(df/dt)_{max}$. If the frequency derivative measurement filter is accounted for, then the actual power required by the control for the inertia response P'_{ir} is given by (3.21), which therefore causes the actual inertia contribution H'_{ess} to be higher than the computed value in (3.20).

$$K_i^* = \left(\frac{df}{dt} \right)^{-1} \quad (3.19)$$

$$H_{ess} = \begin{cases} \frac{f_0}{2} K_i & \text{for } P_{ir} \leq 1 \\ \frac{f_0}{2} \left(\frac{df}{dt} \right)^{-1} & \text{for } P_{ir} > 1 \end{cases} \quad (3.20)$$

$$P'_{ir} = \frac{K_i}{1 + sT} \left(\frac{df}{dt} \right) \quad (3.21)$$

$$H'_{ess} = P'_{ir} \frac{f_0}{2} \left(\frac{df}{dt} \right)^{-1} \quad (3.22)$$

Based on the above computations, the desirable ESS power and energy rating for inertia response can be estimated by (3.23) and (3.24) respectively, where S_s is the system power rating and t_{ir} is the maximum time period during which the IR control action would extend until the PFR control takes over. The energy rating in (3.24) has been computed with a tolerance margin of 10% for a safe design.

$$S_{ir} = S_s \frac{H_s^* - H_s}{H_{ess} - H_s^*} \quad (3.23)$$

$$E_{ir} = 1.1 S_{ir} \left(\int_0^{t_{ir}} \eta_c P_{ir} dt + \int_0^{t_{ir}} \frac{P_{ir}}{\eta_d} dt \right) \quad (3.24)$$

3.4.3 Illustration

As an illustration, the 100% IBR microgrid in Fig. 3.5 is considered to size the ESS for PFR and IR control using droop and virtual inertia control respectively. The system data for the AC side of the microgrid may be obtained from [27]. The autonomous microgrid consists of 3 inverters fed from a DC bus by the combination of a DG source and loads 1,2, and 3 of RL, RC and RL types respectively [48]. In order to size the ESS for PFR, the knowledge of the worst system disturbance P_{dist} is vital. In this case, we consider a 27 kW step load change as the worst disturbance [27]. For this disturbance, to maintain the frequency deviation within allowable levels, the required frequency/power characteristic λ^* of the system is given by (3.13).

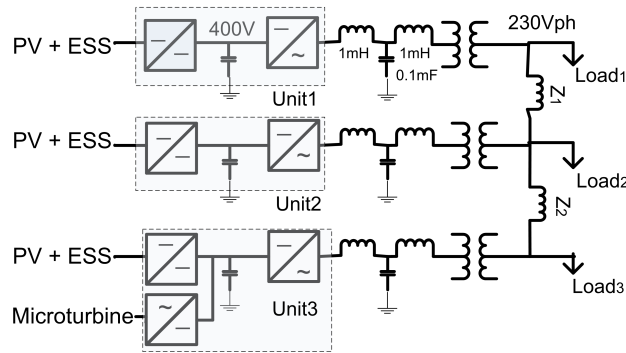


Fig. 3.5: 3-node 100% IBR Microgrid.

Table 3.2 presents the design of ESS computed according to the described sizing procedure in the previous sections. It can be inferred from the table that the PFR directly impacts the frequency deviation and the ESS size for PFR has a low power and high energy rating compared to that of IR. IR control impacts the ROCOF and the f_{min} or f_{nadir} . The power rating required for IR is extremely high and hence comes the need for super capacitors with extremely high power ratings for transient response and BESS to support the sustained PFR response that requires high energy capacity. Once the control is simulated, discrete fourier transform (DFT) can be applied to separate the high and low frequency components to design the HESS optimally [120].

Table 3.2: ESS Sizing for PFR and IR.

PFR Design		IR Design	
m_{ess}	0.0036	K_i	2
Δf_{max}	± 0.2 Hz	$(df/dt)_{max}$	± 0.5 Hz/s
S_{pfr}	24.3 kW	S_{ir}	270 kW
E_{pfr}	12.22 kWh	E_{ir}	2.43 kWh
η_c, η_d	0.9	η_c, η_d	0.9
Simulation with PFR Control		Simulation with IR Control	
Δf_{ss}	0.204 Hz	Δf_{ss}	0.32 Hz
ROCOF	0.55 Hz/s	ROCOF	0.3 Hz/s
f_{nadir}	49.52 Hz	f_{nadir}	49.36 Hz

3.5 Chapter Summary

Utilization of renewable curtailment and load flexibilities for frequency response has been discussed in this chapter. Additional storage reserves have been designed to meet the desired frequency response characteristics of the power system. Control strategies to utilize the designed flexibility of IBRS for IR and FFR in self-consuming energy communities will be explored in the following chapter.

Chapter 4

Coordinated MPC Framework for Grid-following DERs

In this Chapter, a typical PI-based grid-following control for FFR and VIE is presented. The grid-following control has been improved using a coordinated predictive control for application in self-consuming energy communities.

4.1 Grid-following Control

Grid-following IBRs are essentially current-controlled distributed resources that rely on other sources or the grid to serve as the reference voltage source. The small-scale prosumer units in a microgrid may not be capable of performing regulation and stability functions. Grid-following PV inverters with power set point control are referred to as grid-feeding DERs. The grid-feeding units that inject a locally-set power to the grid based on their available resource and feed-in tariff. The grid-forming units act as reference voltage sources for these units. The power references $\{P_{ref}, Q_{ref}\}$ are used to compute the $d - q$ current references in (4.1). The computed reference currents are fed to the current control block shown in Fig. 4.1.

$$\begin{cases} i_{ld}^* = \frac{2}{3} \left(\frac{P_{ref}v_d - Q_{ref}v_q}{v_d^2 + v_q^2} \right) \\ i_{lq}^* = \frac{2}{3} \left(\frac{Q_{ref}v_d - P_{ref}v_q}{v_d^2 + v_q^2} \right) \end{cases} \quad (4.1)$$

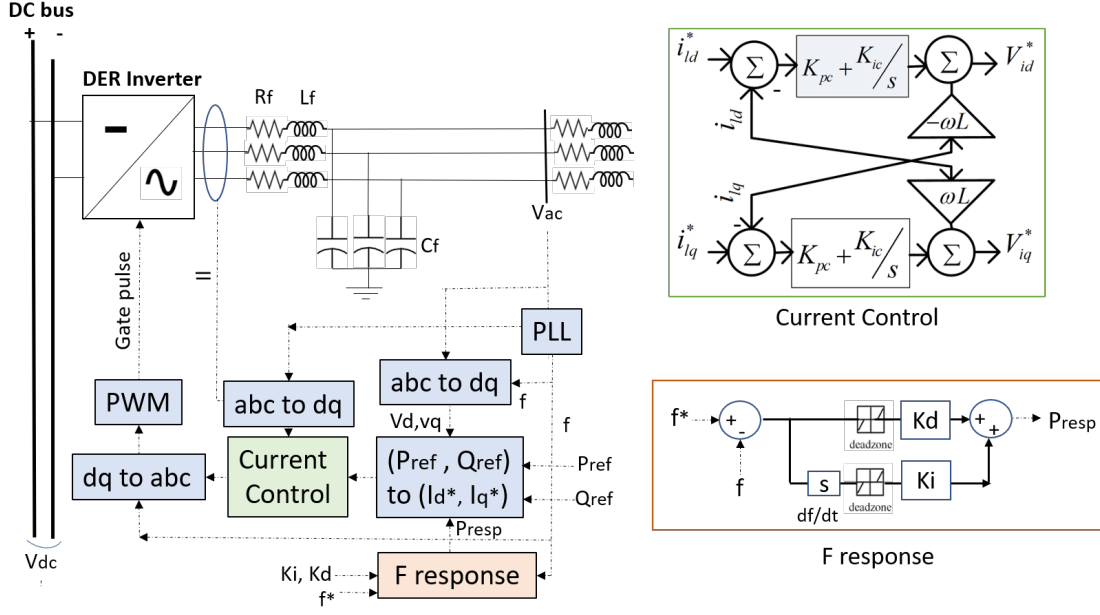


Fig. 4.1: Grid-following Control.

However, some IBRS may be coupled with one or more of the flexibility reserves as described in the previous chapter, and may be capable of participating in the frequency response control. Those that are equipped with certain flexibility to participate in the balancing control are referred to as grid-friendly or grid-supporting DERS (GS-DER) in this work.

4.1.1 Grid-supporting Control

In GS-DERS, the power references of the control are varied as a response to the system frequency. The frequency response block in Fig. 4.1, where the additional power injected for frequency response P_{resp} is computed based on the frequency measurement from the PLL as in (4.2), where K_i and K_d are the inertia and damping control gains whose values are set by (4.3).

$$P_{resp} = P_{damp} + P_{vi} = K_d (\Delta f) + K_i \frac{d\Delta f}{dt} \quad (4.2)$$

$$K_d = \frac{P_{resp_{nom}}}{(\Delta f)_{max}}; K_i = \frac{P_{resp_{nom}}}{\left(\frac{d\Delta f}{dt}\right)_{max}} \quad (4.3)$$

The inertia and damping parameters however, will have to be set carefully to trade off the initial frequency deviation after the contingency and the settling time [63, 67]. In adverse cases, if the control parameters are not tuned properly may result in power oscillations leading to oscillatory instability [26]. In this thesis, a model predictive approach has been proposed for grid-supporting control to vary the inertia and damping levels based on the local flexibility constraints.

4.2 Local MPC Control

In this section, the control strategy in the physical control layer of each grid-friendly DER is described. A model predictive strategy has been employed to replace the conventional PI controllers in the DER, as shown in Fig. 4.2. The predictive control gives access to the trajectory information, which allows the MPC to conduct an optimization over the prediction horizon, avoiding pre-determined constraints based on safety-margins. MPC is a receding horizon control that relies on the plant model for the prediction and has proven its superior performance over a PI control in several applications, including microgrids control [88].

The control comprises the MPC virtual inertia controller (VIC), MPC inverter current controller, and DC-DC controller. The local controllers are coordinated by their speed, such that the inner control loops are sufficiently faster than the outer loop to simplify the control model by overlooking their dynamics.

- The local MPC VIC/frequency control block responds to the measured grid-side frequency by manipulating the reference power P_{vic} . It works at a sampling time of 200 ms and is based on the system model and the locally measured flexibility

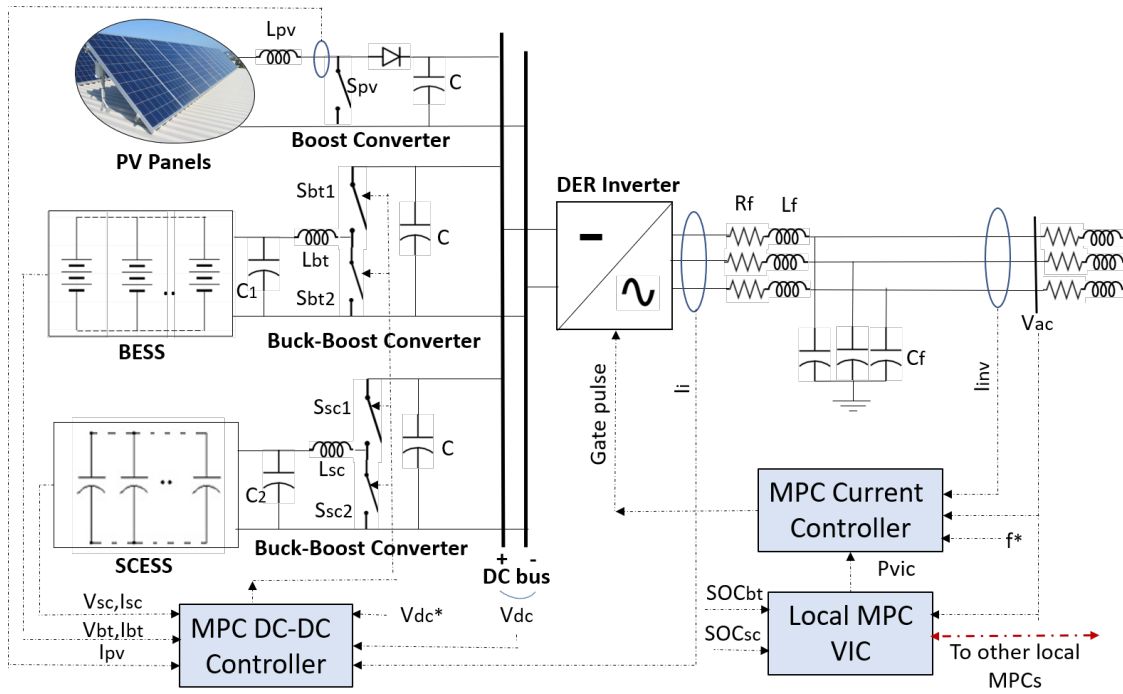


Fig. 4.2: Proposed Control Scheme of a Grid-friendly DER.

constraints of the DER. It manipulates the inertia and damping provided by the DER to the system.

- The MPC current controller controls the DC-AC inverter which operates with a switching frequency of 10 kHz. The switching frequency has to be high enough to maintain a smooth output waveform, however limited by the computation power of the microcontroller. The current control calculates the reference AC current I_{ac}^* based on the P_{vic} of the MPC VIC, and P_{ref} , if any. This MPC tracks the I_{ac}^* and is a faster control loop than the VIC.
- The MPC DC-DC controller controls the buck-boost DC-DC converter which operates with a switching frequency of 200 kHz. It is the innermost and fastest control loop which maintains the DC link voltage constant and in turn maintains the power balance between the DC-side resources and the inverter. The power balance in the DC-link is disturbed by any change in I_{ac} drawn by the inverter and the PV or other renewable intermittency on the DC-side.

Conventional converter controllers equipped with a pulse width modulator (PWM) allow the converter to be modelled in the continuous domain with the help of a modulating signal. However, the MPC converter controls in Sections 4.2.1 and 4.2.2 are direct MPCs that compute the predictive optimization based on all possible switching states of the converter. This method relies on the non-linear discrete model of the converter and filter for state prediction. It is referred to as finite control set (FCS) MPC in Fig. 4.3 and Fig. 4.4.

4.2.1 Model Predictive DC-DC Control

The MPC controller shown in Fig. 4.3 comprises a reference calculator, which determines the updated set-point for the control. The predictor predicts the control objective over the prediction horizon based on the disturbance predictor. The prediction horizon consists of N discrete time intervals throughout this work. The optimizer then determines the control variables for N time intervals and minimize the error between the predicted value and the reference setting over the prediction horizon. However, only a few time steps of control action are performed before the next cycle of prediction, which is termed as the *control horizon*, with N_c discrete time intervals. In this work, we consider the control horizon as one sample time as it gives a satisfactory control performance. The signals in the equations below are shown in Fig. 4.2.

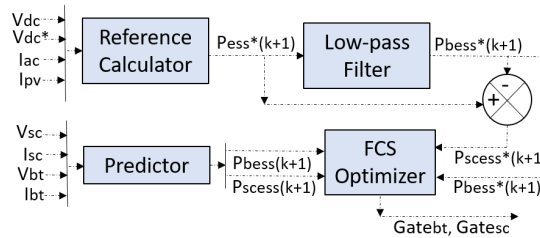


Fig. 4.3: MPC DC-DC Control Schematic.

4.2.1.1 Disturbance Prediction

The varying PV current, I_{pv} , and the AC output current drawn by the inverter, I_{ac} , are the disturbances in the DC-link voltage control problem. Since the DC-DC control loop is

a very fast inner control loop, we consider the prediction for the next time step ($k + 1$) to remain the same as the current measured disturbances, as expressed in (4.4). The disturbance measurements are updated each time-step (k).

$$\begin{cases} I_{pv}(k+1) = I_{pv}(k) \\ I_{ac}(k+1) = I_{ac}(k) \end{cases} \quad (4.4)$$

The DC-link capacitor current is predicted using (4.5) [153], where γ is the coefficient to limit the capacitor current; T_s is the control step time; and V_{dc}^* and $V_{dc}(k)$ are the reference and the measured DC voltages respectively.

$$I_c(k+1) = \frac{C}{\gamma \cdot T_s} (V_{dc}^* - V_{dc}(k)) \quad (4.5)$$

4.2.1.2 Control Reference Calculation

With the predicted DC current, $I_{dc}(k+1) = I_{pv}(k+1) - I_c(k+1) - I_{ac}(k+1)$, the reference power to be injected by the ESS is calculated using (4.6). In this work, we use a hybrid ESS comprising of a battery energy storage system (BESS) and a supercapacitor bank (SCESS) for a combination of high power and high energy capacity. As the SCESS is of higher power capacity, the high frequency component of P_{ess}^* is assigned to the SCESS, while the low frequency component or the slower disturbances are assigned to the BESS, with the use of filters.

$$P_{ess}^*(k+1) = V_{dc}^* I_{dc}(k+1) \text{ With } \begin{cases} P_{bess}^*(k+1) = \left(\frac{\omega_c}{s+\omega_c} \right) P_{ess}^*(k+1) \\ P_{scess}^*(k+1) = \left(\frac{s}{s+\omega_c} \right) P_{ess}^*(k+1) \end{cases} \quad (4.6)$$

4.2.1.3 Model Prediction

Based on the discrete non-linear converter model, the switching states in Table 4.1 are used to predict the battery and supercapacitor currents $I_{bt}(k+1), I_{sc}(k+1)$ based on the respective converter switching states. With 2 buck-boost converters in this scenario,

Table 4.1: Buck-Boost Converter Outputs.

S_1	S_2	Predictor Equation
BOOST MODE		
1	0	$I(k+1) = I(k) + (T_s/L)V(k)$
0	0	$I(k+1) = I(k) + (T_s/L)(V(k) - V_{dc}(k))$
BUCK MODE		
0	0	$I(k+1) = I(k) - (T_s/L)V(k)$
0	1	$I(k+1) = I(k) - (T_s/L)(V(k) - V_{dc}(k))$

there are 4 finite control sets for each of the 2 independent buck-boost converters. The predicted currents are used to determine the battery and supercapacitor output powers given by (4.7).

$$\begin{cases} P_{bess}(k+1) = I_{bt}(k+1) \times V_{bt}(k+1) \\ P_{scess}(k+1) = I_{sc}(k+1) \times V_{sc}(k+1) \end{cases} \quad \text{With} \quad \begin{cases} V_{bt}(k+1) = V_{bt}(k) \\ V_{sc}(k+1) = V_{sc}(k) \end{cases} \quad (4.7)$$

4.2.1.4 Finite Control Set (FCS) Optimization

The DC-DC MPC controls the buck-boost converter operating with a switching frequency of 200 kHz, using the high-speed FCS predictive optimization. The control objective is optimized considering the four possible predicted states of each converter. The decision variables of the optimization are $\{S_{bt-1}, S_{bt-2}, S_{sc-1}, S_{sc-2}\}$. In order to track the reference DC link voltage, the optimal control set may be obtained by minimizing the cost function in (4.8). The constraints in (4.9) show the battery and supercapacitor power and

voltage limits.

$$\min \sum_{k=1}^{N-1} \left[\left(\frac{1}{P_{bess}^*} (P_{bess}^*(k+1) - P_{bess}(k+1)) \right) + \left(\frac{1}{P_{scess}^*} (P_{scess}^*(k+1) - P_{scess}(k+1)) \right) \right] \quad (4.8)$$

$$s.t. \begin{cases} P_{bt}^- < P_{bess}(k+1) < P_{bt}^+ \\ P_{sc}^- < P_{scess}(k+1) < P_{sc}^+ \\ V_{bt}^- < V_{bt}(k+1) < V_{bt}^+ \\ V_{sc}^- < V_{sc}(k+1) < V_{sc}^+ \end{cases} \quad (4.9)$$

4.2.2 Model Predictive Inverter Current Control

The objective of the AC-side inverter current controller is to track the DER power set-point by tracking the equivalent current reference. The illustrated control shown in Fig. 4.4 is a grid-following control, where V_{ac} is obtained from the node of connection. The main grid or the grid-former provides the AC voltage reference in case of grid-connected and islanded modes respectively.

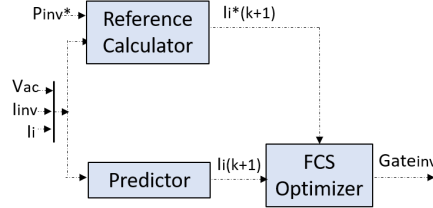


Fig. 4.4: MPC Inverter Control Schematic.

4.2.2.1 Reference Calculation

For synthetic inertia emulation and damping response, the additional injected reference power is obtained from the MPC VIC, while any change steady state power reference may be ΔP_{ref} . From the power reference in (4.10), the current reference can be calculated as given by (4.11).

$$\Delta P_{inv}^*(k+1) = \Delta P_{ref} + \Delta P_{vic} \quad (4.10)$$

$$I_i^*(k+1) = I_i(k) + \Delta P_{inv}^*(k+1)/V_{ac}(k) \quad (4.11)$$

4.2.2.2 Model Prediction

The inverter may be represented by a discrete non-linear model in terms of its switching states (S_a, S_b , and S_c), where a, b , and c represent the IGBT leg of each phase, with 2 states each based on which IGBT is on. The inverter output voltage V_i determined by the switching state vector S is given by (4.12).

$$\begin{cases} S = \frac{2}{3} (S_a + S_b e^{j(2\pi/3)} + S_c e^{j(4\pi/3)}) \\ V_i = V_{dc} S \end{cases} \quad (4.12)$$

The $L_f C_f$ filter dynamics are modelled in (4.13); and I_f and V_c are the filter current and the capacitor voltage respectively.

$$\begin{cases} L_f \frac{dI_i}{dt} = V_i - V_c - I_i R \\ C_f \frac{dV_c}{dt} = I_i - I_{inv} \end{cases} \Rightarrow \dot{\mathbf{x}} = \mathbf{A}\mathbf{x} + \mathbf{B}\mathbf{y}$$

where $\mathbf{x}(k) = \begin{bmatrix} I_i(k) \\ V_c(k) \end{bmatrix}$; $\mathbf{y}(k) = \begin{bmatrix} V_i(k) \\ I_o(k) \end{bmatrix}$; $\mathbf{A} = \begin{bmatrix} -\frac{R_f}{L_f} & -\frac{1}{L_f} \\ \frac{1}{C_f} & 0 \end{bmatrix}$; $\mathbf{B} = \begin{bmatrix} \frac{1}{L_f} & 0 \\ 0 & -\frac{1}{C_f} \end{bmatrix}$ (4.13)

Representing the model (4.13) in the discrete form with sample time t_s and solving the equation, the inverter predictor current equation is then derived as given in (4.14).

$$\mathbf{x}(k+1) = e^{\mathbf{A}t_s} \mathbf{x}(k) + \left[\int_0^{t_s} e^{\mathbf{A}\tau} \mathbf{B} d\tau \right] \mathbf{y}(k)$$

$$I_i(k+1) = e^{\mathbf{A}t_s} \mathbf{x}(k) + \mathbf{A}^{-1} (e^{\mathbf{A}t_s} - I) \mathbf{B} \mathbf{y}(k) \text{ With } e^{\mathbf{A}t_s} = \begin{bmatrix} -e^{-\frac{R_f t_s}{L_f}} & -e^{-\frac{t_s}{L_f}} \\ e^{-\frac{t_s}{C_f}} & 1 \end{bmatrix} \quad (4.14)$$

4.2.2.3 FCS Optimization

The reference tracking is implemented with the MPC controller by optimizing the objective function given in (4.15) subject to the inverter maximum current limit I_{lim} , with 7 distinct control sets based on the possible inverter switching states. The decision variables of the optimization are $\{S_a, S_b, S_c\}$.

$$\begin{cases} \min \sum_{k=1}^{N-1} \frac{1}{T_i^*} (I_i^*(k+1) - I_i(k+1)) \\ \text{s.t. } |I_i(k+1)| \leq I_{lim} \end{cases} \quad (4.15)$$

4.2.3 Model Predictive Inertia Tuning

With the presented controls, it is possible to realize a distributed virtual inertia control (D-VIC) with individual DER controls. In this work, we complement the D-VIC with a simple MPC-tuner, the objective of which is to fast-tune the inertia $H_i \propto K_{vi-i}$ and $D_i = 1/R_i$ offered by the i^{th} DER locally while respecting the upper-bounds (v, ρ) derived from the slower consensus control. Fast tuning essentially means that the power injected by the grid-friendly DER is varied locally in each DER to optimize the frequency response characteristics over the prediction horizon.

Real-time controllability of the inertia reserve is a unique aspect of the synthetic inertia, which is absent in synchronous machines. In a conventional virtual inertia and damping controller, the injected power is given by (4.16). The controllability of the inertia can be exploited to improve the frequency transient metrics. It has been shown by recent research works [70, 59] that a high inertia can improve the initial ROCOF, $\dot{\omega}_{max} = \Delta P_d / (2H_s)$, while fast-acting primary frequency reserves, along with inertia reserves, can improve the frequency nadir, f_{nadir} . Both the inertia and the fast-acting primary frequency reserves inject additional power in response to the disturbance. In this work, we distinguish the fast-acting primary and the inertia reserves based on their control function. The inertia reserves inject an additional power proportionally to the frequency derivative, while the primary reserves inject an additional power proportionally to the frequency deviation. By fast-acting primary reserves, we refer then to the

power injected proportionally to the frequency deviation but with a very short control delay. However high the fast-acting primary reserves is in the system, only the inertia reserves affect the initial ROCOF. Hence, the system inertia is highly significant before the occurrence of the disturbance. The initial value of the individual inertia constant of DERs is henceforth the upper limit of the inertia provided by the DERs through the frequency transient.

$$\left\{ \Delta P_{vic}^* = 2H\dot{\omega} + D\omega \text{ With } \omega = 2\pi(f - f^*) \right. \quad (4.16)$$

If the inertia constant is maintained at its upper limit, through the frequency response, after the primary control reserves came into action, it causes a high peak overshoot. Once the f_{nadir} , expressed as $\Delta\omega_{max}$ in (4.18), is crossed, the need for an inertia response to limit the ROCOF is reduced, while the droop damping constant plays a major role in the settling time of the frequency response [59]. The MPC is enabled only beyond a ROCOF deadband of $\pm 0.01 \text{ Hz/s}$. Once the control is disabled, the parameters are reset to the initial value in case of another disturbance.

4.2.3.1 Frequency Predictor

As per the p.u. AC system frequency response model, expressed in (4.17), the system frequency can be predicted over the prediction horizon of the MPC control N_h , which lasts for a typical frequency transient settling period of 2 s, while the control operates with a time step of 0.2 s. Hence, the prediction is given by the system frequency dynamics as shown below.

$$\Delta\omega(s) = \Delta P_d(s) \left(\sum_{j=1}^{n_d} \frac{1}{R_j(1 + T_j s)} + \sum_{i=1}^{n_h} 2H_i s \right)^{-1}$$

$$\text{With } H_s = \frac{\sum_{i=1}^{n_h} H_i S_i}{\sum_{i=1}^{n_h} S_i}; D_s = \frac{\sum_{j=1}^{n_d} D_j S_j}{\sum_{j=1}^{n_d} S_j}; T_1 = T_2 = \dots = T_j = T, \forall j \in n_d \quad (4.17)$$

The control assumes that every grid-friendly DER is equipped with the same MPC tuning. So, the obtained per unit optimal inertia constant is used to tune H among all controllable

synthetic inertia units, thus enforcing a decentralized control. In case the other DERs are not equipped an MPC H -tuner, the equivalent inertia of the system tuner must be modified with the H parameters of the synchronous generators or other DERs, while only the H_i of the i^{th} DER is tuned.

The transfer function of the system in the standard second order form with a natural frequency ω_n and a damping coefficient ζ is presented in (4.18). The time of the frequency nadir and its expression are computed by setting the frequency derivative to zero.

$$\frac{\Delta\omega(s)}{\Delta P_d(s)} = \frac{1}{2H_s T} \frac{(1+sT)}{(s^2 + 2\zeta\omega_n s + \omega_n^2)}$$

$$\text{With } \omega_n = \frac{D_s}{2H_s T}; \zeta = \frac{2H_s + TD_s}{2\sqrt{2H_s D_s T}}; \omega_d = \omega_n \sqrt{1 - \zeta^2};$$

$$t_{nadir} = \frac{1}{\omega_d} \tan^{-1} \left(\frac{\omega_d}{\zeta\omega_n - T^{-1}} \right); \Delta\omega_{max} = f_{nadir} = \frac{-\Delta P_d}{D_s} \left(1 + \frac{T e^{-\zeta\omega_n t_{nadir}}}{2H_s} \right) \quad (4.18)$$

4.2.3.2 Disturbance Prediction

Disturbance estimation algorithms can be used to predict the disturbance over the prediction horizon, however we are aiming for a fast-frequency control in which case the prediction is a very short-term forecast. Therefore, for a simpler model, we employ the disturbance prediction $P_d(k+1) = P_d(k)$, which is used to predict the frequency using (4.17).

4.2.3.3 Optimization

The MPC tuner controls the frequency response in real time by optimizing the frequency deviation and ROCOF metrics, as expressed in (4.19), where u_i is the control effort in terms of power injected P_{vic} . q_1, q_2 and r are tunable state and the control effort penalties of the control problem. The manipulated variables are inertia coefficient K_{vi-i} and damping coefficient D_i of the i^{th} DER. The control works at a sampling time of 200 ms, where upper-bounds of the control variables v, ρ are computed by the consensus algorithm that is executed in every 15-minutes slot by updating the system parameters and

the DER flexibility constraints.

$$\begin{cases} \min \sum_{k=1}^{N-1} \left(q_1 \Delta \omega_i(k)^2 + q_2 (\dot{\Delta \omega}_i)(k)^2 + r \Delta u_i(k)^2 \right) \\ s.t. \begin{cases} 0 \leq K_{vi-i}(k+1) \leq v \\ 0 \leq D_i(k+1) \leq 1/\rho \end{cases} \end{cases} \quad (4.19)$$

4.3 Coordinating Frequency-Responsive DERs

The interaction of cyber and physical layers of the power system facilitates the usage of remote measurements and control exchanges between DERs participating in the grid-support functions for the system. In this section, we present the proposed distributed average consensus optimization for proportional sharing of inertial response (IR) and primary frequency response (PFR), considering DERs as plug-and-play agents, with identical linear time-invariant (LTI) dynamics, which can be involved in peer-to-peer (p2p) communications. The completely distributed control architecture with p2p communication, shown in Fig. 4.5b, unlike the centralized formulation, does not involve a central controller, show in Fig. 4.5a. We thereby aim to exploit the cyber-physical architecture of the power system to deliver a robust inertia compensation while evading installations of dedicated storage reserves to perform the same task.

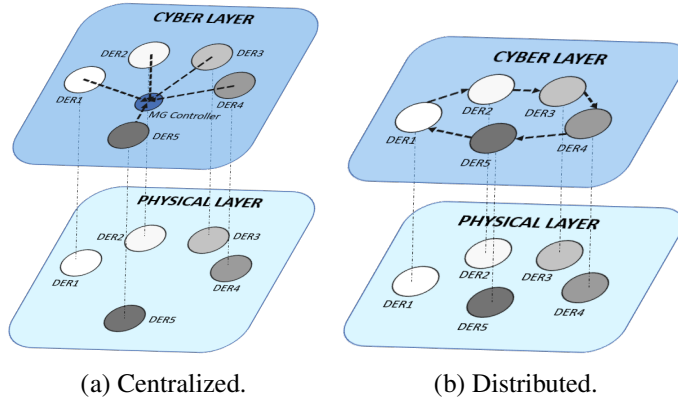


Fig. 4.5: Control Structures for DERs as Multi-Agent Systems.

4.3.1 System Model

The DERs are the agents in the system that can choose to participate in grid-support functions over a scheduled period of time and are thus declared as *grid-friendly* DERs. The frequency dynamics of the microgrid is modelled by the swing equation given in (4.20), where S_i is the rated capacity of i^{th} DER, S_{sys} is the rated system capacity, and ΔP is the generation-load imbalance due to the disturbance in per unit (p.u.). Grid-forming entities in the system such as virtual synchronous generators and physical synchronous generators (if any), contribute to the global system inertia, referred to as H_s . The grid-friendly DERs act as power reserves. The objective of which is to provide the fastest maximum power response in the event of a disturbance, thereby contributing additionally to the IR-PFR capacity of the microgrid. A grid-friendly DER i may be equipped with a combination of very fast responding reserves with a response delay time $T_{r-i} \leq 500 \text{ ms}$ and a power capacity P_{ir} and, a relatively slower reserve capacity P_{pfr} with a higher energy capacity E_{der} . This can be delivered by hybrid storage or flexibility systems that are shown in the later sections. Some grid-friendly DERs may be equipped with only one of these flexibilities, however, the control of PFRs and IRs are coordinated in this work for an optimal performance.

$$\begin{cases} \frac{2H_{sys}}{f_0} \frac{df}{dt} + D_{sys} (\Delta f_{p.u.}) = \Delta P = (P_g - P_l) / S_{sys} \\ \Delta f = (f - f_0) / f_0 \\ H_{sys} = H_s + \sum_{i=1}^{N_{vi}} \frac{H_i S_i}{S_{sys}} \\ D_{sys} = D_s + \sum_{i=1}^{N_{pfr}} \frac{1}{R_i} \frac{S_i}{S_{sys}} \end{cases} \quad (4.20)$$

The IR and PFR contributions by the i^{th} DER are given by H_i in (4.21) and R_i in (4.25) respectively. In this work we consider the possibility that the DER equipped with IR capability may not always have the energy capacity to support PFR and vice versa, where the DER may lack the fast response capability that is sufficient to provide IR. To include this possibility we differentiate DERs into a group of N_{vi} and N_{pfr} each providing virtual inertia and primary frequency response respectively.

Considering the IR of a grid-friendly DER, if the power injected by DER i is given by P_{ir-i} (p.u.) in (4.22), with a time response delay of T_{r-i} and an inertia control gain K_{vi-i} . Considering that the response time for IR is considerably the same across the group of N_{vi} DERs, P_{ir-i} may be approximated as shown in (4.23). However, with the limitation of flexibility reserve, for a ROCOF beyond the designed value in the system, the inertia contribution is limited. It is also possible that for a very high gain, the inertia contribution P_{ir-i} is restricted to 1 p.u. as shown in (4.24). For proportional sharing of IR on the event of a disturbance within the designed ROCOF limits, it is implicit that $K_{vi-1} = K_{vi-2} \dots = v$, where v is the coordinated inertia gain among the participating DERs.

Similarly, the power injected by the i^{th} DER for the PFR is given by (4.25), where (4.26) ensures proportional sharing among participating DERs if ρ is the coordinated primary response coefficient. If the DER is considered to provide bi-directional flexibility for a span of $t_p = 15 \text{ mins}$, the energy throughput of the DER is given by (4.27) in kWh, where η is the round-trip efficiency of the flexible reserve. It is to be noted that uni-directional flexibility may also be modelled likewise with simple alterations.

$$H_i = P_{ir-i} \frac{f_0}{2} \left(\frac{df}{dt} \right)^{-1} \quad (4.21)$$

$$P_{ir-i} = \frac{K_{vi-i}}{1 + sT_{r-i}} \left(\frac{df}{dt} \right) \quad (4.22)$$

$$P_{ir-i} \approx K_{vi-i} \left(\frac{df}{dt} \right) \quad (4.23)$$

$$H_i = \begin{cases} \frac{f_0}{2} K_{vi-i} & P_{ir-i} \leq 1 \\ \frac{f_0}{2} \left(\frac{df}{dt} \right)^{-1} & P_{ir-i} > 1 \end{cases} \quad (4.24)$$

$$R_i = -\Delta f_{ss} / P_{pfr-i} \quad (4.25)$$

$$\frac{S_1}{R_1} = \frac{S_2}{R_2} = \dots = \rho \quad (4.26)$$

$$E_{pfr-i} = \frac{P_{pfr-i} t_p \sqrt{\eta_i}}{3.6e6} \quad (4.27)$$

In this work, we employ a generalized first-order virtual battery model to represent holistically the flexibility constraints of DERs. The first-order virtual battery model (VBM) parameters are the initial state-of-charge (SOC) C_0 , SOC bounds, C_{min} and C_{max} , which

reflect the bi-directional remaining energy capacity limits E_i^-, E_i^+ in kWh, the power limits, P^- and P^+ , and the self-dissipation rate d_s . The effect of d_s in the remaining energy capacity calculation may be neglected for the IR and PFR calculation as we deal with short time slot. The parameters of the DERs are updated in every 15-minute timeslot of coordinating IR and PFR. The parameters of DERs such as electric vehicle parking lots, flexible heating and cooling systems, fast curtailable demand, etc, can be obtained using a performance tracking optimization technique [154] which is out of the scope of this work. The VBM representation of the DER i is given in (4.28), where C_i and P_i are the SOC and the power response of the i^{th} DER in a given time slot respectively.

$$\begin{cases} \dot{C}_i = -d_s C_i - P_i \\ C_{imin} \leq C_i \leq C_{imax} \\ P_i^- \leq P_i \leq P_i^+ \end{cases} \quad (4.28)$$

4.3.2 Consensus-based Coordination

The consensus algorithm allows a set of entities to agree on a quantity of interest by exchanging information via communication. The quantities of interest in this case are the collective decision variable \mathbf{v} and $\boldsymbol{\rho}$ for IR and PFR coordination respectively. The distributed consensus is of special interest when the objective of the optimization problem is a global objective. There may be local constraints and local objectives in the problem. In this case, the objective of the consensus problem is to coordinate DERs for a proportional contribution of inertia and damping, while meeting the individual DER constraints in (3.7), where \mathbf{v} and $\boldsymbol{\rho}$ are the collective decision variables in the consensus problem, represented as \mathbf{Z} .

The communication network used for the distributed optimization of n number of DERs is represented by a connectivity matrix $\boldsymbol{\alpha} = \{n, n\}$ given by (4.29), where n_i denotes the set of nodes connected to i . Based on graph theory [155], the laplacian matrix of the network may be written as $\mathbf{l}(n, n) = \mathbf{d} - \boldsymbol{\alpha}$, where \mathbf{d} is a diagonal matrix, and $d(i, i)$ is the cardinality of n_i . The communication between the connected DERs is considered to

be bi-directional. For the distributed algorithm, it is required that the communication path is fully connected, i.e. there exists a path between every node with every other node in the network. We apply the local adjacency method to compute the weight matrix $w(n, n)$ in (4.30). If Z is the collective decision variable on which the consensus has to be reached, the consensus update equation at the end of iteration m is given by (4.31).

$$\alpha_{ij} = \begin{cases} 1, & i \neq j, j \in n_i \\ 0, & \text{otherwise} \end{cases} \quad (4.29)$$

$$w_{ij} = |l_{ij}| / \sum_{j=1}^n l_{ij} \quad (4.30)$$

$$Z_i(m+1) = \sum_{j=1}^n w_{ij} Z_j(m) \quad (4.31)$$

The coordinated decision variables computed by the i^{th} DER in the consensus algorithm, v_i and ρ_i , are obtained by solving (4.32) and (4.33) respectively, for a pre-computed worst case contingency ΔP_d based on the system loading/renewable penetration scenario. Objective (4.32) minimizes the calculated worst case ROCOF using the system model in (2.9) and (4.21). The optimization includes a penalty cost function for the control effort $F_i(v_i)$. In this work, a linear cost function is used with normalized gain q_1 and normalized violation penalty p_1 .

$$\begin{aligned} \text{Min} \quad & p_1 |df/dt| + q_1 F_i(v_i) \\ \text{s.t.} \quad & P_i^- \leq P_i \leq P_i^+ \end{aligned} \quad (4.32)$$

$$\begin{aligned} \text{Min} \quad & p_2 |\Delta f_{ss}| + q_2 F_i(\rho_i) \\ \text{s.t.} \quad & P_i^- \leq P_i \leq P_i^+ \\ & E_i^- \leq E_i \leq E_i^+ \end{aligned} \quad (4.33)$$

Similarly, the DER collective decision variable for PFR is obtained by optimizing (4.33) which minimizes the steady state frequency deviation error $|\Delta f_{ss}|$ calculated using the system model for the disturbance ΔP_d . The energy capacity required is obtained from (4.27). In systems with very limited reserves compared to the desired worst case disturbance, the optimization problem can be modified with constraint violation penalty. The

expressions for inertia contributed with a power capacity constraint is expressed in (4.24). Once the collective decision variables of individual DERs are obtained, the consensus problem can be solved as shown in (4.31) until convergence is reached. The consensus reached by agents with identical dynamics and a balanced connectivity matrix is the distributed average of the initial local decision variables (v_i, ρ_i) [155]. The consensus variables in turn represent the initial inertia and the post disturbance damping, which are the upper-bound parameter setting to be used in the local MPC controllers.

4.4 Results and Discussion

4.4.1 System Description

We consider the CIGRE benchmark system [156] as it is a radial distribution microgrid with DERs of different capacities and is a representative of self-consuming energy communities towards which this work is targeted. The microgrid comprises six DERs that are classified as shown in Fig. 4.6, based on their functionalities. In the islanded mode, the grid-forming DER 2 acts as the reference voltage source of the microgrid and performs voltage and frequency regulations. Among the other DERs, DER 4 and DER 5 are not equipped with flexible resources. However, they can provide unidirectional flexibility via PV curtailment. It is not desirable to curtail the PV production unless there is an unavoidable case. The other DERs (1, 3 and 6) are equipped with time-varying flexibility with hybrid energy storage systems and PV production.

Table 4.2 presents the virtual battery model parameters of the DER-ESS used in the study. The charging/discharging rate r_{max} gives the ratio of energy to power capacity of the ESS. The round trip efficiency is η and s , the self-discharge rate, is presented per day (p.d.) or per month (p.m.). The used data is a representative of typical commercial ESSs.

We consider that the hybrid ESS (HESS) in DER 1 and DER 3 comprises BESS and fly-wheel ESS (FESS), and BESS and SCESS respectively. HESSs allow highly efficient operation and reduce the cost over the system's lifetime. The BESS in this case only takes

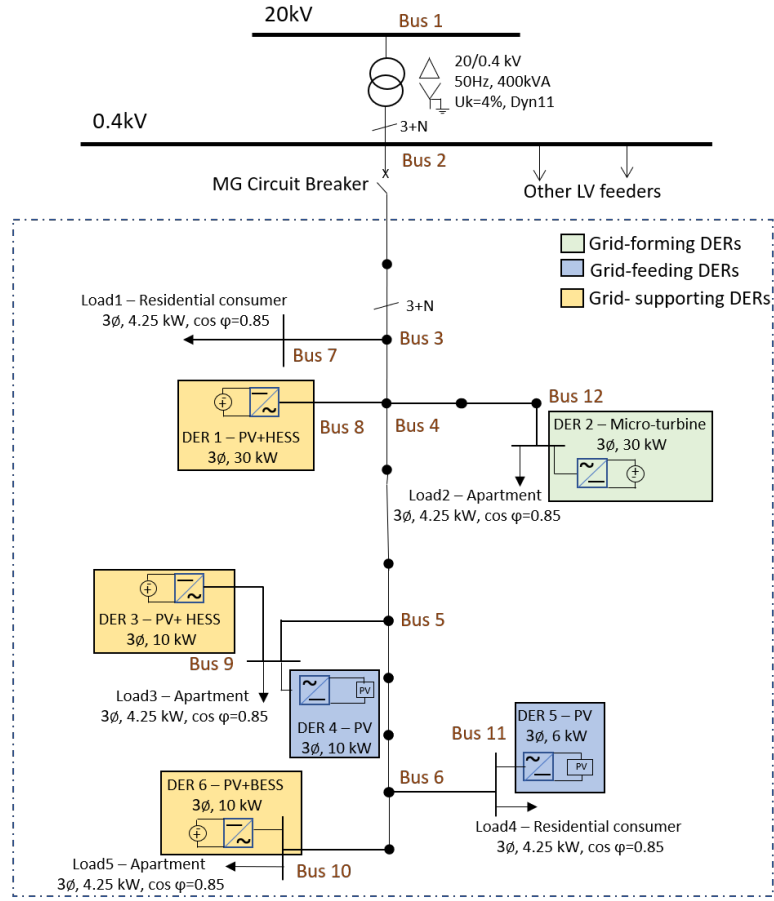


Fig. 4.6: Modified CIGRE Benchmark Microgrid System.

Table 4.2: Virtual Battery Model Parameters.

Parameters	DER-1		DER-3		DER-6
	FESS	BESS	SCES	BESS	BESS
$s, \%$	5 p.d.	5 p.m.	90 p.m.	5 p.m.	5 p.m.
$C_0, \%$	100	50	100	70	80
$C_{min}, \%$	~ 0	20	5	50	20
$C_{max}, \%$	~ 100	80	95	80	80
r_{max}	10 min	3 h	10 s	3 h	3 h
$\eta, \%$	85	70	92	70	70

over when the FESS is at full-speed or stand still, or when the SCES is fully charged or discharged, especially for lasting frequency deviations. It thereby improves the battery lifetime since the fast-acting ESS has a long cycle life and far lesser deterioration compared to BESS. Li-ion BESS is considered in this work. A typical FESS can provide up to 80 % of its rated power capacity after 10–15 years of usage. FESS is of a higher

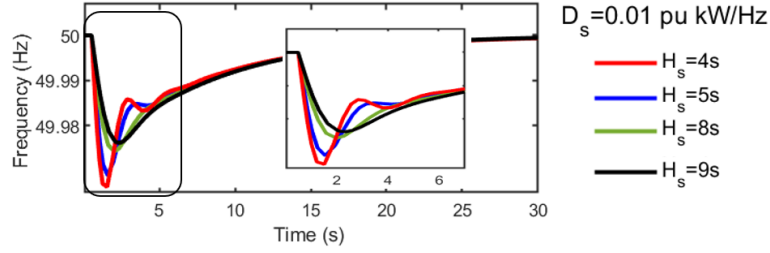
energy capacity than SCESS. The FESS provides 30 kW of short-term peak discharge rate and the SCESS provides a peak power of 10 kW, while the corresponding BESS is designed to provide sufficient energy capacity for going off-grid or to support a given load level. DER 6 supported with only the BESS, shown in Fig. 4.6, has a lower power rating compared to its fast-acting counterparts.

4.4.2 Validation

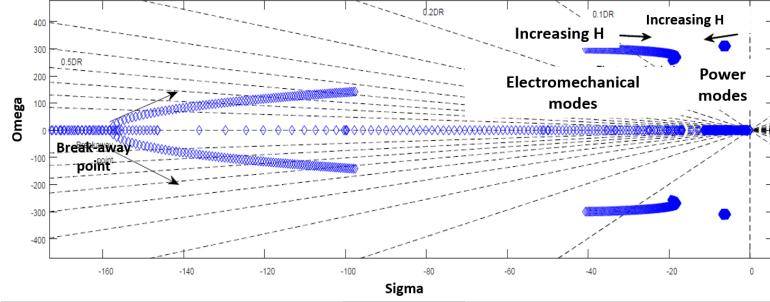
4.4.2.1 Simulations

Time domain simulations are carried out by modeling the microgrid and the inverter controls on MATLAB/Simulink[®]. Initially, we compare the microgrid frequency response when the system inertia varies, as shown in Fig. 4.7a, in the occurrence of a disturbance. It is seen in Fig. 4.7b that the ROCOF and f_{nadir} depend on the inertia coefficient. However, it also determines the peak overshoot and the settling time of the frequency response in 100 % inverter-based low-inertia systems (e.g. $H_s = 4$ s and 5 s). Keeping D constant at 1% p.u, a higher inertia coefficient (e.g. $H_s = 8$ s and 9 s) mitigates the initial ROCOF and f_{nadir} , but increases the peak overshoot and the settling time of the frequency response in Fig. 4.7a.

With the implemented synthetic inertia control, we examine the effect of the inertia parameters on the frequency response using modal analysis in Fig. 4.7b. Based on the control equations, the small-signal model of the inverter control is derived, ignoring the DC side of the model as the MPC controller maintains the DC-link voltage [37]. The modes of the inverter droop control are referred to as *inverter power* modes and the modes of the swing equation-based control that emulate inertia are referred to as the *electro-mechanical* modes since the control is based on a virtual rotor and prime-mover input power. Increase in H_i shifts the inverter power modes towards the left half of the s-plane, thereby stabilizing the system. However, the electro-mechanical modes of the swing-based controller are shifted to the right, decreasing the stability margin of the



(a) Effect of H_s on the Frequency Response.



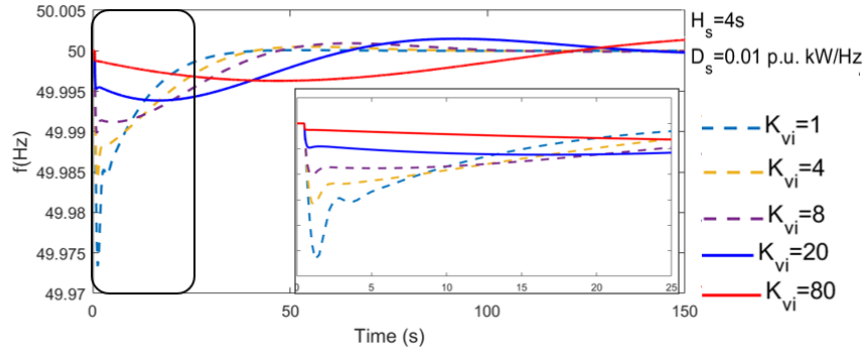
(b) Bifurcation Plot Showing the Effect of an Increasing Inertia.

Fig. 4.7: Effect of the Synthetic Inertia on the System Dynamics.

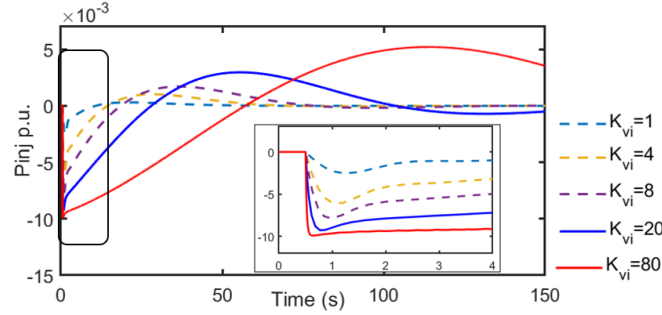
system. Therefore, the inertia and damping parameters have to be traded off for optimal response.

Fig. 4.8 presents the simulation results with the synthetic inertia control using different DERs. Fig. 4.8a presents the frequency responses based on the power rating of the DERs with different synthetic inertia control coefficients K_{vi} . The corresponding aggregated power injected by the DERs is shown in Fig. 4.8b. If K_{vi} is optimized only for the initial ROCOF and f_{nadir} with a high K_{vi} , the frequency response may have a higher peak overshoot and a longer settling time, which decreases the stability margin. A higher K_{vi} also indicates a high power injection from storage reserves, and a higher operating expenditure (OPEX).

Following this, the results of the improved distributed predictive controller have been presented in Fig. 4.9. The ROCOF and the frequency nadir are optimized by a high control coefficient, after what the inertia coefficient is significantly reduced, resulting in a shorter settling time with mitigated oscillation. The power injected by the grid-friendly DERs P_i is limited by P_k^-, P_k^+ for the k^{th} 15-min interval. The optimized K_{vi} base values are shown in Fig. 4.9. The K_{vi} values are designed for the standard ROCOF limit of



(a) Frequency Response with Different Synthetic Inertia Control Coefficients.



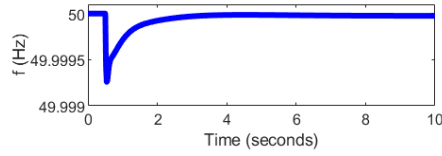
(b) Power Injected by VICs for Fast-Frequency Support.

Fig. 4.8: Synthetic Inertia. Illustration of the Need for MPC.

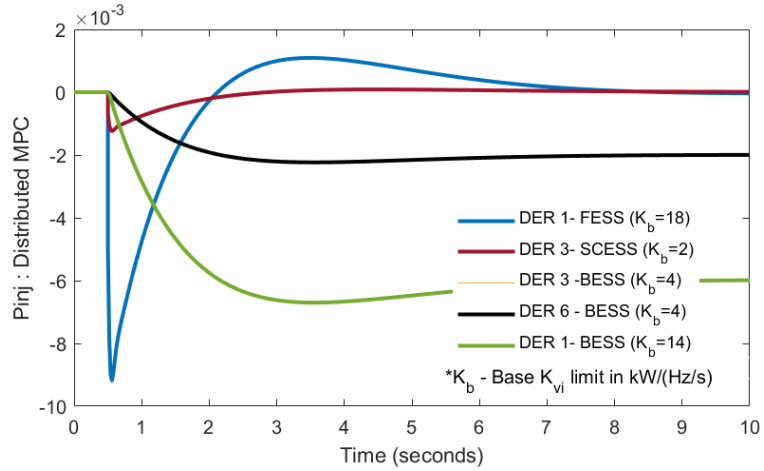
the system, 0.5 Hz/s. If the system ROCOF dips beyond the standard limit, the K_{vi} base values are naturally decreased with the saturation of P_i .

Fig. 4.10 shows the battery and supercapacitor response to maintain the AC-DC power balance by regulating the DC-link voltage with PV variation and AC-microgrid disturbances. The supercapacitor responds to the high-frequency disturbance, while the battery responds to slower disturbances. For the fast-frequency response, we see that the supercapacitor delivers a proper response, while the battery delivers a slower-but-sustained primary frequency response due to its high-energy capacity, but low charge/discharge speed. The hybridization of the storage technology is clearly appropriate in the studied configuration.

In comparison to a conventional virtual droop-inertia controller, which is essentially a proportional-derivative control strategy, the predictive control adaptively tunes the inertia and damping contributions of the DER, thereby leading to an optimal control as shown in Fig. 4.11. If the PID or LQR controllers are tuned to limit the f_{nadir} , it leads to power



(a) Improved Frequency Response Compared to Fig. 4.8a.



(b) Power Injected by MPC D-VICs.

Fig. 4.9: Distributed Predictive Synthetic Inertia Control.

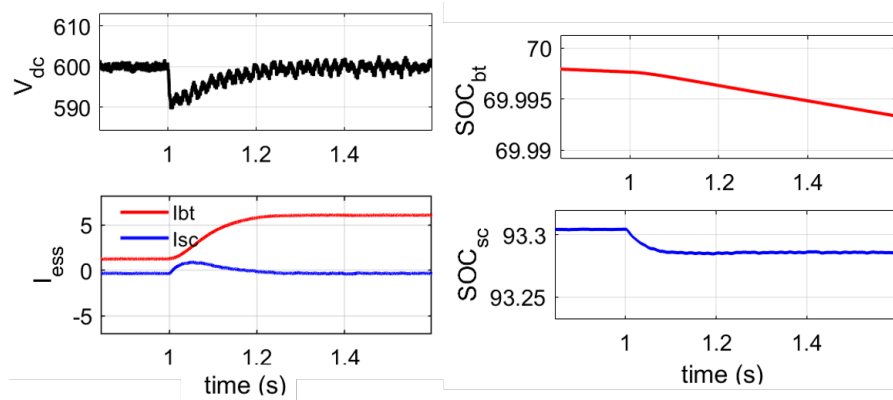


Fig. 4.10: Response Characteristics of the Hybrid Energy Storage.

oscillations and a longer settling time t_s , therefore requiring an additional damping controller which is not an optimal utilization of flexibility reserves. The predictive tuning in MPC allows an optimal scenario without having to trade off the opposing response metrics.

Since the MPC relies on the system model to deliver an optimal performance, model accuracy directly determines the control performance. The parameter changes are updated in the step of distributed optimization in which the DERs are coordinated. In the

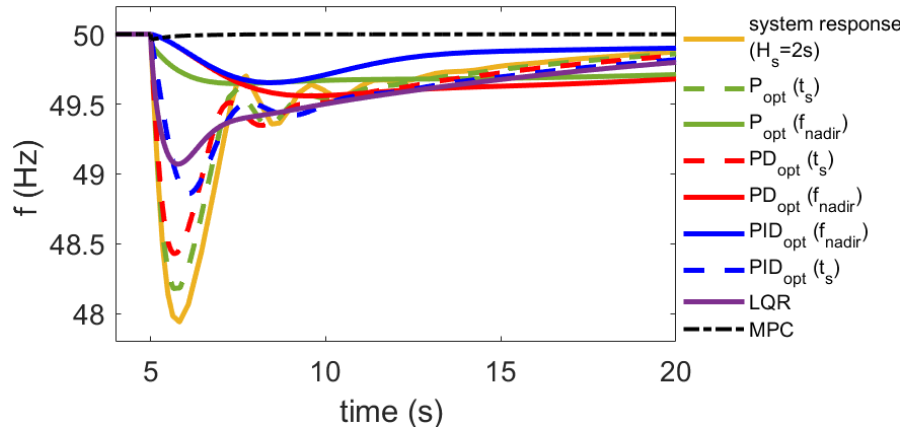


Fig. 4.11: Comparison with other Controllers.

event of unforeseen parameter changes or bad data acquisition for the model, the optimal performance of the controller cannot be guaranteed.

4.4.2.2 Discussion

Given the superior performance of the MPC over the traditional control and other linearized optimal controllers, some restrictive scenarios for the optimal performance are discussed below.

Case 1 Model accuracy plays an important role in the performance of the MPC, hence model-plant mismatch affects the control performance. If model uncertainties can be modelled, they can be accounted for in the MPC using predictive scenarios to account for the worst case, which raises the question of how conservative the control can operate. Accounting for model uncertainties trades off control robustness for a high computing power or a slower control. This can be addressed to an extent by using explicit MPC which relies on pre-simulated scenarios. This comes with the requirement of a sufficient memory and a larger memory in turn comes with the computation time to search a large database of scenarios.

In the proposed framework, as the objective is fast-frequency control, it is essential to maintain the simplicity of the model in MPC computations. So, the system model is

re-identified with the updated parameters in the distributed communication layer along with the DER coordination problem.

Case 2 In the MPC framework introduced in this work, the inertia and damping contribution of the DERs are tuned in real time. It is an optimal control strategy that is not restricted to proportional or derivative response, for which the allocation of resources is not straight forward.

It is to be observed that the derivative response is high on the occurrence of the disturbance and decreases towards the steady state, while the proportional response increases towards the steady state for an optimal response. Hence, to allocate reserves we require a share of fast acting flexibilities with high power (not necessarily high energy) capacity to provide the initial inertia, and sufficient high energy capacity reserves to provide the sustained primary frequency response until corrective actions are taken.

For allocating the power reserve for inertial response, the f_{nadir} has to be determined using the system model in (4.18) for a worst case contingency ΔP_d . The power required from the DER for inertial response can be determined based on the $|f_{nadir}| \leq |f_{limit}|$ constraint of the microgrid. The power required in case of the worst case scenario determines the power capacity of the fast acting flexibilities like the flywheel or supercapacitor storage. It is to be noted that the response time of these resources with the frequency measurement and control has to be low enough to limit the f_{nadir} . The power capacity of the slower reserve can be sized similarly for worst contingency scenario and the primary frequency deviation limits for a designed linear power frequency droop characteristic $\Delta P_d/\Delta f$. The energy capacity can be computed to deliver the calculated power for a 15-minute slot until the corrective action is taken.

An additional case study is presented in Fig. 4.12a, where the MPC response P_{mpc} is curtailed by the maximum power limit of the HESS $P_{hesslim}$. The performance of the MPC is still optimal as the resource constraints can be modelled in the predictive control. The corresponding power injected by the HESS are presented in Fig. 4.12b.

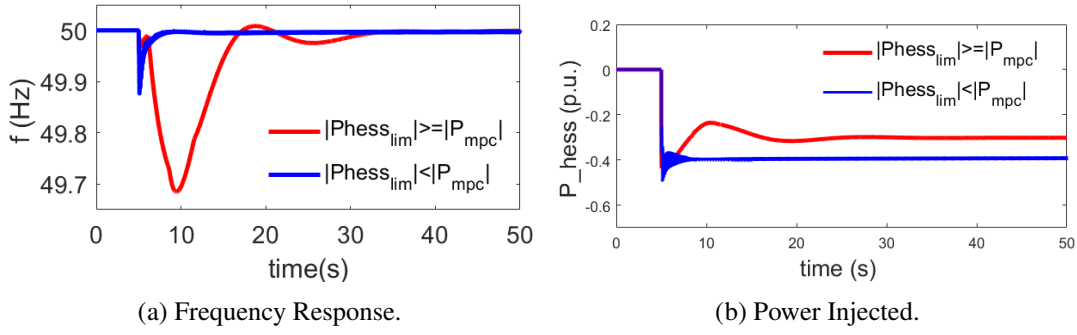


Fig. 4.12: MPC Performance with Flexibility Constraints.

Case 3 Considering the case that one or more of the cooperatively controlled DERs do not implement the proposed MPC inertia tuner, the overall frequency control will be sub-optimal and may require additional damping control in worst cases. One of the grid-friendly DERs with MPC, DER 1 is replaced with an identical DER with a conventional droop-virtual inertia controller. The droop and virtual inertia control coefficients are manipulated to ensure a stable system by small signal analysis. Fig. 4.13 shows the sub-optimal performance where one among the three DERs is not equipped with the MPC inertia tuner.

It is to be noted that the DC-side MPC controls the DC-DC buck-boost converter operating with a switching frequency of 200 kHz, and the AC MPC controls the inverter operating with a switching frequency of 10 kHz, while the frequency response control operates with a sample time of 200 ms. If the faster inner control loops are replaced by PI or other controllers, it does not affect the framework as long as the DC voltage is controlled. However, the MPC implementation can accommodate constraints with better performance and avoids the hardship of tuning the PI controllers for every change in the system.

4.4.2.3 Experimentation

For the real-time validation, we have used a power hardware-in-the-loop (PHIL) platform, shown in Fig. 4.14a. The platform comprises a 5 kW inverter, controlled at a 10 kHz switching frequency by a dSpace[®] controller, supplied by a controllable DC voltage source operating at 700 Vdc. The inverter is controlled in the grid-following or

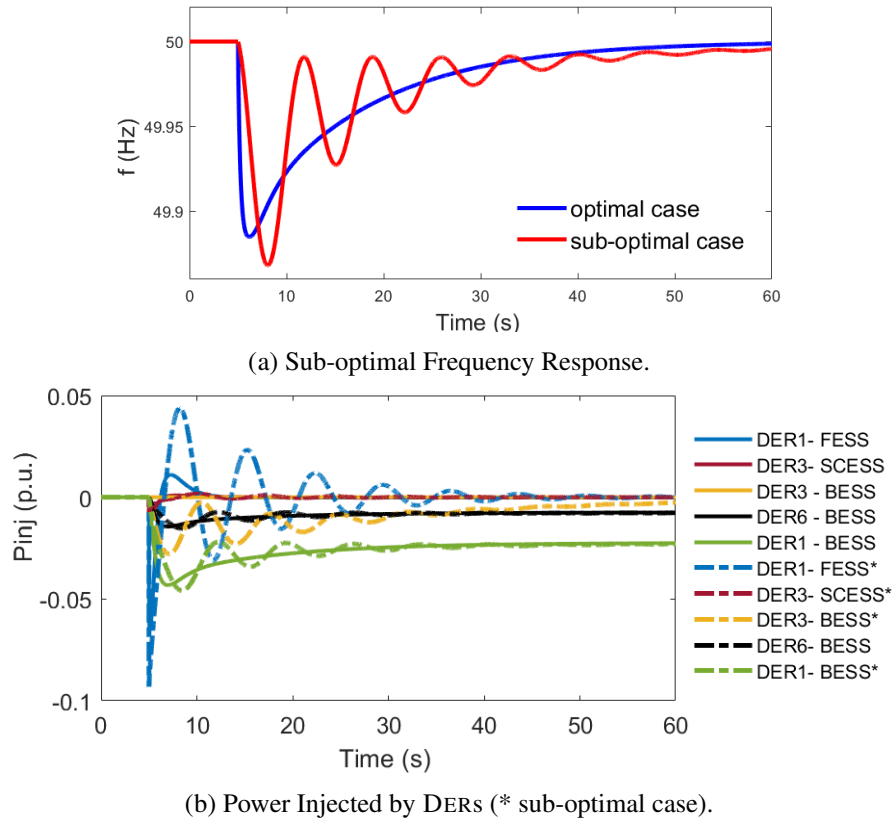
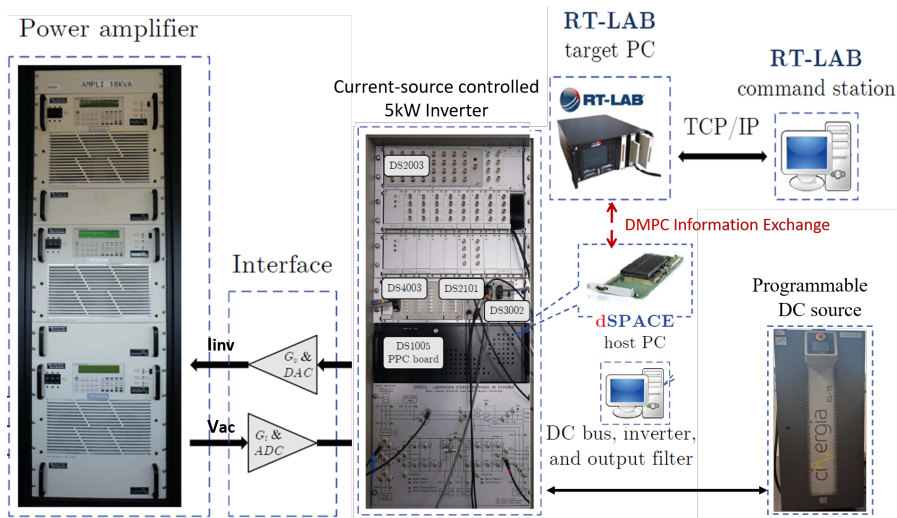


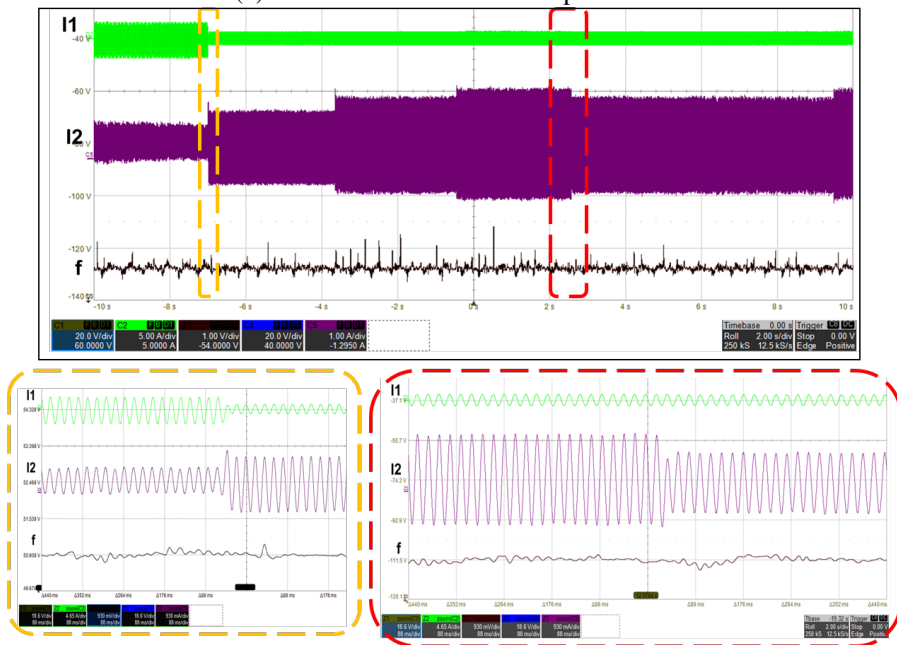
Fig. 4.13: Non-uniform Frequency Control Dynamics among DERs.

current-controlled mode, as discussed in Section 4.2.2. The power amplifier acts as the voltage reference for the inverter control. The power amplifier operates with a nominal power of 6 kW. The output of the power amplifier is manipulated by a OPAL-RT[®] real time simulation target in which the rest of the microgrid with other DERs is simulated.

The waveform recorded in Fig. 4.14b showcases a grid-friendly DER response to a series of disturbances (0.2 p.u. step-load increase, 0.2 p.u. momentary loss of PV generation with gaussian noise, and a step load decrease of 0.1 p.u.) to maintain the frequency balance of the microgrid. The DER inverter I_1 operates as a grid-feeder, which follows a constant power set point over the 15 min sample time, while the grid-friendly DER responds well to the momentary disturbances in the system, maintaining the frequency constant. The first block of waveform shows the response on the grid-friendly DER to the disturbance, while the grid-feeding I_1 does not respond to the disturbance in the constant power mode and decreases with the change in the power set point. The send block shows the response of I_2 to the step load decrease.



(a) Power Hardware-in-the-loop Platform



(b) Experimental Validation of Grid-friendly DER Response.

Fig. 4.14: PHIL Validation.

The waveforms recorded in Fig. 4.15 presents the frequency response of the hybrid energy storage system to a set of real-time simulated PV intermittency and load disturbances emulated by step changes. The BESS supports the steady-state response, while the SCESS supports the transient response of the grid-following DER. For PV disturbance, the output current is maintained with the help of ESS whereas with load disturbance, the output current of the IBR changes for frequency response in scenario A of Fig. 4.15, while scenario B depicts the response of the grid-friendly IBR to a step load

change of 30% of total system load.

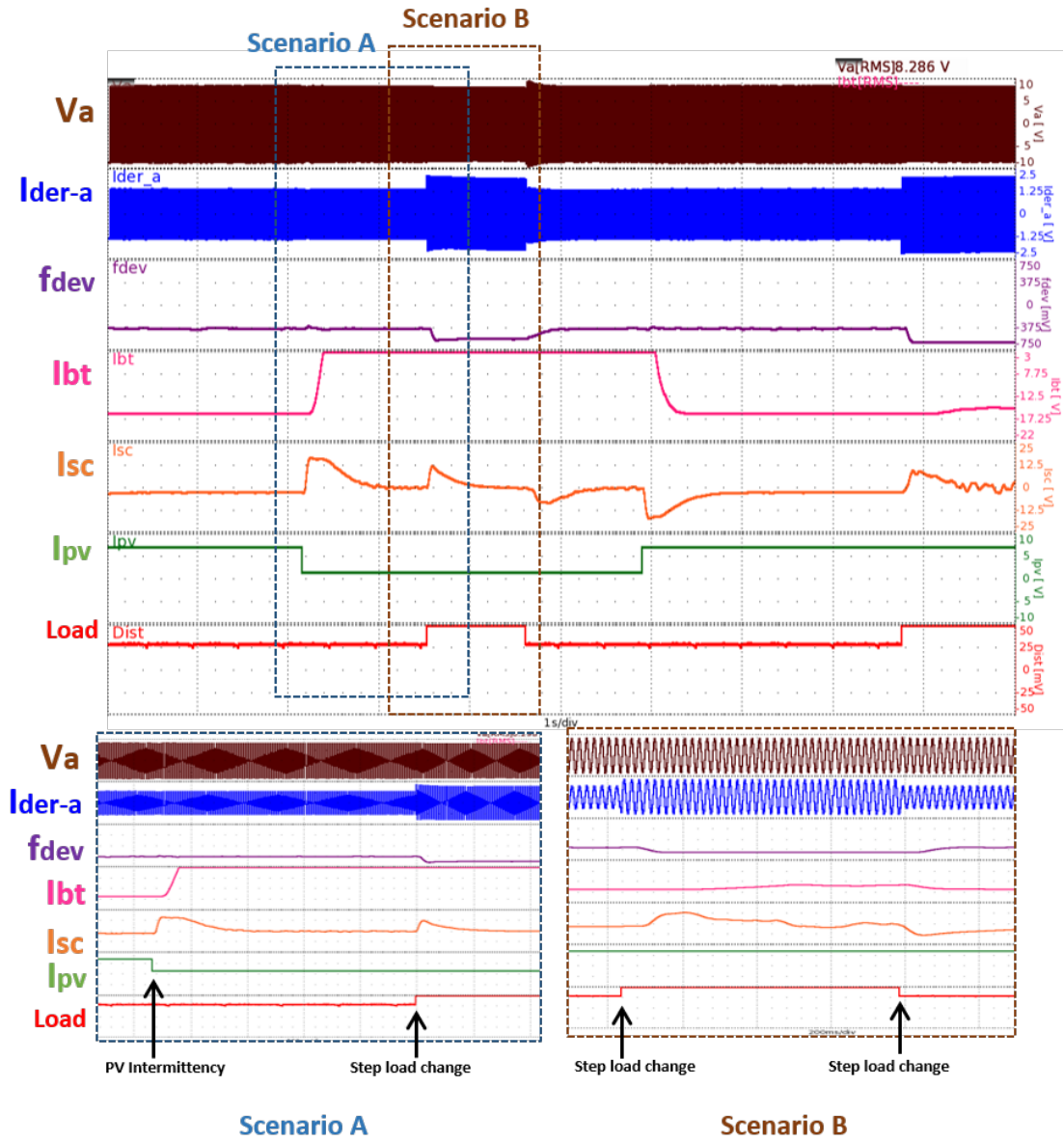


Fig. 4.15: HESS Response Simulating PV and Load Disturbances.

4.5 Chapter Summary

In the proposed control strategy, the inertia coefficients of the IBRs are optimally tuned in real-time by a faster control loop to improve the frequency response metrics such as f_{nadir} , peak overshoot, and the settling time of the frequency transient with the help of

local MPCs. A distributed consensus optimization of inertia coefficients based on the individual resource constraints of grid-friendly DERs, which relies on the presence of a peer-to-peer communication infrastructure.

Although the predictive control enhances the frequency response by tuning the control parameters in real-time, the grid following control topology relies on frequency measurement. Measurements of frequency deviation using PLL or kalman filters involves a delay of 2-3 cycles' time, while the derivative measurement may involve 6-7 cycles' time due to which synthetic inertia emulation poorly compares itself to synchronous inertia. Grid-following DERs are also incapable of operating in the autonomous mode, and so the following chapter discusses a coordinated control framework from grid-forming IBRs, and how it overcomes the requirement for frequency measurements.

Chapter 5

Coordinated Predictive Control of Grid-forming DERs

Grid-forming IBR control is a voltage-source controlled strategy that allows the IBR to serve as a voltage source especially during the autonomous operation mode of the microgrid. Grid-forming frequency control scheme relies on power measurement rather than frequency measurement. This chapter presents the an isochronous and droop-based inverter control for power-frequency response in grid-formers. In the isochronous frequency-control concept, the distributed generation operates at a constant frequency, which renders a zero quasi steady state frequency error Δf_{ss} , whereas the droop control allows for change in frequency to respond to power disturbances. Isochronous frequency control is most-suited for microgrids that use the largest dispatchable unit or a dedicated ESS to respond to load changes. With the help of load sharing algorithms, multiple frequency-responding units can operate in the isochronous mode. The droop concept is most popular in power systems with several frequency responding units as it is a decentralized control with its natural synchronizing property. However, large load shifts could cause a large Δf_{ss} , which has to be restored by the secondary and tertiary layers of the hierarchical frequency control.

In this context, an isochronous load sharing control algorithm for coordinated isochronous model predictive IBR control has been presented in this chapter. The inertia emulation in

the droop method has been implemented with a model predictive tuner for coordinating droop-based grid-forming DERs in IBR microgrids.

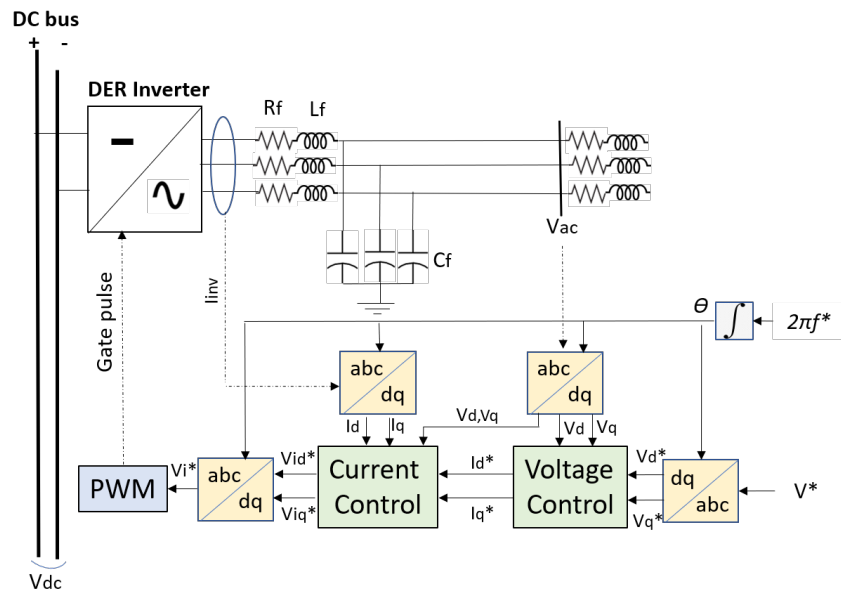
5.1 Isochronous Grid-forming Control

The isochronous grid-formers serve as ideal voltage sources with amplitude V^* and frequency f^* for the autonomous operation of the microgrid. The control scheme of the grid-forming control is shown in Fig. 5.1a with the cascaded $d - q$ controllers in Fig. 5.1b. The external loop controls the voltage output to match the reference amplitude and frequency, while the inner loop regulates the current output of the inverter. As ideal voltage sources, isochronous grid-formers have a very low output impedance and can be considered as the swing bus of the autonomous power system. As dedicated frequency responsive controllers, they require an adequate flexibility on the DC-side of the inverter that can maintain a stable DC voltage while the grid-forming control injects or draws power from the DC bus to maintain the frequency constant. Hence, this control scheme is particularly suitable for islanded microgrids with a single large dispatchable unit or a dedicated ESS assigned for power balancing.

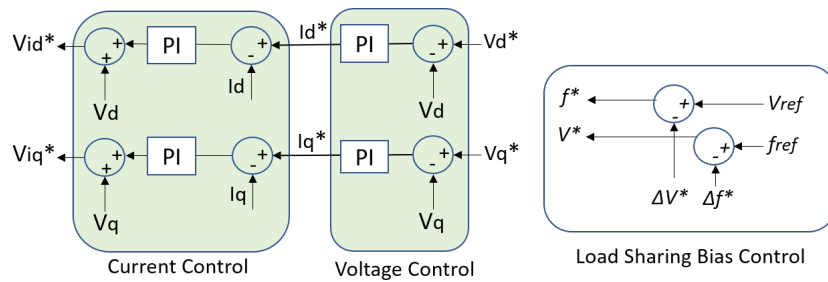
5.1.1 Control Implementation with MPC

Unlike the implementation of grid-forming control with PWM using PI control, the isochronous grid-forming control can be implemented by MPC directly (without PWM) by predicting all possible switching states of the inverter. Similar to the FCS-MPC discussed previously in Section 4.2, the isochronous control is formulated using the finite control set (FCS) optimization. The MPC implementation in the previous chapter has been modified for a voltage-source control of the IBR as shown in Fig. 5.2.

Let the grid-former reference voltage with amplitude V^* and frequency f^* be represented in the $d - q$ synchronous reference frame by (V_d^*, V_q^*) . Similar to the implementation in Section 4.2.2, the inverter may be represented by a discrete non-linear model in terms



(a) Grid-forming Control Scheme



(b) Inner Control Loops and Load Sharing Control.

Fig. 5.1: Isochronous Grid-forming Control.

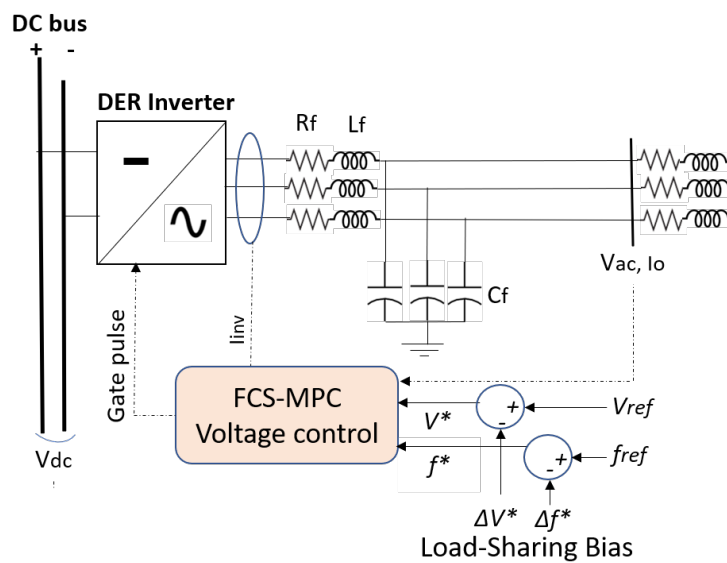


Fig. 5.2: MPC Scheme for Isochronous Grid-formers.

of its switching states (S_a, S_b , and S_c), where a, b , and c represent the IGBT leg of each phase, with 2 states each based on which IGBT is on. The inverter output voltage V_i determined by the switching state vector S is given by (5.1).

$$\begin{cases} S = \frac{2}{3} \left(S_a + S_b e^{j(2\pi/3)} + S_c e^{j(4\pi/3)} \right) \\ V_i = V_{dc} S \end{cases} \quad (5.1)$$

The $L_f C_f$ filter dynamics are modelled in (5.2), I_f and V_c are the filter current and the capacitor voltage respectively.

$$\begin{cases} L_f \frac{dI_{inv}}{dt} = V_i - V_c - I_{inv} R \\ C_f \frac{dV_c}{dt} = I_{inv} - I_o \end{cases} \Rightarrow \dot{\mathbf{x}} = \mathbf{A}\mathbf{x} + \mathbf{B}\mathbf{y}$$

With $\mathbf{x}(k) = \begin{bmatrix} I_{inv}(k) \\ V_c(k) \end{bmatrix}$; $\mathbf{y}(k) = \begin{bmatrix} V_i(k) \\ I_o(k) \end{bmatrix}$; $\mathbf{A} = \begin{bmatrix} -\frac{R_f}{L_f} & -\frac{1}{L_f} \\ \frac{1}{C_f} & 0 \end{bmatrix}$; $\mathbf{B} = \begin{bmatrix} \frac{1}{L_f} & 0 \\ 0 & -\frac{1}{C_f} \end{bmatrix}$ (5.2)

Representing the model (5.2) in the discrete form with sample time t_s and solving the equation, the inverter predictor current equation is then derived as given in (5.3).

$$\mathbf{x}(k+1) = e^{\mathbf{A}t_s} \mathbf{x}(k) + \left[\int_0^{t_s} e^{\mathbf{A}\tau} \mathbf{B} d\tau \right] \mathbf{y}(k)$$

$$V_c(k+1) = e^{\mathbf{A}t_s} \mathbf{x}(k) + \mathbf{A}^{-1} (e^{\mathbf{A}t_s} - I) \mathbf{B} \mathbf{y}(k) \text{ With } e^{\mathbf{A}t_s} = \begin{bmatrix} e^{\frac{R_f t_s}{L_f}} & -e^{\frac{t_s}{L_f}} \\ e^{\frac{t_s}{C_f}} & 1 \end{bmatrix} \quad (5.3)$$

5.1.1.1 FCS Optimization

The reference tracking is implemented with the MPC controller by optimizing the objective function given in (5.4) subject to the inverter maximum current limit I_{lim} based on the inverter rating or DC power constraint, with 7 distinct control sets based on the possible inverter switching states.

$$\min \sum_{k=1}^{N-1} \left[(V_{c-d}^*(k+1) - V_{c-d}(k+1))^2 + (V_{c-q}^*(k+1) - V_{c-q}(k+1))^2 \right] \quad (5.4)$$

The predicted voltage across the capacitor is represented in the $d - q$ reference frame as $(V_{c-d}(k+1), V_{c-q}(k+1))$. The decision variables of the optimization are $\{S_a, S_b, S_c\}$.

5.1.2 Synchronizing Control for Microgrid Transition

In the islanded or autonomous mode, the grid-forming inverters are the main voltage sources of the microgrid. With the transition of the microgrid to grid-tied mode, if the grid-forming IBRs are switched to the grid-following mode and vice versa for the transition to the autonomous mode, a phase angle synchronization control is required. Fig. 5.3 depicts the IBR control in the grid-connected and islanded mode of the microgrid.

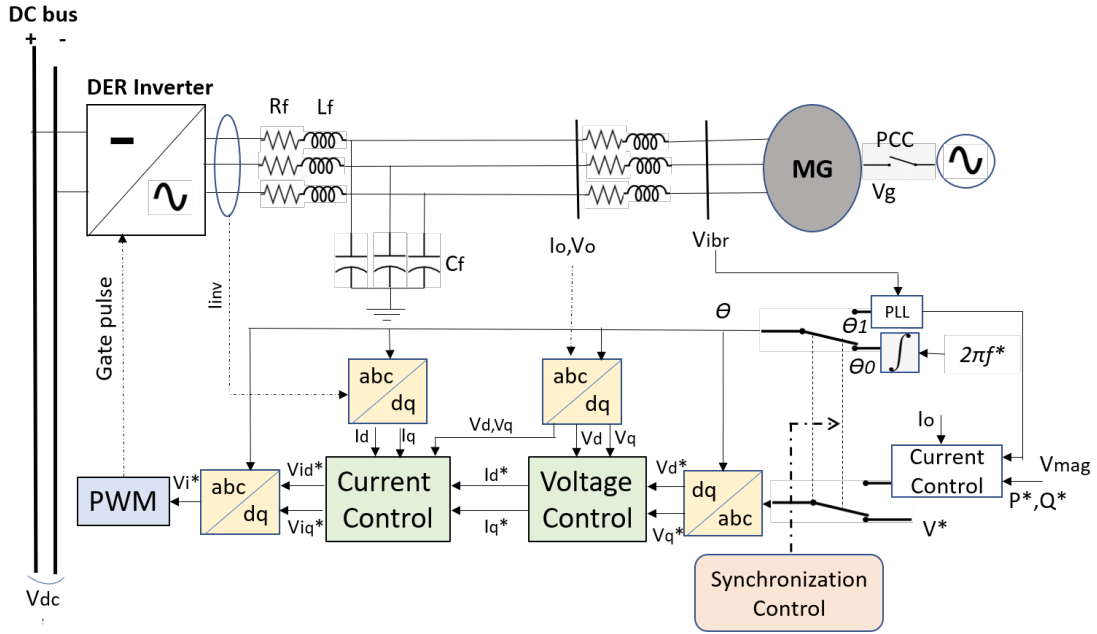


Fig. 5.3: IBR Multi-mode Control for Microgrid Transition

When the point of common coupling (PCC) breaker is closed, the microgrid is operated in the grid-connected mode with angle θ_1 and voltage reference based on power set-points (P^*, Q^*) as shown in Fig. 5.3. This is known as the grid-following mode and has been discussed in detail in Chapter 4. When the PCC is open, the IBR is operating in the grid-forming mode as discussed in Section 5.1, where the angle reference is given by θ_0 and the voltage reference is set as the nominal voltage V^* or may be given by the droop control to be discussed in the following section. For a planned microgrid transition,

there will be necessary changes in the reference voltage. However the angle transition may be controlled for a smooth transition by regulating the angle difference between θ_0 and θ_1 during the transition and by slowing correction of θ_0 which is set in the IBR control [157]. The synchronization control block shown in Fig. 5.3 regulates the angle difference for a smooth transition.

$$\begin{cases} \cos(\phi_d) = \frac{2m}{3} ; m = V_a^* V_{ibr,a} + V_b^* V_{ibr,b} + V_c^* V_{ibr,c} \\ \sin(\phi_d) = \frac{-2m-4n}{3\sqrt{3}} ; n = V_a^* V_{ibr,b} + V_b^* V_{ibr,c} + V_c^* V_{ibr,a} \end{cases} \quad (5.5)$$

For the disconnection of the microgrid, the angle difference ϕ_d between V_{ibr} in p.u. and the grid-forming reference voltage V^* in p.u. is computed based on the sine and cosine values and their polarities given by (5.5). On disconnection, the initial reference angle of the grid-forming control is given by $\theta'_0 = \theta_0 + \int \phi_d$ [157].

For the reconnection of the microgrid to the main grid, the angle difference $\phi_r = \theta_g - \theta_{ibr}$ between the PCC voltage V_g in p.u. and the IBR output voltage V_o in p.u. is computed using (5.6), where θ_g and θ_{ibr} are obtained from the respective PLLs. A PI control may be employed to regulate ϕ_r to zero by controlling $\Delta\theta_0$.

$$\begin{cases} \phi_r \approx \sin(\phi_r) = \frac{-2p-4q}{3\sqrt{3}} \\ p = V_{g,a}V_{o,a} + V_{g,b}V_{o,b} + V_{g,c}V_{o,c} ; q = V_{g,a}V_{o,b} + V_{g,b}V_{o,c} + V_{g,c}V_{o,a} \end{cases} \quad (5.6)$$

5.1.3 Coordinating Isochronous Grid-formers

When multiple DERs are operating in parallel with the isochronous control, each of the DERs compete to respond to the disturbance first and to compensate the entire imbalance causing overloading of one DER over the others as the isochronous control lets the DERs compete to respond to the disturbance immediately. Therefore, for a stable operation of multiple isochronous grid-formers, a load-sharing algorithm is required as shown in Fig. 5.1b. The algorithm regulates the power sharing among the isochronous DERs by a bias signal that acts a feedback to the isochronous reference frequency f^* set in the

grid-forming control. The bias points are computed dynamically for active load sharing for each unit by load power measurement. These setpoints are rapidly varied as the system settles to a new steady state post-disturbance [158]. Isochronous load sharing is feasible for a microgrid with large load clusters and a precise number of grid-formers connected at the same bus (considering low electrical distance between loads and units) as it requires load measurement and a communication network between units. The frequency and voltage bias points Δf_i^* and ΔV_i^* of the i^{th} isochronous grid-former are given by (5.7) and (5.8) respectively, where P_i and S_i are the active power output and the rating of the i^{th} isochronous grid-former, S_s is the system base power, and P_l and Q_l are the measured power at the n_l load buses close to the point of connection of the grid formers. K_{iso-p} and K_{iso-q} are coordinately set load-sharing coefficients in the dispatch control based on the available resources of the participating units using communication network between grid-forming units. The coordination of the load-sharing coefficients is implemented using the consensus approach described in Section 4.3.2, where the collective decision variable vector $Z = (K_{iso-p}, K_{iso-q})$.

$$\Delta f_i^* = K_{iso-p} \left(\frac{\sum_{l=1}^{n_l} P_l}{S_s} - \frac{P_i}{S_i} \right) \quad (5.7)$$

$$\Delta V_i^* = K_{iso-q} \left(\frac{\sum_{l=1}^{n_l} Q_l}{S_s} - \frac{Q_i}{S_i} \right) \quad (5.8)$$

Frequency de-tuning is effectively a form of droop but with the help of the communication network. Therefore, especially for scenarios with a large number of participating DERs droop control is the obvious choice for a stable system with less dependence on the communication network for the fast frequency response. For islanded operation, there can be an isochronous unit if there is a dedicated resource with adequate flexibility, supported by droop-controlled grid-forming or grid following DERs [50]. Although there maybe multiple grid-formers in this scenario, the droop controlled DERs share the load based on the droop setting, while the isochronous unit restores the Δf_{ss} .

5.2 Grid-forming Droop Control

The droop-controlled grid-formers act as voltage sources for the microgrid. They respond to load changes by regulating their output voltage and frequency, thereby facilitating power sharing amongst the units. The grid-forming units are those that contribute to a high fraction of the microgrid generation. Droop control implements a linear relationship between $P - f$ and $Q - V$ in the phasor domain which enables power sharing in a decentralized manner. In the conventional droop law in (5.9), the droop coefficient m_p establishes a linear relation between the active power and frequency pair and n_q establishes the reactive power and voltage linear relation. This droop law is based on the assumption that the system impedance is predominantly inductive, which is not the case of low voltage distribution networks. This aspect is addressed in sub-sections 5.2.1 and 5.2.2.

$$\Delta\omega = -m_p\Delta P ; \Delta V = -n_q\Delta Q \quad (5.9)$$

A typical inverter droop control scheme has been presented in Fig. 5.4a. The droop block in Fig. 5.4b measures the averaged values of real and reactive power given by (5.10) and (5.11) respectively. The active and reactive power measurements P and Q are computed from the inverter output current i_o and voltage v_o . The measured voltages and currents are represented in the $d - q$ reference frame as (v_{od}, v_{oq}) and (i_{od}, i_{oq}) respectively. In order to avoid the harmonics in the measurements from propagating to the control, a low pass filter (LPF) with corner frequency ω_c has been provided. The frequency and the voltage references are then generated based on the droop laws (5.12), where ω_n and V_n represent the nominal frequency and voltage, P_{nom} and Q_{nom} are the nominal power outputs.

$$P = \frac{\omega_c}{s + \omega_c} (v_{od}i_{od} + v_{oq}i_{oq}) \quad (5.10)$$

$$Q = \frac{\omega_c}{s + \omega_c} (v_{od}i_{oq} - v_{oq}i_{od}) \quad (5.11)$$

$$\omega = \omega_n - m_p(P - P_{nom}) ; v_{od}^* = V_n - n_q(Q - Q_{nom}) \quad (5.12)$$

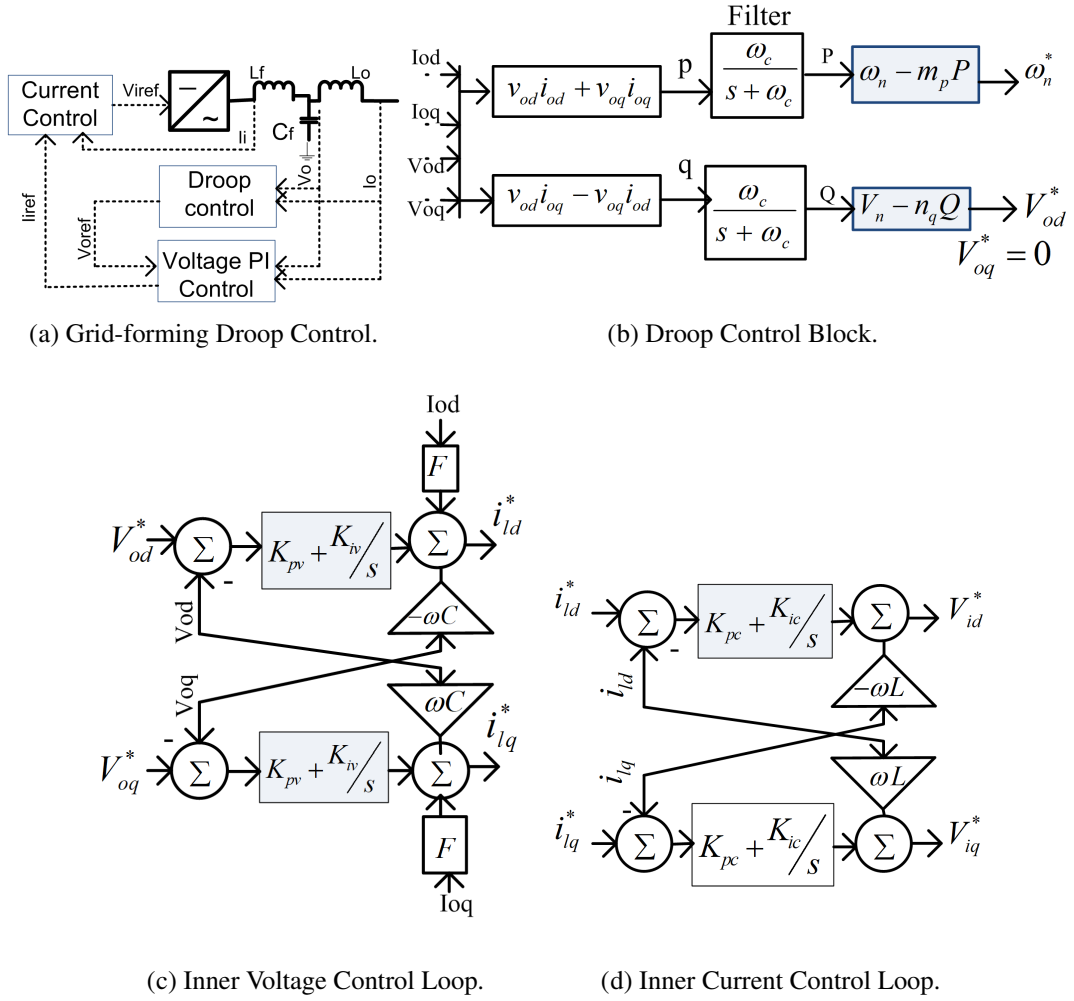


Fig. 5.4: Inverter Droop Control Schematic.

The inverter is connected to the bus through an LCL filter with components r_f , L_f , C_f , r_c , and L_c . The voltage reference generated by the droop block, (v_{od}^*, v_{oq}^*) is fed to the inner voltage loop controller in Fig. 5.4c which computes the output current reference for the inverter given by (5.13)-(5.16). The corresponding PI control parameters are K_{pv} and K_{iv} .

$$\phi_d = \int (v_{od}^* - v_{od}) \quad (5.13)$$

$$\phi_q = \int (v_{oq}^* - v_{oq}) \quad (5.14)$$

$$i_{ld}^* = F i_{od} - \omega_n C_f v_{oq} + K_{pv} (v_{od}^* - v_{od}) + K_{iv} \phi_d \quad (5.15)$$

$$i_{lq}^* = F i_{oq} + \omega_n C_f v_{od} + K_{pv} (v_{oq}^* - v_{oq}) + K_{iv} \phi_q \quad (5.16)$$

The current reference i_{ld}^* and i_{lq}^* is fed to the current control loop in Fig. 5.4d to generate the inverter output voltage reference before the LCL filter as given by (5.17)-(5.20). The corresponding PI control parameters are K_{pc} and K_{ic} .

$$v_d = \int (i_{ld}^* - i_{ld}) \quad (5.17)$$

$$v_q = \int (i_{lq}^* - i_{lq}) \quad (5.18)$$

$$v_{id}^* = -\omega_n L_f i_{lq} + K_{pc} (i_{ld}^* - i_{ld}) + K_{ic} v_d \quad (5.19)$$

$$v_{iq}^* = \omega_n L_f i_{ld} + K_{pc} (i_{lq}^* - i_{lq}) + K_{ic} v_q \quad (5.20)$$

5.2.1 Droop Laws with System Impedance

The $P - f, Q - V$ droop law is valid only under the assumption of a predominantly inductive impedance, however the line impedances of the rural distribution network, tend to be more resistive as voltage drops [159] or even complex [160]. The control variables of voltage source inverters are the output AC voltage magnitude V_o and electric pulsation ω . For each inverter to respond to the changing load, its active P and reactive power Q is given by (5.21). Z indicates the impedance magnitude and θ indicates the impedance angle. These approximate expressions are derived from the power flow equations under the assumption that the phase difference between the inverter output voltage V_i and the microgrid nodal voltage V_g . ϕ is very small and typically inferior to 1° . Based on the type of system impedance, Table 5.1 establishes the linear relationship for each impedance type based on the approximate expressions of P and Q . Hence, the appropriate droop relation for a known system impedance can be derived from this table. The relations in the table are obtained by substituting the respective impedances and simplifying (5.21).

$$\begin{cases} P \approx (V_i(V_g - V_i) \cos \theta + V_i V_g \phi \sin \theta) / Z \\ Q \approx (V_i(V_g - V_i) \sin \theta - V_i V_g \phi \cos \theta) / Z \end{cases} \quad (5.21)$$

Table 5.1: Droop Relations for Different System Impedances.

	P - Q Relations	Droop Laws
L $\theta \approx 90^\circ$	$P \simeq V_g V_i \phi / X$ $Q \simeq V_g (V_i - V_g) / X$	$\omega = \omega_n - m_p P$ $V_i = V_n - n_q Q$
RL $\theta \approx 45^\circ$	$P - Q \simeq \sqrt{2} V_g V_i \phi / Z$ $P + Q \simeq \sqrt{2} V_g (V_i - V_g) / Z$	$\omega = \omega_n - m(P - Q)$ $V_i = V_n - n(P + Q)$
R $\theta \approx 0^\circ$	$P \simeq V_g (V_i - V_g) / R$ $Q \simeq -V_g V_i \phi / R$	$V_i = V_n - n_p P$ $\omega = \omega_n + m_q Q$
RC $\theta \approx -45^\circ$	$P + Q \simeq -\sqrt{2} V_g V_i \phi / Z$ $P - Q \simeq \sqrt{2} V_g (V_i - V_g) / Z$	$\omega = \omega_n + m(P + Q)$ $V_i = V_n - n(P - Q)$
C $\theta \approx -90^\circ$	$P \simeq -V_g V_i \phi / X$ $Q \simeq -V_g (V_i - V_g) / X$	$\omega = \omega_n + m_p P$ $V_i = V_n + n_q Q$

5.2.2 Virtual Impedance

The system impedance comprises the line, load and the inverter output impedance. Low-voltage distribution networks have a high R/X ratio [159], while the inverter output impedance is mainly inductive due to the output LC or LCL filters. The system impedance is therefore subject to change based on the microgrid control and operation. In order to establish the droop law, virtual impedance techniques [160] are used to manipulate the system impedance. The inverter output impedance can be modified to become a resistance by adding a negative proportional feedback from the output current I_o to the inverter reference output voltage V'_o , to give the modified reference V_o^* . Similarly, a negative derivative feedback emulates an inductive voltage drop and a negative integral feedback emulates a capacitive voltage drop as shown in (5.22).

$$V_o^* = V'_o - \left(R_v + \frac{\omega_v}{s + \omega_v} L_v s + \frac{C_v}{s} \right) \times I_o \quad (5.22)$$

The resistive system impedance remains constant for all frequency ranges and automatically shares the harmonic power. A high value for the virtual resistance R_v (i.e. well above the line impedance range) renders the system impedance resistive and insures

power sharing even for large load shifts. However, a very large value of R_v may result in a sluggish response. Thus, the value of R_v is chosen with the criteria such that the system impedance angle is considerably low for the line impedance with the lowest R/X .

5.2.3 Active damping

The droop relationships given in Table 5.1 are linear relationships which trade the voltage-frequency ($V-f$) regulation for power sharing accuracy. The droop coefficients are therefore calculated according to the steady-state requirements of the system, therefore leaving no degree of freedom to design the damping.

Based on the droop law, the closed loop transfer functions (CLTF) of the P_i and Q_i expressions, (5.23), are given by (5.24) and (5.25).

$$\begin{cases} P_i &= (V_i^2 - V_i V_g \cos(\delta_i - \delta_g)) / R \\ Q_i &= (V_i V_g \sin(\delta_i - \delta_g)) / R \end{cases} \quad (5.23)$$

H_{p1} , H_{p2} , and H_q terms in the CLTF are given by (5.26), (5.27), and (5.28) respectively.

$$\Delta P_i(s) = \frac{H_{p1}}{1 + n_p H_{p1}} \Delta V_i(s) + \frac{H_{p2}}{1 + n_p H_{p1}} \Delta V_g(s) \quad (5.24)$$

$$\Delta Q_i(s) = \frac{H_q}{s - m_q H_q} \Delta \omega_i(s) + \frac{H_q}{s - m_q H_q} \Delta \omega_g(s) \quad (5.25)$$

$$H_{p1} = (2V_i - V_g \cos(\delta_i - \delta_g)) / R \quad (5.26)$$

$$H_{p2} = -(V_i \cos(\delta_i - \delta_g)) / R \quad (5.27)$$

$$H_q = -(V_i V_g \sin(\delta_i - \delta_g)) / R \quad (5.28)$$

The small signal model of the Q droop control yields the critical eigenvalue $\lambda_{q_i} = m_q H_q$ that depends on m_q for Q_i . However, the P eigenmode is not controllable as H_{p1} and H_{p2} are functions of the system impedance, the linearization point, and δ_i , which is in turn affected by the reactive power control [161]. The droop equations may be modified

with active damping terms n_{p1} and m_{q1} as shown in (5.29) and (5.30), where V_n and ω_n are the nominal values of voltage and frequency. The small signal stability of the modified control gives the new critical eigenvalues, (5.31) and (5.32) which may be controlled using the active damping terms without affecting the droop settings that affect the steady-state requirements.

$$V_i = V_n - n_p P_i - n_{p1} (dP_i/dt) \quad (5.29)$$

$$\omega = \omega_n + m_q Q_i + m_{q1} (dQ_i/dt) \quad (5.30)$$

$$\lambda_{p_i} = -(1 + n_p H_{p1}) / (n_{p1} H_{p1}) \quad (5.31)$$

$$\lambda_{q_i} = (m_q H_q) / (1 + m_{q1} H_q) \quad (5.32)$$

5.2.4 Inertia Emulation

Inertia emulation may be implemented in the inverter droop control by simply adding a rate limiter to the controlled frequency reference signal to curtail the ROCOF to a preset limit, or by using an LPF to slow down the speed of response of the system to contingencies in [48]. If the active power output of the inverter is measured with the help of a low pass filter with time constant $T_f = 1/\omega_c$, the droop equation (5.33) may be re-arranged as (5.34) to compute the equivalent inertia and damping of the droop controller as given by (5.35), where, P_b is the base power output of the textscder.

$$\omega_i^* = \omega_n - m_p \left(\frac{P}{(1 + T_f s)} - P_b \right) \quad (5.33)$$

$$P_b - P = \frac{T_f}{m_p} s(\omega_i^*) + \frac{\omega_i^* - \omega_n}{m_p} \quad (5.34)$$

$$J = \frac{T_f}{m_p}; D = \frac{1}{m_p} \quad (5.35)$$

VI contribution by the LPF of droop control in (5.34) is not fully controllable and the ratio J/D is constant for a system. The inability to independently control inertia of the unit is overcome by formulating a swing equation in the control as presented below. The swing equation of a synchronous generator can be written as shown in (5.36), where J

is the inertia coefficient, D is the damping, and P_{in} can be regarded as the virtual input power.

$$\begin{cases} -Jm_p \frac{dP}{dt} + D(\omega_n - m_p P) = \frac{P_{in} - P}{\omega_0} \\ P_{in} = P - \frac{(\omega_n - \omega)}{m_p} \end{cases} \quad (5.36)$$

By implementing the swing equation in the droop control, the reference frequency to the controller can be written as (5.37), where C_t is used to represent the expression in p.u. of frequency. Similar to a low pass filter, if $t_0 = J/D$, (5.37) may be written in time-domain as (5.38). It is evident from the time domain equation that by implementing the swing equation, an additional damping term $t_0 m_p$ appears. This results in additional damping in the system. Therefore, the controller can now provide both inertia and damping once the swing equation is incorporated. From (5.38), it can also be shown that if $t_0 > 1/\omega_c$ and $t_0 < 1/\omega_c$, the power response of the IBR is underdamped and overdamped respectively. The opposite for the frequency profile, due to which a trade-off has to be made in the choice of the parameters [48], which essentially leads us to the need for predictive control, similar to that of Chapter 4.

$$\omega_i^* = \frac{1}{C_t} \left(1 + s \frac{J}{D} \right) \left(\omega_n - m_p \frac{\omega_c}{s + \omega_c} P_i \right) \quad (5.37)$$

$$\frac{d\omega_i}{dt} + \omega_c \omega_i = \frac{1}{C_t} \left(\omega_c \omega_n - \omega_c m_p P_i - t_0 m_p \omega_c \frac{dP_i}{dt} \right) \quad (5.38)$$

5.3 Coordinated Predictive Framework

In the MPC implementation of the controller inner controllers can be formulated similar to that of the isochronous control in Section 5.1.1, however the reference voltage and frequency are obtained from the droop equation for FFR and the swing-based formulation in (5.37) for inertia emulation and damping control. Fig. 5.5 represents an IBR with the frequency grid-forming control. The inverter controller involves the droop, damping, and inertia parameters which affect the evolution of the frequency response. Hence, we propose an MPC tuner that predictively optimizes the frequency response of the microgrid with the limited flexibility resources.

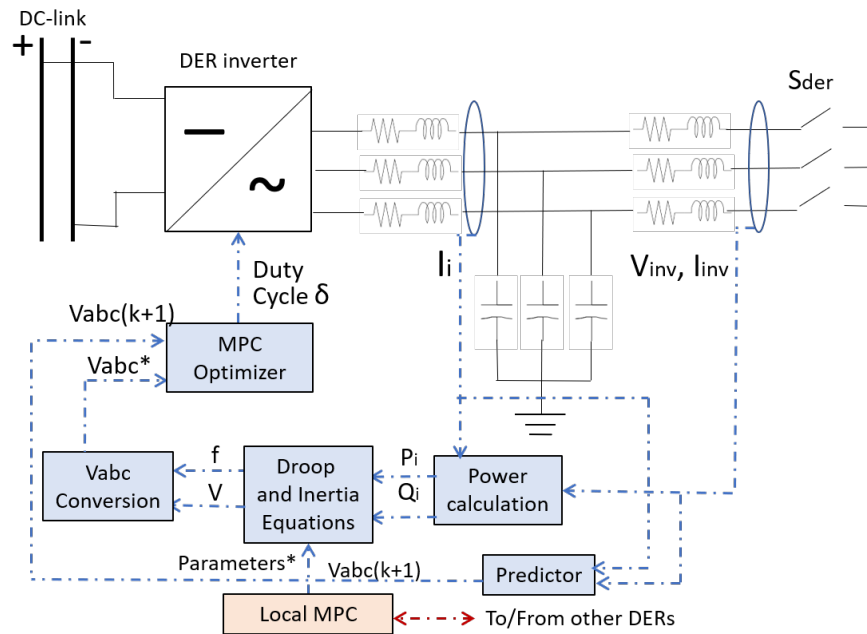


Fig. 5.5: Droop and Inertia Emulation with MPC Tuner

Fig. 5.6 presents the overall MPC scheme. An MPC primarily comprises the system model, a disturbance predictor and the optimizer. The system has to be represented as a discrete time linear or non-linear model to predict the system states X for a given set of input trajectories U for a chosen number of samples N , known as the prediction horizon. The accuracy of the MPC control is determined by the model accuracy. The linearized microgrid model allows the prediction of the evolution of the state variables over the prediction horizon using the measured frequency. The power disturbance is measured and projected to the prediction horizon by a disturbance predictor. The disturbance prediction used in this work assumes that the disturbance remains constants for the next sample time. We consider this method as the forecasting is on a very short term and complex disturbance forecast can deteriorate the control performance as we target the fast-frequency control problem.

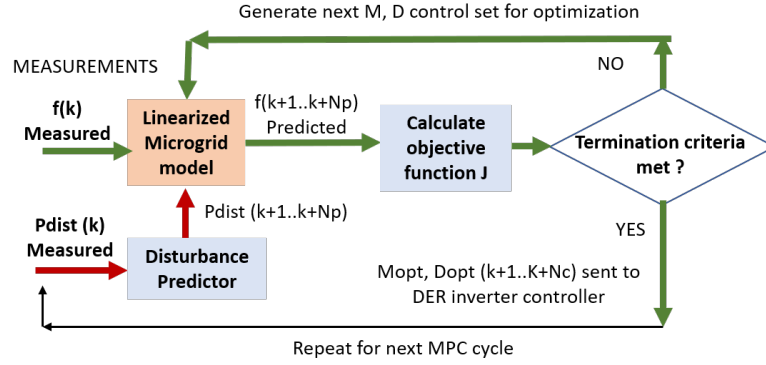


Fig. 5.6: Schematic Diagram of the Local MPC.

5.3.1 System Model

The MPC heavily relies on the plant model for projecting the state variables over the prediction horizon. Hence, the higher the accuracy of the model, the better is the performance. With a non-linear system, accurate non-linear models such as deep neural network models could be used for their high accuracy. However, in the context of fast-frequency control, the control computation time is clearly crucial than the control accuracy. Hence, a simple linear state-space model and a simple optimization is more practical.

The overall microgrid transfer function can be represented by (5.42), where the individual transfer functions $G_d(s)$, $G_{ff}(s)$, $G_{vic}(s)$ represent the different types of converters in the microgrid: the slow droop converters, the fast-acting primary frequency responsive units, and the inertial-response units respectively.

$$G_{d_i}(s) = \frac{k_i}{R_i} \frac{1}{(1 + sT_d)} \quad (5.39)$$

$$G_{ff_i}(s) = \frac{k_i}{R_i} \frac{1}{(1 + sT_{ff})} \quad (5.40)$$

$$G_{vic_i}(s) = \frac{sM_i + D_i}{(1 + sT_{vic})} \quad (5.41)$$

By neglecting the fast-frequency and inertia control time constants as in (5.43) as in [59], the overall plant transfer function is reduced to (5.44).

$$G(s) = \frac{\omega(s)}{\Delta P_e(s)} = \left(\sum_{i \in N_d} G_{d_i}(s) + \sum_{i \in N_{ff}} G_{ff_i}(s) + \sum_{i \in N_{vic}} G_{vic_i}(s) \right)^{-1} \quad (5.42)$$

$$T_p \gg T_{ff}, T_{vic} \approx 0 \quad (5.43)$$

$$G(s) = \frac{1 + sT_d}{MT_d s^2 + (M + (D - R_d)T_d)s + D} \quad (5.44)$$

The aggregated system inertia M given by (5.45) and the aggregated system droop characteristic D given by (5.49) form the control parameters. In the cooperative control, the overall system parameters can be altered by collectively utilizing the distributed resources, subject to their individual constraints modelled in the previous subsection.

$$M = \sum_{i \in N_{vic}} \frac{M_i P_i}{P_b} \quad (5.45)$$

$$D_{vic} = \sum_{i \in N_{vic}} \frac{D_i P_i}{P_b} \quad (5.46)$$

$$R_{ff} = \sum_{i \in N_{ff}} \frac{k_i P_i}{R_i P_b} \quad (5.47)$$

$$R_d = \sum_{i \in N_d} \frac{k_i P_i}{R_i P_b} \quad (5.48)$$

$$D = D_{vic} + R_{ff} + R_d \quad (5.49)$$

On applying a disturbance of ΔP_{dist} , the plant characteristic equation can be given by (5.50) and the state space representation is given by (5.51).

$$\frac{\Delta P_{dist}}{MT_d} = \ddot{\omega} + 2\zeta \omega_n \dot{\omega} + \omega_n^2 \omega \quad (5.50)$$

$$\begin{bmatrix} \Delta \dot{\omega} \\ \Delta \ddot{\omega} \end{bmatrix} = \begin{bmatrix} 0 & I \\ -\frac{D}{MT_d} & -\left(\frac{1}{T_d} + \frac{D - R_d}{M}\right) \end{bmatrix} \begin{bmatrix} \Delta \omega \\ \Delta \dot{\omega} \end{bmatrix} + \begin{bmatrix} 0 \\ \frac{\Delta P}{MT_d} \end{bmatrix} \quad (5.51)$$

5.3.2 Rate-based Linearization of the Model

The MPCs rely on a linear discretized state space model to perform the predictive optimization around specific operation points [91]. In this work we modify the conventional linearized state space equations (5.52) into that of the RB domain (5.53), where, x_k, u_k, d_k, y_k , and r_k indicate the state, control, disturbance, output, and output reference vector respectively at the k^{th} sample time.

$$\begin{cases} x_{k+1} = Ax_k + B_1u_k + B_2d_k \\ y_k = Cx_k + D_1u_k + D_2d_k \\ e_k = y_k - r_k \end{cases} \quad (5.52)$$

$$\begin{cases} \xi_{k+1} = \bar{A}\xi_k + \bar{B}_1\Delta u_k + \bar{B}_2\Delta d_k \\ y_k = Cx_k + D_1(u_{k-1} + \Delta u_k) + D_2(d_{k-1} + \Delta d_k) \\ e_k = y_k - r_k \\ \xi = \begin{bmatrix} x_k - x_{k-1} \\ e_k \end{bmatrix} \\ \bar{A} = \begin{bmatrix} A & 0 \\ C & I \end{bmatrix}; \bar{B}_1 = \begin{bmatrix} B_1 \\ D_1 \end{bmatrix}; \bar{B}_2 = \begin{bmatrix} B_2 \\ D_2 \end{bmatrix} \end{cases} \quad (5.53)$$

The RB-MPC optimization objective is to minimize (5.54), subject to the state update equation of (5.53) and input bound constraints. The first term of (5.54) refers to the termination, where P is the solution to the Ricatti equation of the linear-quadratic problem. RB-MPC is empirically proven to implicitly capture the state derivatives within the neighbourhood of the linearized equilibrium points [91]. It therefore widens the applicability of the linearized model and enhances the transient performance of the control.

The objective to be optimized may comprise the performance indices to be optimized over a finite horizon and constraint violation penalty functions subject to the input and state variable bounds and rate constraints. The objective function of the MPC tuner

is given by (5.55), which minimizes the frequency deviation and the ROCOF over the prediction horizon, while minimizing the control effort.

$$\xi_N^T P \xi_N + \sum_{k=1}^{N_p-1} (e_k^T Q e_k + u_k^T R u_k + M \varepsilon^2) \quad (5.54)$$

$$J = \sum_{i=k+1}^{k+N_p-1} X_i^T Q X_i + U_i^T R U_i \quad (5.55)$$

5.3.3 Cooperative MPC Framework

The parallel cooperative distributed MPC (C-DMPC) architecture, shown in Fig. 5.7a, is based on a centralised cost function. Flexi-DERs indicate that the DERs with flexible resources can contribute to frequency response. The local MPCs simultaneously optimize for the same global objective f_{obj} subject to the system constraints C_{sys} and the operational constraints of the particular DER C_i in an iterative manner. The prime advantage of this cooperative predictive algorithm is that it is strongly based on complexity. The stability of the distributed control can be guaranteed due to the information sharing [162]. Each local MPC would therefore receive the full state measurement, the control trajectories of other MPCs, and is aware of the dynamics of the entire system. The optimization is performed by the individual MPCs assuming that all the other MPCs retain the same input trajectories as the last iteration. With the new optimized input trajectories $U_i(k+1)^*$ of each MPC, a combined final optimal trajectory $U_i(k+1)^{GJ}$ is obtained by the Gauss-Jacobi weighted sum transformation as shown in (5.56) at the end of the c^{th} iteration of predictive optimization for the k^{th} sampling time of the i^{th} local MPC, where α is the weight of each participating DER [162]. The steps followed in the cooperative predictive control is represented as a flowchart in Fig. 5.7b.

$$U_i(k+1)^{GJ} = \alpha_i U_i(k+1)^{c-1} + (1 - \alpha_i) U_i(k+1)^* \quad (5.56)$$

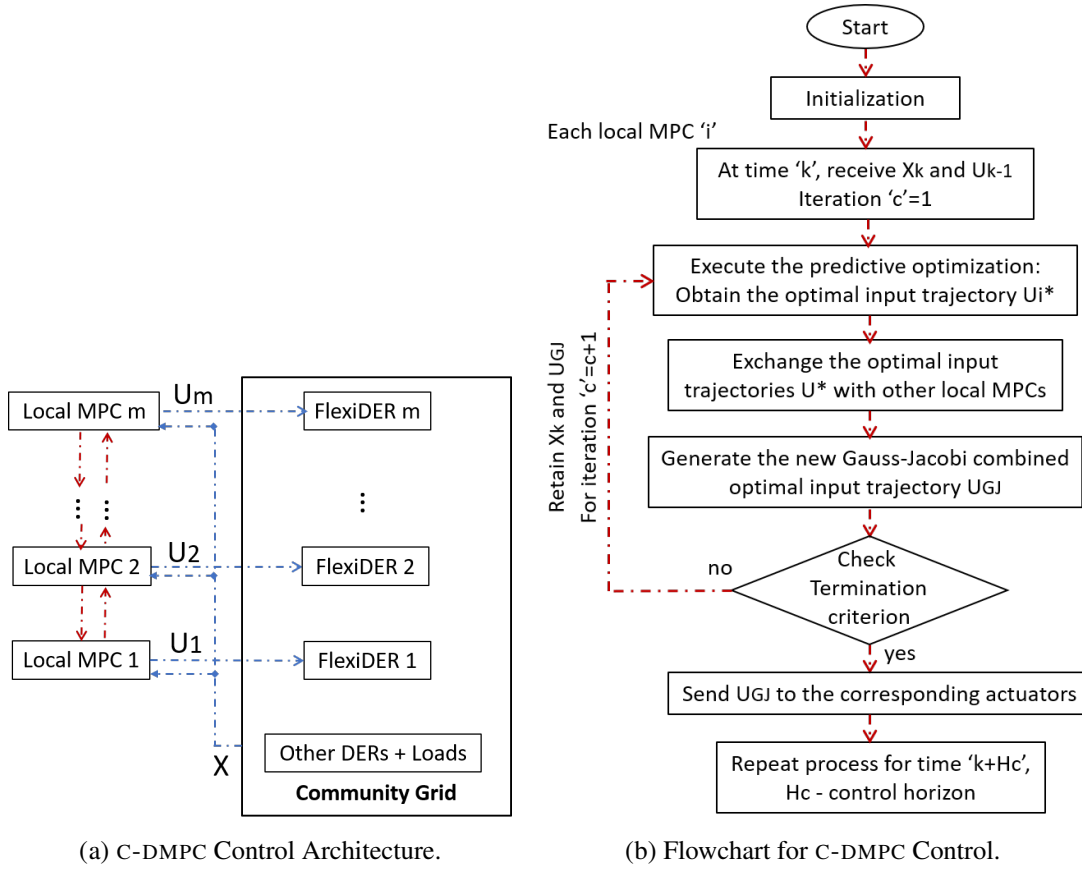


Fig. 5.7: Cooperative MPC Framework.

5.4 Results and Discussion

5.4.1 Isochronous Grid-forming Control

The proposed isochronous control has been validated on a power hardware-in-the-loop setup as described in Section 4.4.2.3. However, as the IBR is voltage-controlled for grid-forming function, the inverter acts as a voltage source, while the rest of the microgrid modelled using the OPAL-RT[®] real-time simulation target and emulated by the power amplifier is current controlled. The experimental setup has been presented in Fig. 5.8.

The isochronous control has been implemented on the CIGRE benchmark microgrid described in Section 4.4.1. Grid-forming IBR 1 with a high power rating and flexibility is controlled by an isochronous controller. IBR 2 is equipped with BESS providing the steady-state response and the fast-acting super-capacitors for compensating the transient

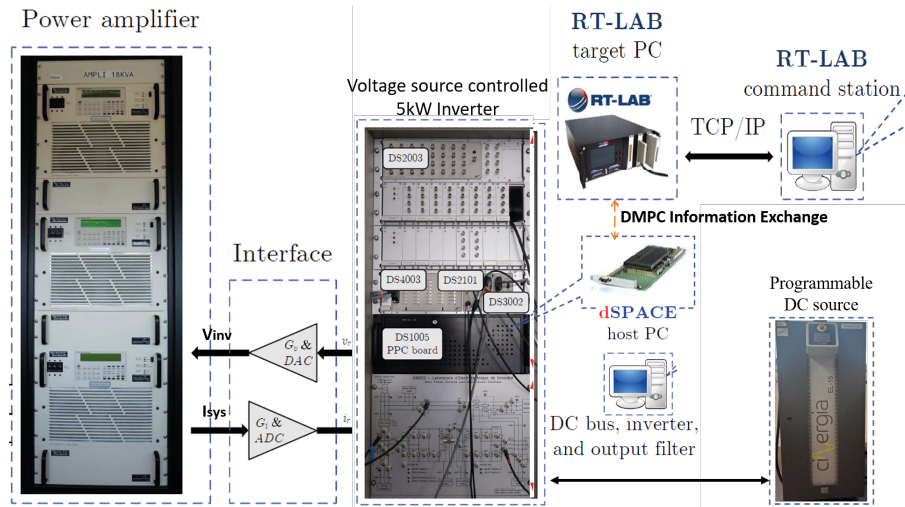


Fig. 5.8: PHIL Experimental Setup

disturbances. Super-capacitors have a higher power rating than the BESSs, and are hence more suited to provide the transient response. The model predictive control thereby exploits the higher power rating of the distributed flexibility resources to provide a robust frequency response. The first set of waveforms in Fig. 5.9 present the inverter output response of the isochronous IBR to a step load change of 20% total system load where the voltage and frequency are regulated without a steady-state error (as compared to the droop control waveforms in Fig. 5.16). The flexibility of the IBR is provided by the HESS on the DC-side of the IBR, the waveforms of which are presented in the second set of signals in Fig. 5.9.

5.4.2 Droop Control in Resistive Microgrids

A 2-inverter single-phase system with a resistive impedance [159] has been used for offline validation in MATLAB/Simulink[®]. The two inverters in the system are considered to be of equal capacity for the clear representation of the results. Inverter unit 2 is operated in the droop control mode to follow the changing load, while the first unit is operated in different modes as shown in Fig. 5.10.

Initially the first unit is operated in the synchronization mode, before it is connected to the microgrid. During this period IBR 2 supplies the total system load. Once connected

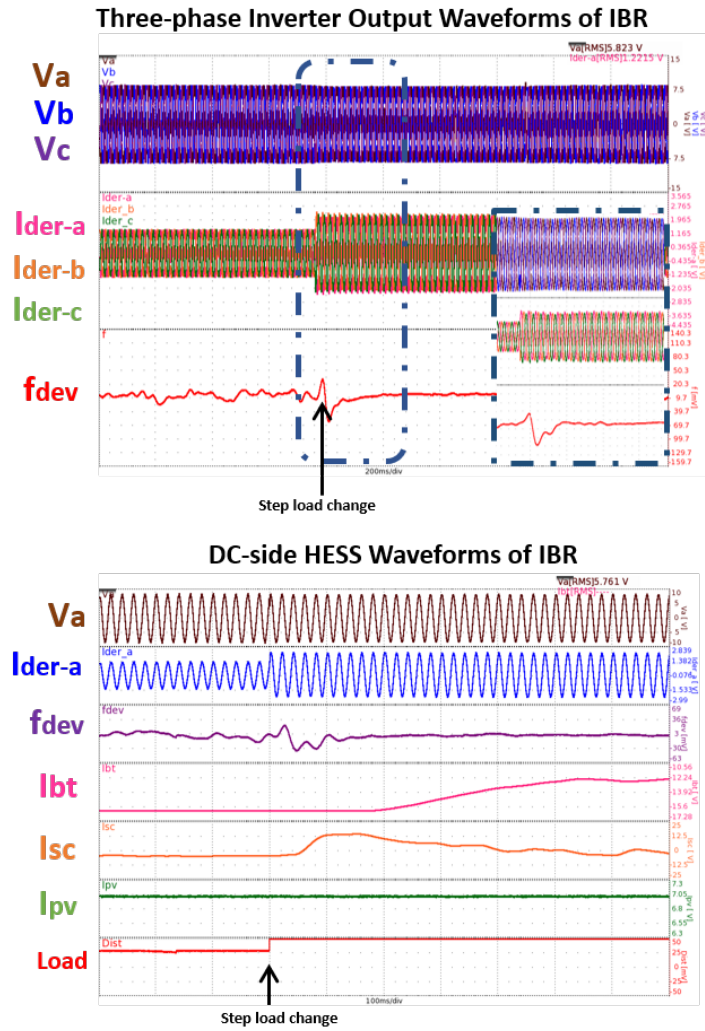


Fig. 5.9: Isochronous Grid-former Response.

to the microgrid, the first unit is operated as a constant power source of 3 kW, during which the other unit supplies the remaining load by following the load change. It is also noteworthy that the change in the P loading affects only the RMS value of the output voltage, while the change in Q affects the system frequency as shown in Fig. 5.10d and Fig. 5.10e respectively.

The first unit is then changed to operate in the droop control mode in which the power is shared proportionally. In order to implement an accurate power sharing the virtual resistance of the inverter R_v is tuned to 0.4Ω based on the parameter selection procedures described in the previous sections. The effect of R_v on the power sharing accuracy and response time are reflected in Fig. 5.11, where it can be observed that a higher R_v

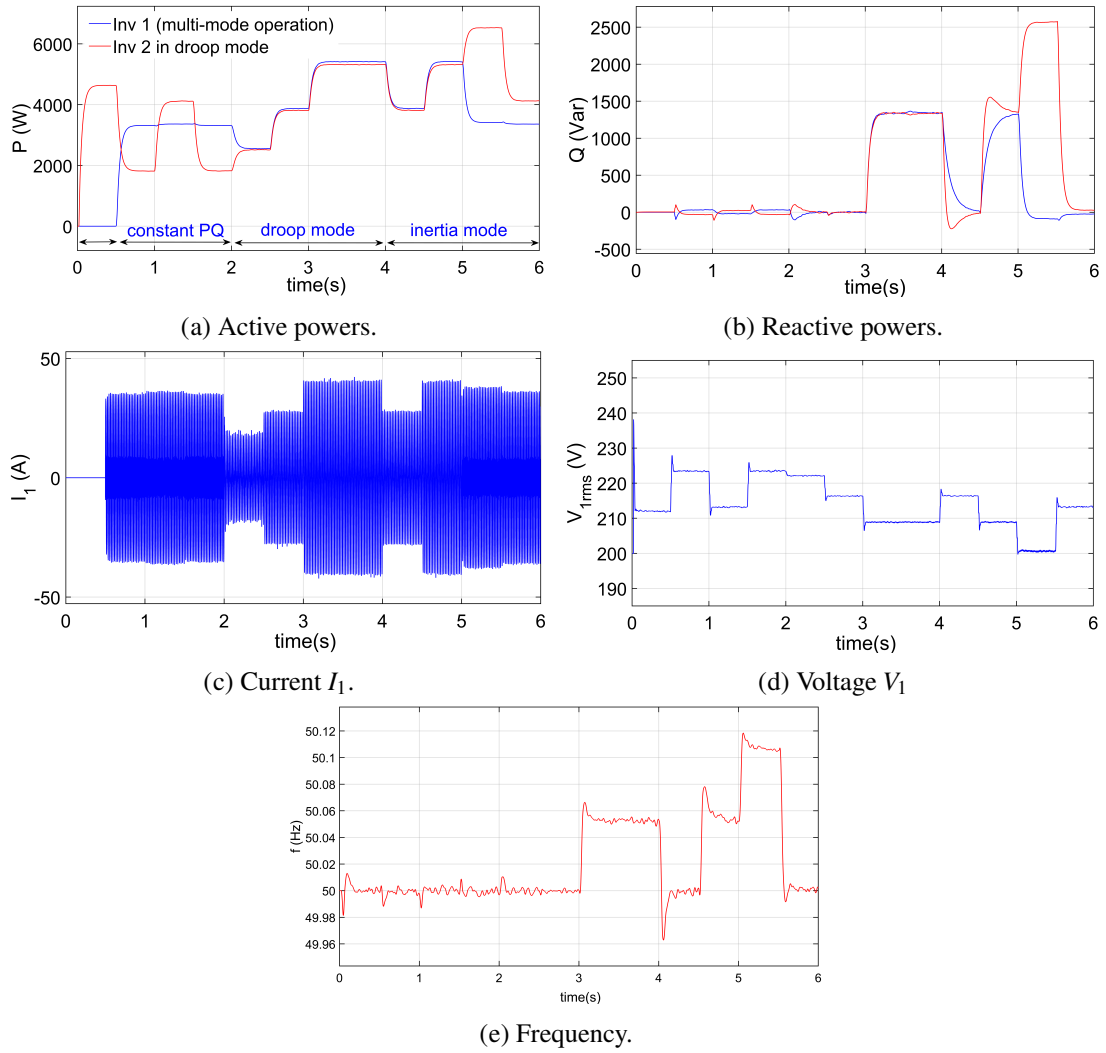


Fig. 5.10: Operation of IBR in Different Modes.

increases the power sharing accuracy, i.e. the power is shared equally by the two units in this case. Since the inverters are rated equally in this system, the power shared by the inverters are equal in the droop mode. The droop coefficients n_p and m_q are set as $1.5e^{-3}$ V/W and $2.5e^{-4}$ Hz/Var respectively. Based on the system dynamics, the optimal active damping terms n_{p1} and m_{q1} are set as $3e^{-4}$ V.s/W and $5e^{-5}$ Hz.s/Var respectively. There is also a significant impact of the virtual impedance on the power sharing accuracy as the total active power load level increases for the $R_v = 0.1\Omega$ case in Fig. 5.11.

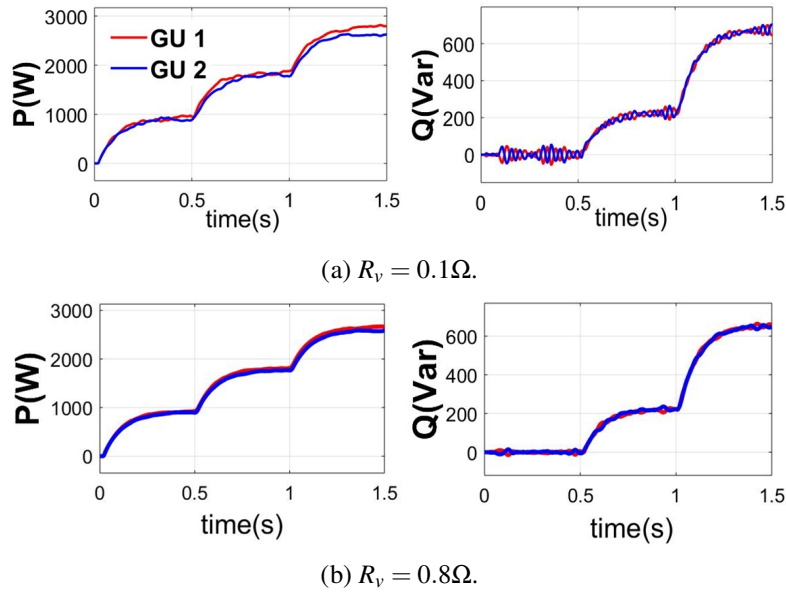


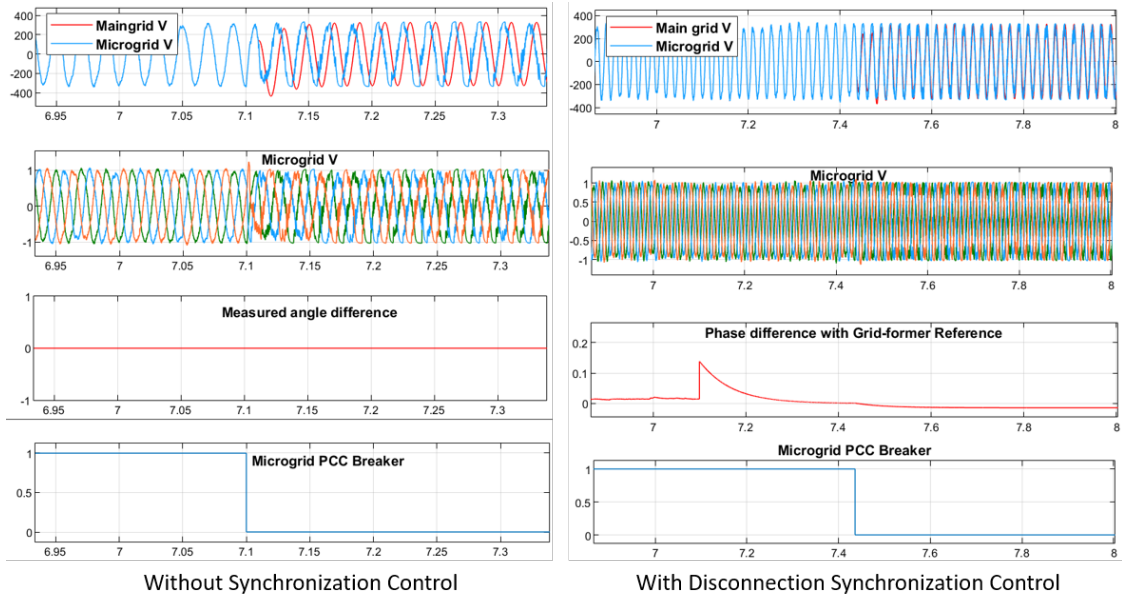
Fig. 5.11: Effect of R_v on Power Sharing Accuracy and Response Time.

5.4.3 Synchronization Control for Microgrid Transition

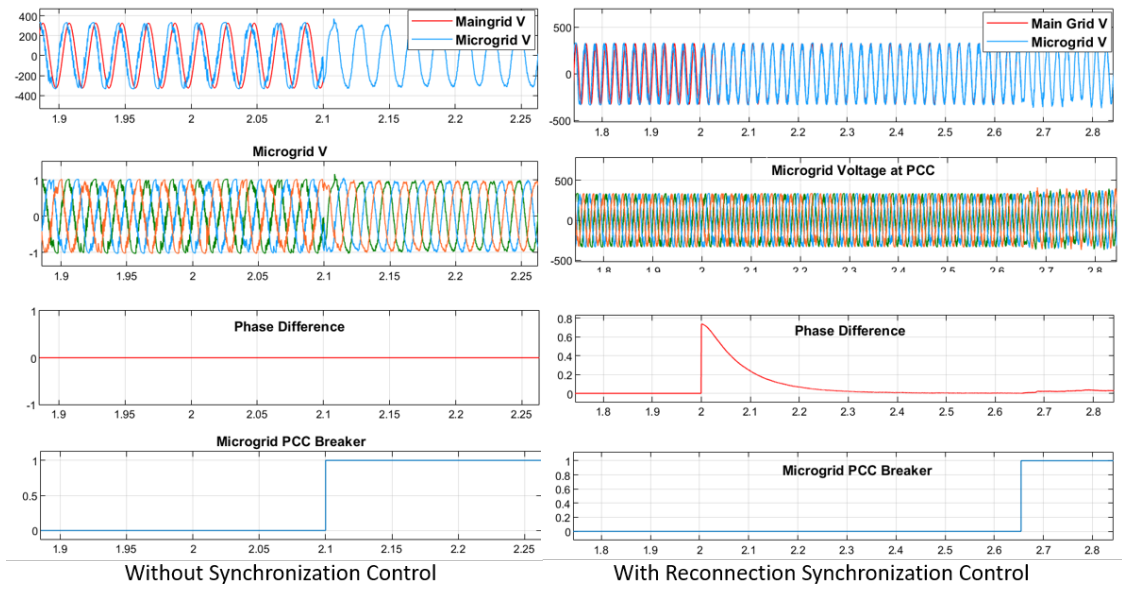
The synchronization control comes into action for a planned disconnection or reconnection of a three-phase microgrid where the angle difference is first regulated to approximately zero to trigger the breaker for the transition. Fig. 5.12 presents the benefit of employing the disconnection and reconnection synchronization controls to smoothen the transient. It can be observed in Fig. 5.12a that for a smooth islanding transition, i.e. if the microgrid is disconnected from the interconnected microgrids or the main grid for autonomous operation, the synchronization sets the initial angle of the grid former by regulating the phase difference between the voltage angle of the main grid and the grid-former setting to zero. Once the angle difference is regulated, the PCC circuit breaker is opened. Similarly, the grid-former angle is controlled to regulate the angle difference to zero for reconnecting to the main grid as shown in the waveforms in Fig. 5.12b.

5.4.4 Cooperative Predictive Droop Control

The droop, damping, and inertia parameters are tuned by the model predictive strategy. Although inertia and droop parameters can be tuned optimally within the time-varying



(a) Disconnection Synchronization.



(b) Reconnection Synchronization.

Fig. 5.12: Synchronization Control for Microgrid Transition.

flexibility of the DERS, the damping ratio and the droop slope constrain each other. Hence, there is a trade off between the system dynamics and the shared balancing power. The effect of damping variation on droop parameter is shown in Fig. 5.13.

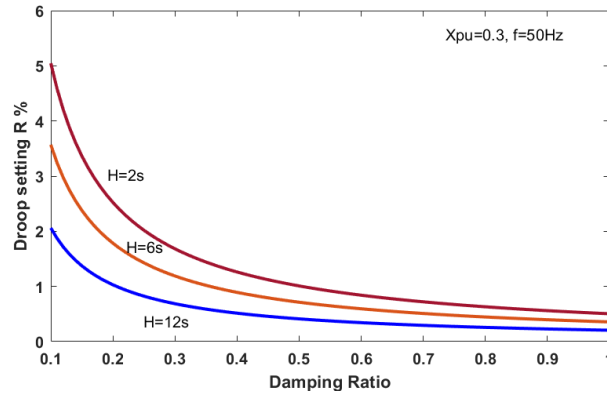


Fig. 5.13: Interdependence of Droop and Damping Parameters.

Time domain simulations of grid-forming control in the DERS of the 3-inverter microgrid discussed in Section 3.4.3 and modelled with DC-side HESS of battery and supercapacitor are presented in Fig. 5.14. Super-capacitors have a higher power rating than the BESSs, and are hence more suited to provide inertia response. The model predictive control thereby exploits the higher power rating of the distributed flexibility resources to provide a robust frequency response.

As the proposed fast-frequency optimal controller is meant for real-time optimization and control, we have used a power hardware-in-the-loop (PHIL) platform to validate the robustness of the real-time control. The PHIL setup shown in Fig. 5.8 comprises a 5kW inverter supplied by a controllable DC voltage source. The inverter is controlled as a grid-forming voltage source and is connected to the power amplifier. The output of the power amplifier is manipulated by the OPAL-RT real time simulation target in which the rest of the microgrid is simulated. The hardware inverter is controlled as a grid-former and another DER is emulated by the power amplifier which is modelled in the real-time target. The inverter control is programmed in the d-Space controller to command the inverter switches.

Fig. 5.15a shows that only the hardware grid-former is controlled by a centralized MPC to perform the fast-frequency control. In each scenario, a load disturbance has been

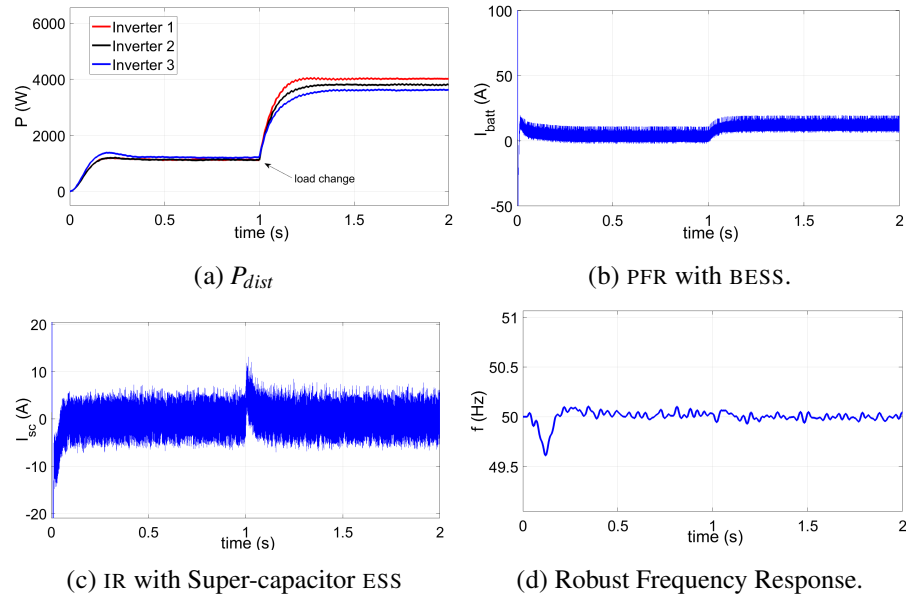


Fig. 5.14: PFR and IR with ESS-based DERs.

emulated to observe the frequency response. Further, the same grid-former serves as the dedicated frequency reserve, while the other DER operates in a fixed power mode, with zero inertia and droop parameters. Fig. 5.15c shows the real-time variation of the DER responses in the event of disturbances in the system. The frequency response is seen to be robust. Finally, in the event of a failure in the grid-former, the other grid-supporting DER provides a frequency response limited to its capacity constraints, which causes a higher frequency deviation.

Fig. 5.16 presents some of the results showcasing the MPC grid-forming control implemented in the DERs 1, 2, and 6 in the CIGRE benchmark microgrid where DER 1 is present as the 5 kW hardware inverter controlled by the dSpace[®] controller, while the rest of the microgrid is emulated by the power amplifier which is controlled by the microgrid model on the real-time target.

The results showcase different scenarios of PV and load disturbances, and the corresponding response of the IBR with the support of HESS. The HESS waveforms of a droop-controlled IBR have been presented in the first set of waveforms in Fig. 5.16, while the second set of waveforms presents the frequency response of the droop controller. It is to be noted that unlike isochronous control, there is a steady-state error due

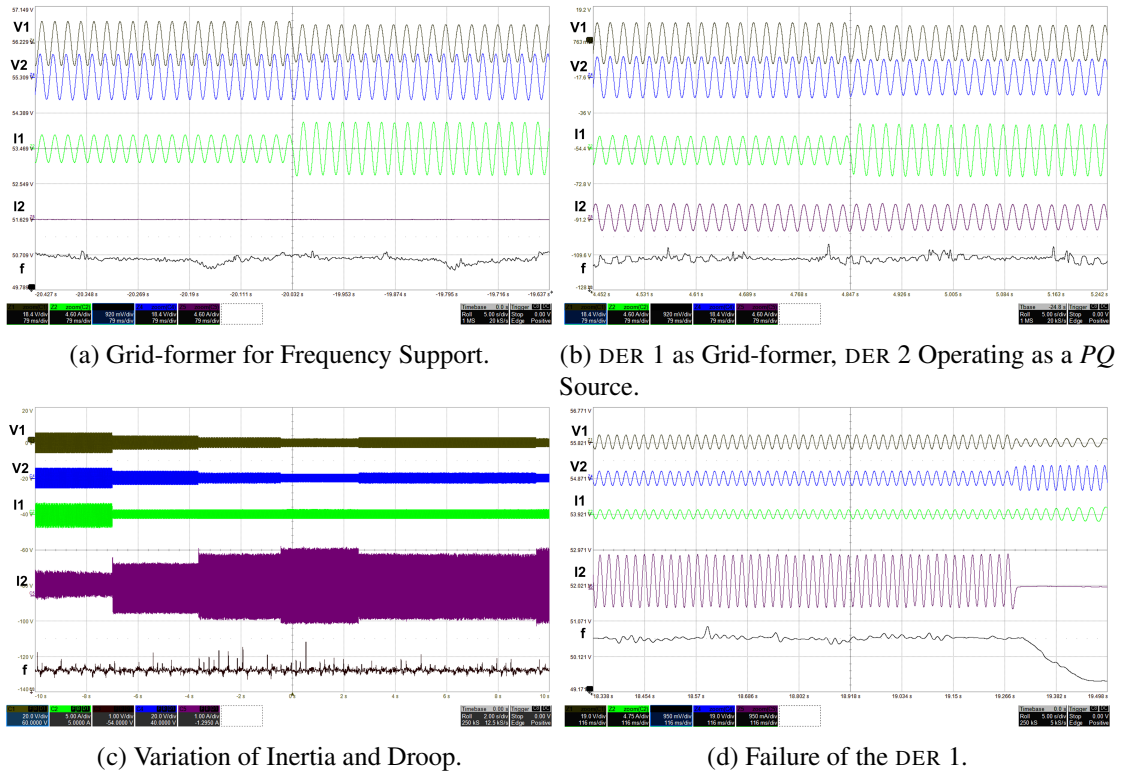


Fig. 5.15: Frequency Response of Parallel DERs

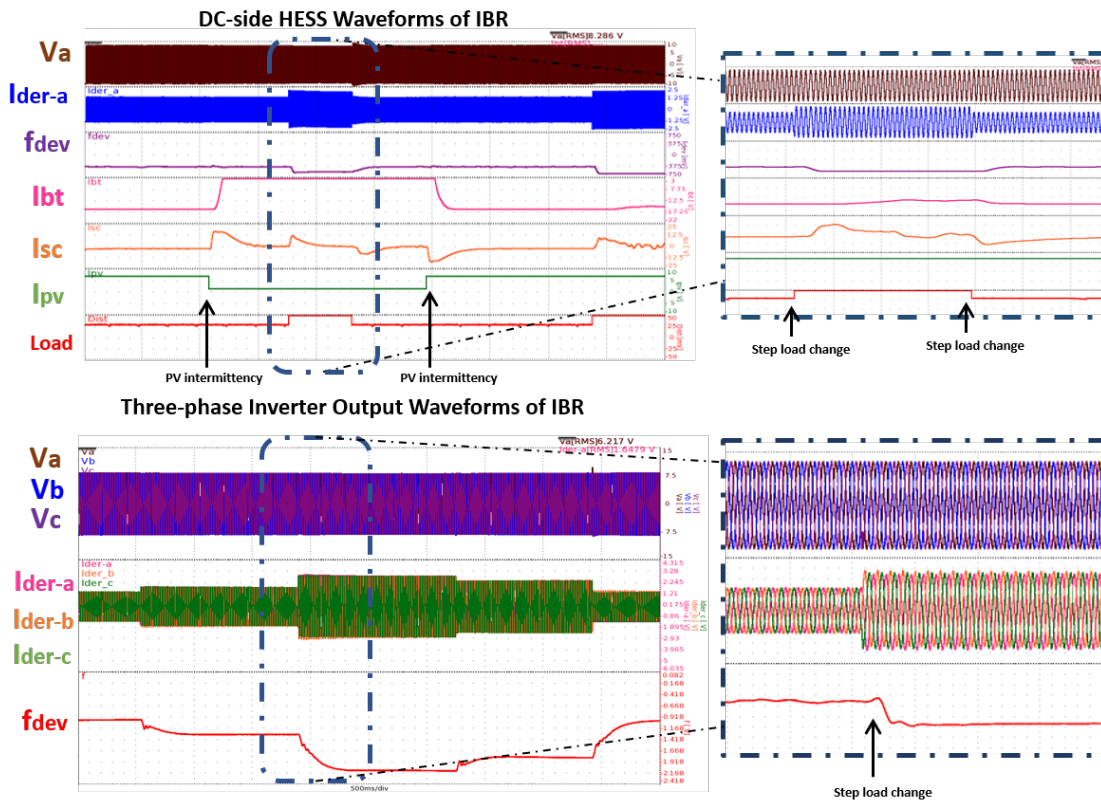


Fig. 5.16: Grid-forming MPC Droop and Inertia Control Response.

to the power-frequency droop that has to be corrected by secondary frequency response. The supercapacitor and battery compensate for the PV intermittency to maintain the inverter output current. On a load change, the reference inverter output current is set in the controller based on the droop settings. The increase or decrease in the inverter reference current setting is in turn actuated by flexibility of the inverter current is in turn due to the additional flexibility provided by the HESS. The frequency response of grid-formers are observed to be faster than the corresponding response of a grid-following DERs with equivalent control parameters. This is due to the control strategy of grid-formers as they do not rely on the frequency measurement to respond to disturbances, and hence the faster response.

5.5 Chapter Summary

The grid-forming control is principal for the autonomous operation of the 100% IBR system. In this chapter, the isochronous and droop-based grid-formers have been discussed with their coordination schemes. Further, the predictive control has been explored to regulate the inertia and damping parameters to improve the frequency response characteristics. The frequency response of grid-forming IBRs is faster than that of the grid-following IBRs discussed in Chapter 4 as they do not rely on the frequency or ROCOF measurement for the FFR. In addition to optimizing the frequency response with enhanced controls, the small signal stability of the system has to be secured. Hence, the interaction of the discussed controllers and its impact on the oscillatory stability of the system will be investigated in the following chapter for the coordinated tuning of frequency control parameters.

Chapter 6

Small Signal Stability of IBR

Microgrids

The control strategies discussed in Chapters 4 and 5 stabilize and optimize the frequency stability of the system, however, the interaction between the IBRs equipped with the different control strategies are prone to impact the oscillatory stability of the system [33, 34]. In order to study the interaction between the different controls, the IBRs are modelled for small signal stability (SSS) analysis using modal analysis in this chapter. As modal analysis requires the steady state operating points, a stochastic backward/forward islanded microgrid power flow analysis has been presented that incorporates the droop control in the power flow algorithm. The small signal model of the microgrid with the grid-forming and grid-following components are described below.

6.1 Small Signal Modelling

For studying the small signal stability of the microgrid, the system inclusive of the IBRs with their controls, filters, lines, and loads are modelled in a linear state space representation. The various IBR controls have been modelled as state space equations in the

respective chapters. In this section, the individual IBR linearized state space models are derived based on the state space equations to formulate the overall system model.

6.1.1 Modelling Inverter based Resources

6.1.1.1 Grid-forming IBRs

The grid forming control in IBRs and their corresponding state space equations have been discussed in Chapter 5. Droop control is a phasor-domain grid-forming control that implements a linear relationship between $P - f$ and $Q - V$. The state space equations may vary depending on the control strategies such as virtual impedance, acting damping control, and inertia emulation. However, the basic droop state space equations are used to formulate the linearized model and can therefore be modified for other grid-forming controllers using the corresponding state space equations from Section 5.2. The inverter is connected to the bus through an LCL filter with components $r_f, L_f, C_f, r_c,$ and L_c . The state space equations of the LCL filter are presented in (6.1)-(6.6).

$$\frac{di_{ld}}{dt} = -\frac{r_f}{L_f}i_{ld} + \omega i_{lq} + \frac{v_{id}}{L_f} - \frac{v_{od}}{L_f} \quad (6.1)$$

$$\frac{di_{lq}}{dt} = -\frac{r_f}{L_f}i_{lq} - \omega i_{ld} + \frac{v_{iq}}{L_f} - \frac{v_{oq}}{L_f} \quad (6.2)$$

$$\frac{dv_{od}}{dt} = \omega v_{oq} + \frac{i_{ld}}{C_f} - \frac{i_{od}}{C_f} \quad (6.3)$$

$$\frac{dv_{oq}}{dt} = -\omega v_{od} + \frac{i_{lq}}{C_f} - \frac{i_{oq}}{C_f} \quad (6.4)$$

$$\frac{di_{od}}{dt} = -\frac{r_c}{L_c}i_{od} + \omega i_{oq} + \frac{v_{od}}{L_c} - \frac{v_{bd}}{L_c} \quad (6.5)$$

$$\frac{di_{oq}}{dt} = -\frac{r_c}{L_c}i_{oq} - \omega i_{od} + \frac{v_{oq}}{L_c} - \frac{v_{bq}}{L_c} \quad (6.6)$$

The state space representation of the inverter has been written with respect to the inverter reference frame. Considering a microgrid with more than one inverter connected in parallel, the state space model has to be represented in the common reference frame. The above equations may be written in the common reference frame using the δ computed

using (6.7) - (6.10). The subscripts d, q represent the individual inverter reference frame and the subscripts D, Q represent the common reference frame, which is the d, q frame corresponding to the first or only grid-forming inverter in the microgrid.

$$\begin{bmatrix} \Delta i_{oDQi} \end{bmatrix} = T_S \begin{bmatrix} i_{odqi} \end{bmatrix} + T_C \begin{bmatrix} \Delta \delta_i \end{bmatrix} \quad (6.7)$$

$$\begin{bmatrix} \Delta v_{bdq} \end{bmatrix} = T_S^{-1} \begin{bmatrix} v_{bDQ} \end{bmatrix} + T_C^{-1} \begin{bmatrix} \Delta \delta_i \end{bmatrix} \quad (6.8)$$

$$T_S = \begin{bmatrix} \cos(\delta) & -\sin(\delta) \\ \sin(\delta) & \cos(\delta) \end{bmatrix} \quad (6.9)$$

$$T_C = \begin{bmatrix} -V_{bD}\sin(\delta) & V_{bQ}\cos(\delta) \\ -V_{bD}\cos(\delta) & -V_{bQ}\cos(\delta) \end{bmatrix} \quad (6.10)$$

The overall state variables of each individual inverter may be listed as shown in (6.13). The additional subscript i in (6.13) represents the state variables of a particular inverter i . The overall state space model of each inverter is given by (6.11)-(6.12), where the matrices $A_{INV}^i, B_{INV}^i, B_{\omega com}^i, C_{INV\omega i}$ and C_{INVci} may be computed using the state space equations.

$$\begin{bmatrix} \Delta x_{inv}^i \end{bmatrix} = A_{inv}^i \begin{bmatrix} \Delta x_{inv}^i \end{bmatrix} + B_{inv}^i \begin{bmatrix} \Delta v_{bDQ}^i \end{bmatrix} + B_{\omega com}^i \begin{bmatrix} \Delta \omega_{com} \end{bmatrix} \quad (6.11)$$

$$\begin{bmatrix} \Delta \omega_i \\ \Delta i_{oDQi} \end{bmatrix} = \begin{bmatrix} C_{INV\omega i} \\ C_{INVci} \end{bmatrix} \begin{bmatrix} \Delta x_{INV}^i \end{bmatrix} \quad (6.12)$$

$$\Delta x_{inv}^i = \begin{bmatrix} \Delta \delta_i & \Delta P_i & \Delta Q_i & \Delta \phi_{di} & \Delta \phi_{qi} & \Delta v_{di} & \Delta v_{qi} & \Delta i_{ldi} & \Delta i_{lqi} & \Delta v_{odi} \\ & & & & & & & & & & \Delta v_{oqi} & \Delta i_{odi} & \Delta i_{oqi} \end{bmatrix} \quad (6.13)$$

6.1.1.2 Grid-following IBRs

Consider the grid-feeding IBR in Fig. 4.1, which is controlled as a current source to feed a reference power P_{ref}, Q_{ref} set by the controller. Based on the power set-points, the reference current $I_{d,q}^*$ is calculated using the reference voltage from the grid-former or the main grid v_d, v_q . The state vector of a typical grid-feeding IBR is given by (6.16),

where ϕ_{dc} is the state of the DC-DC PI control similar to v_{id} and v_{iq} which are the states of the PI current controller, and θ_{pll} is the state affected by the PLL filter. The input vector of the grid-feeding IBR consists of the $d - q$ components of the measured grid-former or main grid voltage as reference v_g , and the reference power inputs P_{ref} and Q_{ref} in (6.14). The outputs are the $d - q$ components of the IBR output current in the $D - Q$ reference i_{oD} in (6.15). The linearized state psace model of the grid-feeding IBR can therefore be computed based on the derived state space equations in Section 4.1 and the current controller equations similar to those of the droop control.

$$U_{Gfeed}^i = [v_{gD} \quad v_{gQ} \quad P_{ref,i} \quad Q_{ref,i}] \quad (6.14)$$

$$Y_{Gfeed}^i = [i_{oDi} \quad i_{oQi}] \quad (6.15)$$

$$\Delta x_{feed}^i = [\Delta\delta_i \quad \Delta V_{dc-i} \quad \Delta\phi_{dc} \quad \Delta\theta_{pll} \quad \Delta v_{di} \quad \Delta v_{qi} \quad \Delta i_{ldi} \quad \Delta i_{lqi} \quad \Delta v_{odi} \quad \Delta v_{oqi} \quad \Delta i_{odi} \quad \Delta i_{oqi}] \quad (6.16)$$

Unlike grid-feeding IBRs, the grid-supporting ones respond to the frequency deviations by altering the power set point as a function of the system frequency. While the rest of the state space equations remain the same, the input vector also has the system frequency ω_g as a control variable. The linearized model can there fore be written as shown in (6.17)-(6.19).

$$U_{Gsup}^i = [v_{gD} \quad v_{gQ} \quad P_{ref,i} \quad Q_{ref,i} \quad \omega_g] \quad (6.17)$$

$$Y_{Gsup}^i = [i_{oDi} \quad i_{oQi}] \quad (6.18)$$

$$\Delta x_{sup}^i = [\Delta\delta_i \quad \Delta V_{dc-i} \quad \Delta\phi_{dc} \quad \Delta\theta_{pll} \quad \Delta v_{di} \quad \Delta v_{qi} \quad \Delta i_{ldi} \quad \Delta i_{lqi} \quad \Delta v_{odi} \quad \Delta v_{oqi} \quad \Delta i_{odi} \quad \Delta i_{oqi}] \quad (6.19)$$

6.1.2 Overall System Model

The autonomous microgrid in Fig. 6.1 which has been discussed in Section 3.4.3 and 5.2 has been considered for the oscillatory stability study, as smaller systems allow a

detailed analysis of eigentraces. It consists of 3 inverters fed from the DC bus by the combination of an intermittent renewable source such as PV or wind, with an ESS mix, and three loads of RL, RC and RL types respectively. The system data may be obtained from [27].

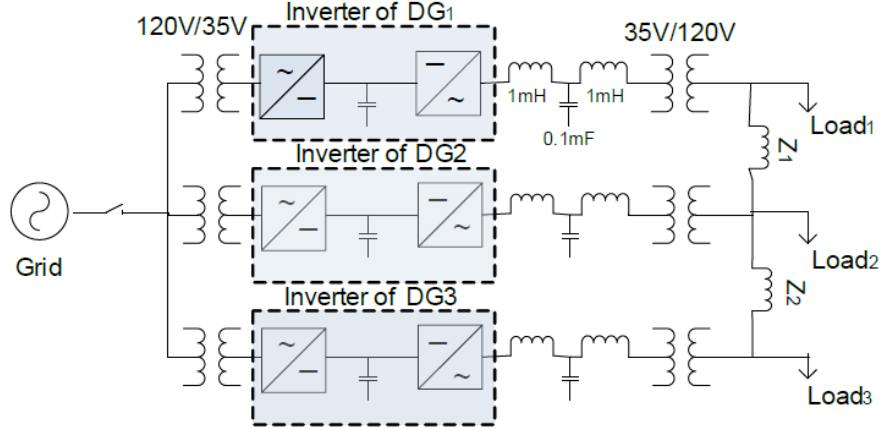


Fig. 6.1: 3-IBR Islanded Microgrid.

6.1.2.1 Network Model

The network lines are modelled as RL branches. The state space equations of the i_{th} line current flowing from node a to b may be written as in (6.20) and (6.21). The state space model of the microgrid network may be represented by (6.22) where, the matrices A_{line} , B_{1line} , and B_{2line} may be computed from (6.20) and (6.21).

$$\frac{di_{lineDi}}{dt} = -\frac{r_{linei}}{L_{linei}}i_{lineDi} + \omega i_{lineQi} + \frac{1}{L_{linei}}(v_{bDa} - v_{bDb}) \quad (6.20)$$

$$\frac{di_{lineQi}}{dt} = -\frac{r_{linei}}{L_{linei}}i_{lineQi} - \omega i_{lineDi} + \frac{1}{L_{linei}}(v_{bQa} - v_{bQb}) \quad (6.21)$$

$$\begin{bmatrix} \Delta i_{lineDQ} \end{bmatrix} = A_{line} \begin{bmatrix} \Delta i_{lineDQ} \end{bmatrix} + B_{1line} \begin{bmatrix} \Delta v_{bDQ} \end{bmatrix} + B_{2line} \Delta \omega \quad (6.22)$$

6.1.2.2 Load Model

Loads 1 and 3 of the microgrid in Fig. 6.1 are modelled as inductive RL loads which are very common in the distribution system. Their load models are given by (6.23) and

(6.24). Load 2 is modelled as a series RC load in (6.25) and (6.26) that represent the effect of capacitor banks at the substation.

$$\frac{di_{loadDi}}{dt} = -\frac{r_{loadi}}{L_{loadi}}i_{loadDi} + \omega i_{loadQi} + \frac{1}{L_{loadi}}v_{bDi} \quad (6.23)$$

$$\frac{di_{loadQi}}{dt} = -\frac{r_{loadi}}{L_{loadi}}i_{loadQi} - \omega i_{loadDi} + \frac{1}{L_{loadi}}v_{bQi} \quad (6.24)$$

$$\frac{dv_{capDi}}{dt} = -\frac{1}{r_{loadi}C_{loadi}}v_{capDi} + \omega v_{capQi} + \frac{1}{r_{loadi}C_{loadi}}v_{bDi} \quad (6.25)$$

$$\frac{dv_{capQi}}{dt} = -\frac{1}{r_{loadi}C_{loadi}}v_{capQi} - \omega v_{capDi} + \frac{1}{r_{loadi}C_{loadi}}v_{bQi} \quad (6.26)$$

The combined state space model of the loads may be written as (6.27), where the matrices may be computed from (6.23)-(6.26). The state variables of the RL and RC loads are their load currents and the load voltages respectively.

$$\begin{aligned} \left[\Delta \dot{x}_{loadDQ} \right] = & A_{load} \left[\Delta x_{loadDQ} \right] + B_{1load} \left[\Delta v_{bDQ} \right] + B_{2load} \Delta \omega \\ & + B_{3load} \left[\Delta i_{oDQ} \right] + B_{4load} \left[\Delta i_{lineDQ} \right] \end{aligned} \quad (6.27)$$

6.1.2.3 Microgrid Model

The microgrid nodal voltage vector Δv_{bDQ} may be defined in terms of the state variables using the diagonal connectivity matrices M_{inv} , M_{load} , M_{line} , and a virtual high impedance diagonal matrix $R_n \approx 1000\Omega$ in (6.28). The diagonal elements of connectivity matrices are filled with ones for the inverter and negative ones for the loads. M_{line} is filled with 1 or -1 depending on whether the line current is entering or leaving a node respectively.

$$\left[\Delta v_{bDQ} \right] = R_n \left(M_{inv} \left[\Delta i_{oDQ} \right] + M_{load} \left[\Delta x_{loadDQ} \right] + M_{line} \left[\Delta i_{lineDQ} \right] \right) \quad (6.28)$$

$$\begin{bmatrix} \Delta \dot{x}_{inv} \\ \Delta i_{lineDQ} \\ \Delta x_{loadDQ} \end{bmatrix} = A_{MG} \begin{bmatrix} \Delta x_{inv} \\ \Delta i_{lineDQ} \\ \Delta x_{loadDQ} \end{bmatrix} \quad (6.29)$$

Combining the inverter, line, and the load state space models, the microgrid can be represented by (6.29) and (6.30) [27]. As the small signal analysis is conducted around

a given operating point, an islanded microgrid power flow methodology has been described in the section below to obtain the steady-state operating point.

$$A_{MG} = \begin{bmatrix} A_{inv} + B_{inv}R_nM_{inv}C_{invc} & B_{inv}R_nM_{line} & B_{inv}R_nM_{load} \\ B_{1line}R_nM_{inv}C_{invc} + B_{2line}C_{inv\omega} & A_{line} + B_{1line}R_nM_{line} & B_{1line}R_nM_{load} \\ B_{1load}R_nM_{inv}C_{invc} + B_{2load}C_{inv\omega} & B_{1load}R_nM_{line} & A_{load} + B_{1load}R_nM_{load} \end{bmatrix} \quad (6.30)$$

6.2 Power Flow for Islanded Microgrids

Islanded microgrids based on converter-based distributed generation systems do not possess a fixed voltage reference node. In Chapter 5 parallel operation of inverters in an isolated system is implemented by emulating the synchronous generator droop control i.e. by modelling the droop relations between the $P - f$ and $Q - V$ relations. This results in the addition of a frequency as a new state variable to the power flow problem. Power flow analysis tools are employed to obtain the steady state variables of a power system, which includes the system voltages and frequency in the case of an islanded microgrid.

6.2.1 Deterministic Power Flow Analysis of Islanded Microgrids

In this work, we apply a backward/forward sweep (BFS) algorithm based on the direct approach described in [126] to solve the islanded microgrid power flow. The method described in the sub-section below involves the formation of two simple matrices based on the system topology: the nodal injection-nodal current matrix **bibc** and the nodal current-nodal voltage matrix **bcbv**, that eliminate the time-consuming decomposition and the backward/forward substitution of the nodal admittance matrix in the power flow algorithm.

6.2.1.1 Modified BFS with Droop Equations for Radial Microgrids

For a microgrid operating in the grid-connected mode, the BFS power flow does not pose any problem as there is a stiff node that acts as a voltage reference. However, in the islanded mode, both active and reactive powers are shared by the generators according to their respective droop function, which allows variation of the node voltages and the system frequency. The state variable vector includes the nodal voltage magnitudes, voltage angles, and the system frequency. They are to be computed by the power flow algorithm as described below.

Step 1: The entries of the nodal voltage vector \mathbf{V} are assumed to be 1 per unit and the frequency deviation from the nominal value Δf is assumed to be zero at the start. Steps 3 to 10 form the inner frequency droop control loop, while the voltage of the reference node is adjusted according to the reactive power imbalance in the outer voltage droop control in step 2.

Step 2: The change in the DER reactive power is computed by the $Q - V$ droop equation given by (6.31).

Step 3: The change in the DER active power is computed by the $P - f$ droop equation given by (6.32). Based on the changes in the active and reactive power calculated, the complex power injected at each node is calculated by (6.33), where P_{gi}^0 and Q_{gi}^0 are the rated active and reactive power of the DERs at the rated frequency f^0 and rated voltage V_i^0 respectively.

Step 4: The node current vector \mathbf{I} may be calculated using (6.34), where S_i is the complex power injected into the i^{th} node.

Step 5: The branch current vector \mathbf{I}_{branch} may be computed with the help of **bibc** as shown in (6.35). **bibc** may be formed offline, as it remains the same for a specific system topology. The steps for the formation of **bibc** are given below:

1. Create a matrix of zeroes of size $M * N$, where M is the number of branches and N is the number of nodes in the microgrid.

2. If the k^{th} line is located between the i^{th} node and the j^{th} node, copy the i^{th} column to the j^{th} column of the matrix and fill the element $\mathbf{bibe}(k, j)$ with 1.
3. Repeat the previous step for each of the lines in the radial microgrid.

Step 6: The reference node or node 1 with the largest or only grid-forming unit is the gateway for the excess or deficit power transfer. Thus the power traded at the first node is indicative of the system frequency [125]. The change in the system frequency according to (6.36).

Step 7: The system frequency is modified according to the change in the frequency calculated in the previous step as in (6.37). Equation (6.38) modifies the line impedance vector according to the new frequency, where X_{ij} is the line reactance at the rated frequency.

Step 8: Compute \mathbf{bcbv} and $[\Delta V]$ given by (6.39) and (6.40) respectively, where \mathbf{Z}_{branch} is the branch impedance vector that changes with the system frequency.

Step 9: Compute the updated nodal voltage of each node except node 1, based on (6.41).

Step 10: Repeat steps 3 to 9 until the node voltages converge to a steady value. In this work, the tolerance criteria given by (6.42) is checked between the last two successive iterations of nodal voltage values. k indicates the current iteration number of the inner loop.

Step 11: The outer loop voltage droop control equations are modelled in (6.43) and (6.44), where the voltage of the first node is altered based on the reactive power trading of the node.

Step 12: If the voltage of the first node has not converged to a steady value, repeat from step 2. The convergence of the first node voltage can be checked by the tolerance criteria given in (6.45) where p indicates the current iteration number of the outer loop.

$$\Delta Q_{g_i} = \frac{|V_i| - 1}{n_{Q_i}}, \quad \forall i \in \text{Gen}. \quad (6.31)$$

$$\Delta P_{g_i} = \frac{\Delta f}{m_{P_i}}, \quad \forall i \in \text{Gen}. \quad (6.32)$$

$$S_i = P_{l_i} + P_{g_i}^0 + \Delta P_{g_i} + j * (Q_{l_i} + Q_{g_i}^0 + \Delta Q_{g_i}) \quad (6.33)$$

$$I_i^k = \left(\frac{S_i}{V_i^k} \right)^* \quad (6.34)$$

$$\mathbf{I}_{branch} = \mathbf{babc} * \mathbf{I} \quad (6.35)$$

$$\Delta = -m_{P_1} \left[P_{L_1} + P_{G_1}^0 + \text{Re} \left(\sum_{i \in A_1} V_1 I_{1i}^* \right) \right] \quad (6.36)$$

$$f = f^0 + \Delta f \quad (6.37)$$

$$Z_{ij} = R_{ij} + jX_{ij} \frac{f}{f^0} \quad (6.38)$$

$$\mathbf{bcbv} = \mathbf{babc} * \text{diag}(\mathbf{Z}_{branch}) \quad (6.39)$$

$$\Delta \mathbf{V} = \mathbf{bcbv} * \mathbf{I}_{branch} \quad (6.40)$$

$$V_i = V^0 - \Delta V_i \quad (6.41)$$

$$\min (V_i^k - V_i^{k-1}) < \varepsilon, \quad \forall i = 2, \dots, N \quad (6.42)$$

$$\Delta V^0 = -m_{Q_1} \left[Q_{L_1} + Q_{G_1}^0 + \text{Im} \left(\sum_{i \in A_1} V_1 I_{1i}^* \right) \right] \quad (6.43)$$

$$\mathbf{V}^0 = \left[1 \quad \dots \quad 1 \right]_{1*N}^T - \left[\Delta V_0 \quad \dots \quad \Delta V_0 \right]_{1*N}^T \quad (6.44)$$

$$\min (V_1^p - V_1^{p-1}) < \varepsilon \quad (6.45)$$

6.2.1.2 Modification for Weakly-meshed Topologies

The matrices \mathbf{babc} and \mathbf{bcbv} that were described in the last section will have to be modified for weakly-meshed systems. High density load areas in the distribution system are often the nodes that are involved in the meshed topologies [126]. Normally open tie-switches may be closed on high-loading periods of these nodes. The presence of meshes do not affect the nodal current vector but increases the size of the branch current vector. The tie branches that convert the system from a radial to the weakly meshed system are identified separately.

The **bibc** matrix formation steps are described in step 5 of the BFS algorithm in the previous section. Once the radial system branches are added, the tie branches may be added to the **bibc** matrix. If the k^{th} branch is a tie branch between the i^{th} node and the j^{th} node, fill in the elements of the k^{th} column by subtracting the elements of the j^{th} from the i^{th} column. Also, fill the element **bibc**(k,k) with 1 [126].

The **bcbv** matrix may be obtained by the modified **bibc** matrix and the new line impedance vector appended with the tie line impedances as shown in (6.39). For obtaining the change in the nodal voltages, (6.40) may be replaced by (6.46), where the **bibv** matrix is given by (6.47) and (6.48). Except for the changes in the matrix formations and (6.40), all other steps in the algorithm are valid for weakly-meshed microgrids.

$$\Delta \mathbf{V} = \mathbf{bibv} * \mathbf{I} \quad (6.46)$$

$$\mathbf{bibv} = \mathbf{L} - \mathbf{M}^T \mathbf{N}^{-1} \mathbf{M} \quad (6.47)$$

$$\begin{bmatrix} \mathbf{L} & \mathbf{M}^T \\ \mathbf{M} & \mathbf{N} \end{bmatrix} = \mathbf{bcbv} * \mathbf{bibc} \quad (6.48)$$

6.2.2 Stochastic Response Surface Formulation

This section describes the transformation of the deterministic power flow analysis to the stochastic domain. The principle used in this method is to formulate a polynomial surface representing the function of variation of each state variable in terms of the stochastic input variables of the system [128]. Once the stochastic polynomial response surface (SRS) is formulated for each response variable, it simply replaces the deterministic BFS by the computation of a set of polynomials. The formulation of SRS that represents the BFS is described in this section.

The stochastic input variables include the active power generation of the DERs, active power, and reactive power demands of the load. The photovoltaic generation is influenced by the variation of the sunlight intensity which is often described by the Beta distribution. From (6.49), we can infer that if the solar irradiation is modelled by a Beta

distribution [129], the active power output of the PV system is also given by a beta distribution, where r is the solar irradiation; A_{bt} is the area of the battery; and η is the battery efficiency. The probability density function (PDF) of the Beta distribution is given by (6.50). The beta parameters (a, b) and the maximum irradiation r_{max} are given by the solar irradiation forecasts. Then the active power output of the i^{th} DER, P_{g_i} , is given in (6.50) by replacing r and r_{max} with P and P_{max} respectively. The load demand uncertainties are usually modelled by the normal distribution function [129], with the means μ_p and μ_q and standard deviations σ_2^p and σ_2^q from the load forecasts. The PDF of the Normal distribution function is given by (6.51).

$$P = rA_{bt}\eta \quad (6.49)$$

$$f(r) = \frac{\Gamma(\alpha + \beta)}{\Gamma(\alpha)\Gamma(\beta)} \left(\frac{r}{r_{max}}\right)^{\alpha-1} \left(1 - \frac{r}{r_{max}}\right)^{\beta-1} \quad (6.50)$$

$$f(P_l) = \frac{1}{\sqrt{2\pi}\sigma_p} e^{-\frac{(P_l - \mu_p)^2}{2\sigma_p^2}} ; f(Q_l) = \frac{1}{\sqrt{2\pi}\sigma_q} e^{-\frac{(Q_l - \mu_q)^2}{2\sigma_q^2}} \quad (6.51)$$

Consider the problem of formulation of a SRS for each output response variable y . The polynomial chaos function of the output response variable in terms of the stochastic input vector X may be written as shown in (6.52), where the X denotes the vector of stochastic input variables as given in (6.53); n denotes the number of stochastic input variables; the coefficients a_{j_i} denote the unknown coefficients of the polynomial that have to be computed; and the H_m function denotes the hermite polynomial expansion of m^{th} order. Hermite polynomials are specifically used to represent the polynomial expansion when each of the stochastic variable follows a standard normal distribution. The hermite polynomial function is defined by (6.54). The higher the order of the Hermite polynomial expansion, the higher is the accuracy of the stochastic model. In this work, a Hermite polynomial expansion of the second order has been considered. Accordingly, (6.52) can be reduced to (6.55). The total number of unknown coefficients to be computed for a polynomial chaos expansion of the m^{th} order with n stochastic input variables is given by (6.56).

$$y = a_0 + \sum_{j_1=1}^n a_{j_1} H_1(x_1) + \sum_{j_1=1}^n \sum_{j_2=1}^{j_1} a_{j_1 j_2} H_2(x_1, x_2) + \dots \quad (6.52)$$

$$\mathbf{X} = [x_1, x_2, \dots, x_n]^T \quad (6.53)$$

$$H_m(x_1, x_2, \dots, x_n) = (-1)^m e^{\frac{1}{2}\mathbf{X}^T \mathbf{X}} \frac{\partial^m}{\partial x_1 \dots \partial x_n} e^{-\frac{1}{2}\mathbf{X}^T \mathbf{X}} \quad (6.54)$$

$$y = a_0 + \sum_{j_1=1}^n a_{j_1} x_{j_1} + \sum_{j_1=1}^n a_{j_1 j_1} (x_{j_1}^2 - 1) + \sum_{j_1=1}^n \sum_{j_2=j_1+1}^n a_{j_1 j_2} x_{j_1} x_{j_2} \quad (6.55)$$

$$n_a = \frac{(n+m)!}{n!m!} \quad (6.56)$$

It is to be noted that each of the desired output response variable is modelled by a different polynomial. If \mathbf{Y} represents the vector of the desired response variables, then it may be represented by (6.57), where r is the number of output responses that require the formulation of polynomial approximation models. \mathbf{Y} may include the state variables such as the node voltage magnitudes, node voltage angles, or other dependent variables like the line flows, total active power loss, etc. Thus, the unknown coefficient matrix for \mathbf{Y} may be represented by \mathbf{A} defined in (6.58). In order to compute the n_a unknown coefficients for each response y , n_a linearly independent equations are required. They can be generated as in (6.59), where the \mathbf{H} is the stochastic input hermite matrix defined in (6.60) and \mathbf{Y}_r is the overall response matrix that can be filled with all the r response values obtained from each of the n_a runs of the deterministic power flow with n_a sets of samples of the stochastic input variables. The \mathbf{Y}_r matrix may be formulated as shown in (6.61).

$$\mathbf{Y} = [y_1, y_2, \dots, y_r]^T \quad (6.57)$$

$$\mathbf{A} = \begin{bmatrix} a_0^1 & \dots & a_0^r \\ [a_1^1, a_2^1, \dots, a_n^1]^T & \dots & [a_1^r, a_2^r, \dots, a_n^r]^T \\ [a_{11}^1, a_{22}^1, \dots, a_{nn}^1]^T & \dots & [a_{11}^r, a_{22}^r, \dots, a_{nn}^r]^T \\ [a_{12}^1, a_{13}^1, \dots, a_{1n}^1]^T & \dots & [a_{12}^r, a_{13}^r, \dots, a_{1n}^r]^T \\ [a_{23}^1, \dots, a_{2n}^1]^T & \dots & [a_{23}^r, \dots, a_{2n}^r]^T \\ \dots & \dots & \dots \\ [a_{(n-1)(n)}^1]^T & \dots & [a_{(n-1)(n)}^r]^T \end{bmatrix} \quad (6.58)$$

$$\mathbf{Y}_r = \mathbf{H} * \mathbf{A} \quad (6.59)$$

$$\mathbf{H} = \begin{bmatrix} 1, x_{11} \dots x_{1n}, (x_{11}^2 - 1) \dots, (x_{11}x_{12}) \dots (x_{1(n-1)}x_{1n}) \\ 1, x_{21} \dots x_{2n}, (x_{21}^2 - 1) \dots, (x_{21}x_{22}) \dots (x_{2(n-1)}x_{2n}) \\ \dots \\ \dots \\ 1, x_{r1} \dots x_{rn}, (x_{r1}^2 - 1) \dots, (x_{r1}x_{r2}) \dots (x_{r(n-1)}x_{rn}) \end{bmatrix} \quad (6.60)$$

$$\mathbf{Y}_r = [Y_1 Y_2 \dots Y_{na}] \quad (6.61)$$

$$SV_i = F_i^{-1} \left(\frac{1}{\sqrt{2\pi}} \int_{-\infty}^{x_i} e^{-\frac{t^2}{2}} dt \right) \quad (6.62)$$

The n_a different sets of the stochastic input samples are known as the collocation points (CPs) and are used for the response surface formulation. It is to be noted that the n_a linearly independent sets of stochastic input samples are required to solve the unknown coefficients. The CPs will have to be chosen carefully to ensure the correctness of the polynomial model. In this work, we utilize the efficient CP selection method for the standard normal distribution proposed in [163]. The CPs are the most influencing sample points of the standard normal distribution that affect the stochastic variation of the output response and are chosen according to the rules listed below.

1. The sample points close to the origin are the most preferred as it is the region of highest probability for the standard normal distribution.

2. The sample points picked must be symmetric with respect to the origin to examine the response surface variation with different directions [163].
3. Few random samples may be chosen to improve the model robustness.
4. Samples from the region of very low probability are generally avoided or restricted to one or two CPs [163].

The CPs chosen for the deterministic runs are in the standard normal distribution, whereas the stochastic inputs in the BFS power flow problem follow the beta and normal distribution. Thus, the collocation points chosen according to [163] are converted to their respective distributions by the transformation equation (6.62), where $F(x)$ is the probability density function of the beta or normal distribution for the DER power outputs and the load powers respectively. With the values of the stochastic variable samples SV_i , the BFS deterministic power flow described in the previous section is run n_a times with the different set of sample inputs. \mathbf{Y}_r is filled with the values of the output variables after the deterministic runs and the unknown coefficients are obtained by solving (6.59). Thus, the approximate polynomial stochastic response surface has been formulated and so, the deterministic runs of the power flow may be replaced by the computation of the set of polynomials.

6.2.2.1 Probability Density Estimation

Once the set of polynomial equivalents for the power flow is obtained, similar to the ideal Monte Carlo simulation (MCS), the response variables for a large number of random samples may be computed using the polynomial in a very less computation time. Thus, the response surface reduces the computation time, while maintaining the accuracy of the MCS. With the response variable outputs for a large number of samples, the statistical parameters such as the mean, variance, skewness, and kurtosis may be determined for each response variable using (6.63), (6.64), (6.65), and (6.66) respectively. The probability density functions (PDFs) and cumulative density functions (CDFs) of the response variable distributions may be obtained using the kernel density estimation

tool in MATLAB from the obtained sample responses. The overall flowchart of the steps involved in the stochastic power flow tool is presented in Fig. 6.2.

$$\mu(y_i) = \frac{1}{r} \sum_{j=1}^{n_{sample}} y_{ij} \quad (6.63)$$

$$\sigma^2(y_i) = \frac{1}{r} \sum_{j=1}^{n_{sample}} (y_{ij} - \mu(y_{ij}))^2 \quad (6.64)$$

$$\gamma_1(y_i) = \frac{1}{r\sigma^3(y_i)} \sum_{j=1}^{n_{sample}} (y_{ij} - \mu(y_{ij}))^3 \quad (6.65)$$

$$\gamma_2(y_i) = \frac{1}{r\sigma^4(y_i)} \sum_{j=1}^{n_{sample}} (y_{ij} - \mu(y_{ij}))^4 \quad (6.66)$$

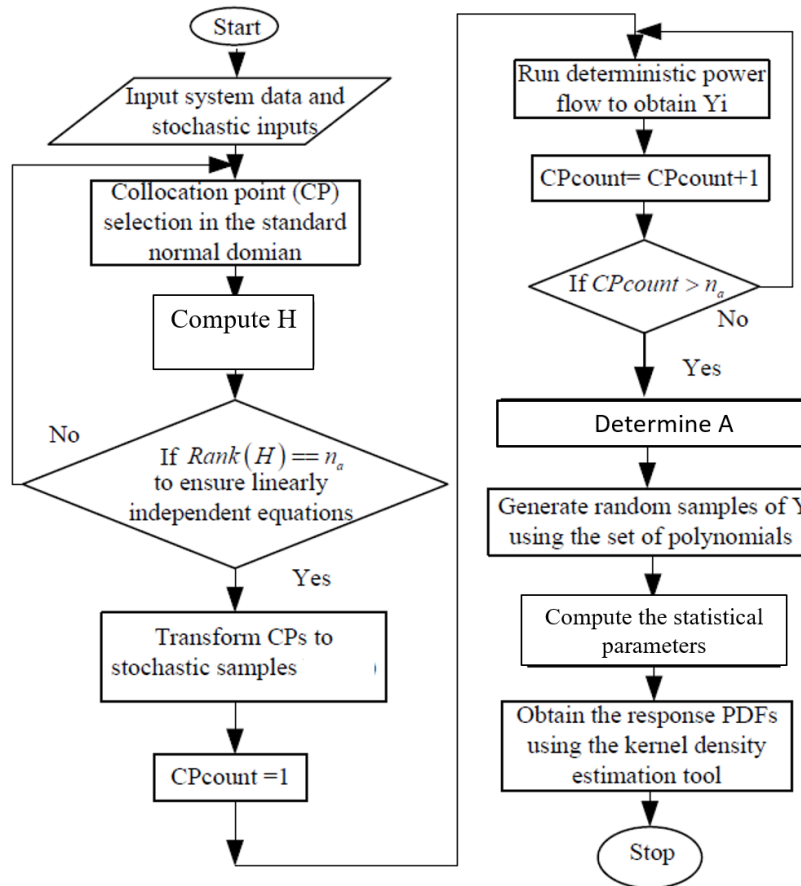


Fig. 6.2: Steps for Stochastic Power Flow.

6.2.3 Illustration with Benchmark System

The steady-state operating point with the droop parameters set for the base case of the 3-IBR microgrid shown in Fig. 6.1 is given by Table 6.1.

Table 6.1: 3-IBR Microgrid Initial Steady State Values.

State	Value	State	Value
f_0	50	δ_0	[0, 1.7e-3, -1.2e-2]
v_{bd}	[379.5, 380.5, 379]	v_{bq}	[-6, -6, -5]
v_{od}	[380.5, 381.9, 380.2]	v_{oq}	[0, 0, 0]
i_{od}	[11.38, 11.38, 11.38]	i_{oq}	[0.5 -1.5 1.25]
i_{ld}	[11.38, 11.38, 11.38]	i_{lq}	[-5.6 -7.25 -4.6]
$i_{line1d,q}$	[-3.77, 0.4]	$i_{line2d,q}$	[7.6, -1.3]

The IEEE 33-bus distribution system has been widely used for power flow studies in the literature and is therefore considered for the validation of the proposed power flow method for larger microgrids. It is an islanded microgrid with five DERs at nodes 1, 6, 13, 25, and 33 and droop coefficients -0.05, -1, -0.1, -1, and -0.2 p.u. respectively. The nominal active and reactive power generated by the DERs are considered to be 0.9 and 0.6 p.u. [125]. The system data along with the DG data may be obtained from [125]. Considering the DER active power outputs to be stochastic variables that follow beta distribution with parameters α and β as 2.06 and 2.5 respectively based on the fitting algorithm using aggregated PV output from [132]; and the load active and reactive powers to follow normal distribution with mean values same as those of the original data and a standard deviation of 5% [132], the SRS algorithm has been used to obtain the probability distribution of the state and dependent variables of the microgrid. The accuracy and computation time comparison between the MCS and the proposed method are presented in Table 6.2.

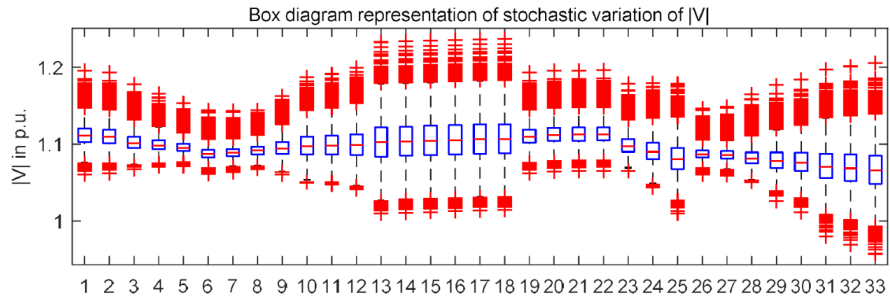
Table 6.2: Comparison of the Performance of SRS Method and MCS.

Ideal accuracy - MCS $n_{sample} = 20000$		
Method	Maximum error in %	CPU time (s)
SRSM $n_{sample} = 10000$	0.23	1.5543
SRSM $n_{sample} = 20000$	0.09	4.1527
MCS $n_{sample} = 10000$	0.15	95.1728

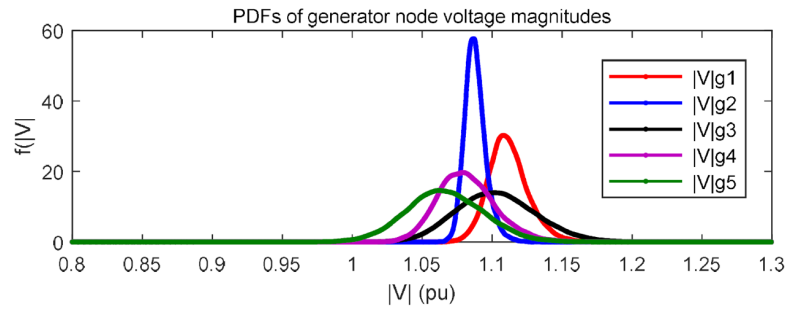
Table 6.3: 33-bus Microgrid - Droop-based BFS Power Flow Solution.

Node	Radial System		Weakly-Meshed System	
	$ V $ in p.u.	δ in deg	$ V $ in p.u.	δ in deg
1	0.9964	0.0000	0.9980	0.0000
2	0.9972	0.0047	0.9989	0.0053
3	1.0000	0.0270	1.0018	0.0175
4	1.0009	0.0137	1.0028	0.0308
5	1.0013	0.0024	1.0035	0.0472
6	1.0022	-0.0150	1.0051	0.0900
7	1.0026	0.0331	1.0050	0.1431
8	1.0026	0.0522	1.0046	0.1478
9	1.0008	0.0679	1.0021	0.1293
10	0.9984	0.0761	0.9996	0.0490
11	0.9980	0.0838	0.9992	0.0430
12	0.9970	0.1006	0.9983	0.0334
13	0.9914	0.0790	0.9919	-0.0414
14	0.9935	0.1465	0.9935	0.0007
15	0.9948	0.1786	0.9945	0.0063
16	0.9960	0.1984	0.9951	0.0324
17	0.9979	0.2634	0.9957	0.1351
18	0.9985	0.2714	0.9957	0.1507
19	0.9978	0.0155	0.9994	0.0217
20	1.0013	0.0819	1.0029	0.1385
21	1.0020	0.1009	1.0036	0.1731
22	1.0026	0.1208	1.0042	0.2431
23	1.0013	0.0752	1.0027	0.0220
24	1.0030	0.1789	1.0037	0.0372
25	1.0016	0.2405	1.0015	0.0108
26	1.0029	-0.0420	1.0060	0.0812
27	1.0037	-0.0804	1.0071	0.0684
28	1.0074	-0.2041	1.0127	0.0340
29	1.0097	-0.3070	1.0166	-0.0011
30	1.0102	-0.3761	1.0175	-0.0718
31	1.0075	-0.3759	1.0157	-0.0921
32	1.0061	-0.3917	1.0147	-0.1160
33	1.0036	-0.4542	1.0125	-0.1910
	P_g in p.u.	Q_g in p.u.	P_g in p.u.	Q_g in p.u.
1	2.4641	0.9728	2.4701	0.9402
6	0.9782	0.8978	0.9785	0.8949
13	1.6821	0.9858	1.6851	0.9813
25	0.9782	0.8984	0.9785	0.8985
33	1.2910	0.8820	1.2925	0.8373
	P_{loss} in p.u.	Q_{loss} in p.u.	P_{loss} in p.u.	Q_{loss} in p.u.
	0.0364	0.0368	0.0253	0.0468

The comparison verifies that the SRS method lessens the computational burden of conventional stochastic computation while maintaining the accuracy of the MCS. The base power flow solution obtained using the droop-based BFS power flow is presented in Table 6.3 under the radial system column. In order to validate the modified algorithm for weakly-meshed topologies, we consider that the normally-open tie lines between nodes 8-21, 9-15, 12-22, 18-33, and 25-29 are closed to create a meshed network. The results obtained from the generalized power flow algorithm are shown in Table 6.3 under the weakly-meshed system column. The nodal voltages and angles obtained from the power flow are used as the steady-state operating points for modal analysis. The statistical parameters of the nodal voltage magnitudes are obtained and plotted as a box diagram shown in Fig. 6.3a. Using the kernel density estimation tool of MATLAB, the PDFs of the voltage magnitudes of the DER buses are plotted in Fig. 6.3b. The box-plots from the stochastic power flow can be used to obtain the worst case scenarios with the renewable and load uncertainties.



(a) Stochastic Variation of Nodal Voltage.



(b) PDFs of Nodal Voltages.

Fig. 6.3: Stochastic Power Flow Results.

6.3 Modal Analysis

The eigenvalue plot of the microgrid state matrix in the frequency or s domain, which is commonly referred to as the root locus plot or modal plot is used to analyze the oscillatory and small signal stability of the system. The real part of the eigenvalue indicates the power of the exponent term in the time response function and the imaginary value indicates the frequency of periodicity ω . As the real part of the eigenvalue σ moves towards the positive x -axis, the stability margin of the system reduces and it is unstable when one or more real parts of the eigenvalues are positive. As the modal analysis is based on the small signal linear model of the system, the analysis is valid only around a given steady-state operating point and therefore has to be studied for the various possible operating conditions and the corresponding operating points. The steady-state solution for the islanded microgrid power flow is obtained from the BFS method. For analyzing the various possibilities and worst case scenarios of operating conditions, the stochastic power flow analysis may be used.

6.3.1 Clustering Eigenmodes

Fig. 6.4 presents the eigenvalues of the system state matrix of the islanded IBR microgrid with grid-forming droop and inertia controllers and grid-feeding converters. The system is stable with all poles on the left half of the s -plane. As there are a number of system states for each IBR, the eigenmodes are divided into clusters as they appear on the plot, for a range of frequency and damping ratio ζ . The slanting lines present in the background of the root locus plot in all the following figures, represents the constant ζ lines. Each of these clusters is linked to a set of system states.

Cluster I comprises high-frequency, underdamped modes and are far from the critical zone and is related to the system impedances such as the line and load impedances and the LCL filter inductance and capacitance. Hence, the system operating conditions mostly affect these modes. However, the first cluster is related to the harmonic stability

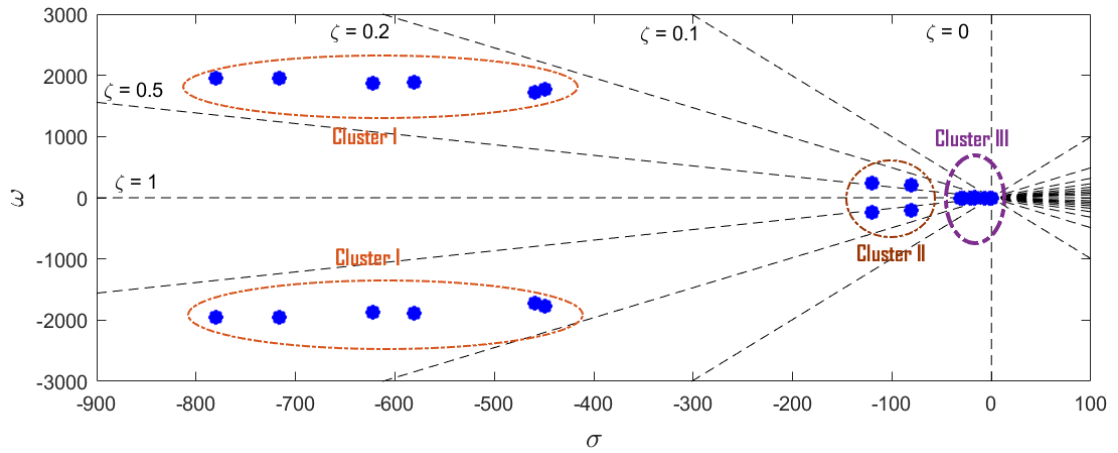


Fig. 6.4: Clustering the Eigenmodes of IBR Microgrid.

and power quality with high frequency oscillatory modes and do not affect the small signal stability margin of the system.

Unlike cluster I and III, the modes of cluster II are damped with high ζ and therefore are not oscillatory and do not impact the small signal stability. The modes of cluster II are sensitive to the states of the inner control loops such as current control in the grid-following IBR and the current and voltage controllers in the grid-forming IBR.

Cluster III is the most critical for the small signal stability assessment as it is the low-frequency mode with considerably low damping. The most critical mode is identified with a frequency of 20 Hz, with $\zeta \approx 0.2$. The most critical modes correspond to the outer loop controls of IBRs, the droop controllers, and the PLL for the grid-following IBRs. The slowest mode is that of the power measurement filter in the droop controller at 5 Hz. Hence, the droop and damping parameters in grid-forming and grid-supporting control impact the small signal stability margin of the system. In the following section, the effect of droop and inertia variation on the eigen trace is discussed.

6.3.2 Impact of Parameter Variation on Eigen Traces

6.3.2.1 Droop Parameters

The root locus plot of the microgrid where all IBRs are equipped with droop control is shown in Fig. 6.5. It is to be noted that the state variables introduced by the LCL filter, Voltage PI, and current PI loops are higher frequency modes and are not affected much by the droop variation. The state variables corresponding to the droop control block influence the cluster III. Based on sensitivity analysis we can identify the state variables that are most sensitive to each inverter's droop coefficient m_p . The pair of eigenvalues that move towards the real axis the fastest with increase in m_p are the ones that first cross the y-axis of the root locus plot. For the 3-IBR case study, the sensitivity of the eigenvalues that reduce the stability margin due to m_p droop variation are: $(m_{p1}, m_{p2}, m_{p3}) = (0.12, 0.3, 0.05)$. Hence, IBR 2 is the most critical unit whose droop has to be scheduled and be mindful of the stability issue. A high m_p indicates that the inverter controls are less responsive to the frequency variations. This explains the reduction of SSS margin with an increase in m_p . A critical value of droop is the value at which the oscillatory modes show a positive real part and the system stability margin reduces to zero. The critical m_p in this case is observed to be 7.9%, beyond which the system is oscillatory unstable.

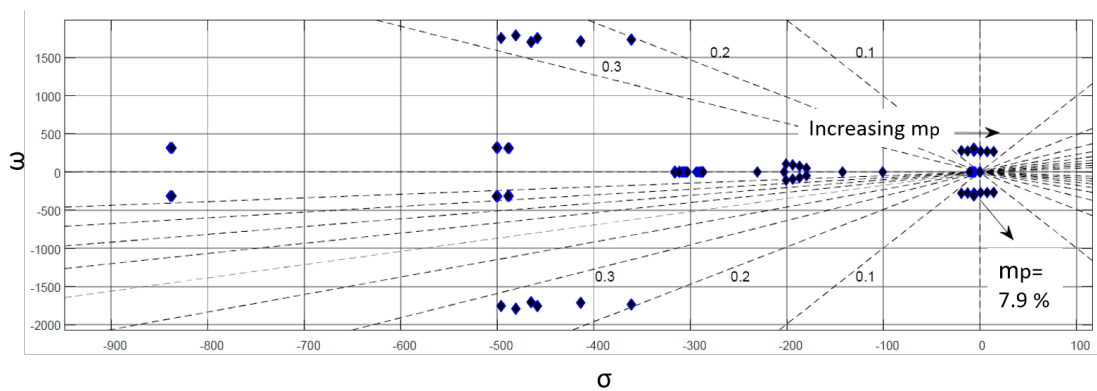


Fig. 6.5: Effect of m_p Variation.

Similarly, we can study the effect of the variation of the $Q - V$ by examining the sensitivity of the state variables to the $Q - V$ droop parameter n_q , which are the cluster III

eigenmodes. The sensitivity of this pair of eigenvalues to the n_q s are: $(n_{q1}, n_{q2}, n_{q3}) = (0.03, 0.4, 0.0006)$. Similar to the previous case, the IBR 2 plays a critical role with respect to the $Q - V$ droop too. However, the effect of n_q droop variation does not adversely affect the stability as m_p . Fig. 6.6 depicts the variation of the n_q and the critical droop. As n_q is increased i.e. if the reactive power control of the inverter becomes less responsive to the node voltage variation at all, two of the real poles of the system break away into a pair of complex poles, i.e. they show an oscillatory behaviour. When n_q is increased to a very high value 16.4% the oscillatory modes break in on the real axis very close to the y axis, and moves in the opposite direction, where one real value approaches the y axis and becomes positive at $n_q = 18.8\%$, which is the critical n_q value. The $Q - V$ droop variation effect is a localized phenomenon especially in larger microgrids and is different for different inverters based on the load connected and the node location.

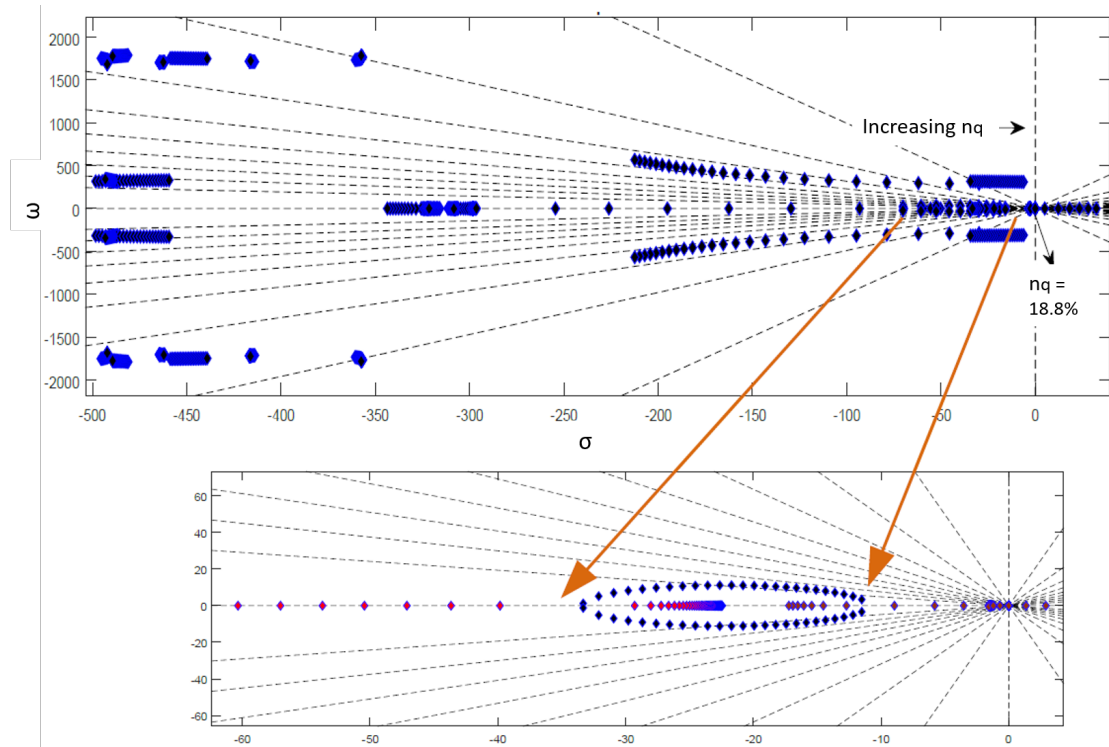


Fig. 6.6: Effect of n_q Variation.

The case studies mentioned above show the local birth (break-away points) and death (break-in points) of periodicity with the variation of the droop parameters, which can be identified as the sub-critical homoclinic hopf bifurcation (HB) in the bifurcation theory that studies the change in the dynamic behavior of the system with respect to the change

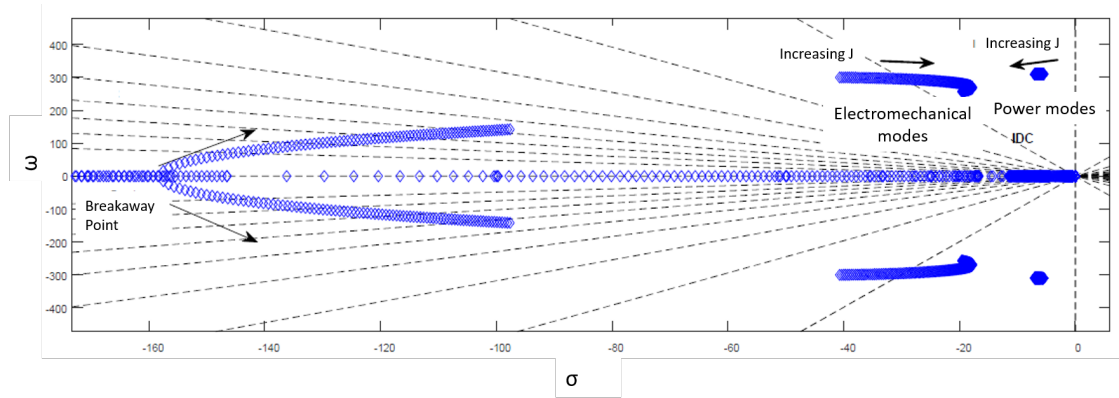
in the parameters [83]. This identification gives scope for quantification of the stability margin based on the mathematical representations of the HB hypersurface which can be computed using the method in [164], that is relevant for large systems for which modal analysis is tedious.

6.3.3 Interaction of Droop and Inertia Controllers

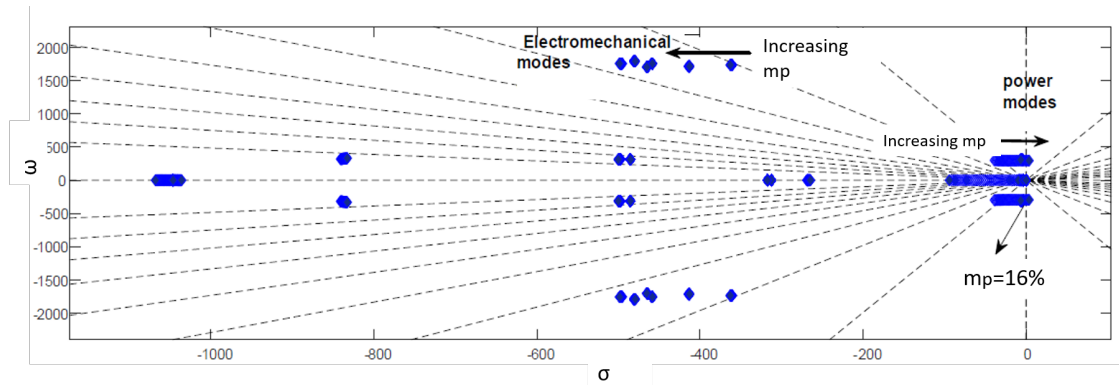
In the sensitivity analysis with all droop-based IBRs, IBR 2 was the critical node, whose droop played a crucial role in determining the stability margin. To study the interaction between swing-based inertia control and droop controllers, the droop control of the IBR 2 has been replaced with the swing equation-based grid-forming inertia control. Thus, the control parameters for node 2 is J , while the other nodes are droop-controlled. The modes of the inverter droop control (IDC) are referred to as inverter power modes and the modes of the swing equation-based control are referred to as the electro-mechanical modes, since the swing equation is based on a virtual rotor and prime-mover input power [48].

An increase in inertia J shifts the inverter power modes towards the left-half of the s -plane and thereby stabilizing the system as shown in Fig. 6.7a. However, an increase in J , with constant m_p as 0.05, shifts the electro-mechanical modes of the swing-based controller to the right, making the stability margin narrower. Fig. 6.7b presents the effect of increase in m_p when J is constant at 0.03. It can be observed that m_p has the reverse effect of J i.e. as the m_p is increased the electromechanical modes are damped and the inverter power modes are destabilized. The critical m_p at which the oscillatory modes become purely imaginary and the stability margin reduces to zero is computed as 16%.

From these plots, we can infer that if the J/D ratio is increased the frequency damping increases while the active power damping reduces. Thus, it is possible to arrive at an optimal trade-off point [34] where both the frequency and the active power response are well-damped while minimizing the requirement of energy storage. For the droop control, it has been shown in Section 5.2 that the droop along with the corner frequency of the LPF ω_c determines the inertia and the damping is directly given by the droop.



(a) Effect of increase of Inertia on Electromechanical and IDC Modes.



(b) Effect of increase of Droop on Electromechanical and IDC Modes.

Fig. 6.7: Interaction of Droop and Inertia Controllers.

Thus, in case of the droop control, the J/D has the constant value of $1/\omega_c$ or T_f . If the J/D ratio is less than ω_c , the frequency response is over-damped and the power response is under-damped in case of droop control, and if the ratio is greater than ω_c , the converse is true.

6.3.4 Design of Active Damping Parameters for SSS

The parameters of the grid-forming units include the active power droop m_p , reactive power droop n_q , and the active damping terms n_{p1} and m_{q1} . The droop parameters are chosen based on the steady-state regulation requirements of the system. This implies that the unit with the lowest droop coefficient contributes the highest to a load increase.

$$\begin{cases} m_p = (\omega_{max} - \omega_{min})/P_{max} \\ n_q = (V_{max} - V_{min})/Q_{max} \end{cases} \quad (6.67)$$

The small signal dynamics of P and Q are given by (6.68) and (6.69), where t_f is the time constant of the LPF. The dynamics of the voltage ΔV_g and phase angle $\Delta\phi$ are expressed as (6.71) and (6.70) respectively. Since n_p and m_q are defined by the system steady-state requirements, n_{p1} and m_{q1} are chosen to meet the SSS criteria.

$$\Delta P_i = \frac{1}{(1+t_f)} \frac{V_i}{Z} (\cos\phi(\Delta V_g) - V_g \sin\phi(\Delta\phi)) \quad (6.68)$$

$$\Delta Q_i = -\frac{1}{(1+t_f)} \frac{V_i}{Z} (\sin\phi(\Delta V_g) + V_g \cos\phi(\Delta\phi)) \quad (6.69)$$

$$\Delta\phi = -(m_p/s + m_{p1}) \Delta P_i \quad (6.70)$$

$$\Delta V_g = -(n_q + n_{q1}s) \Delta Q_i \quad (6.71)$$

The SSS margin of a system is defined in terms of the minimum damping d_{min} and the minimum damping ratio ζ_{min} . The real part of the critical eigenvalue $-\lambda_r + j\lambda_i$ is referred to as the damping d , while the damping ratio ζ is given by (6.72). With increase in m_{p1} in Fig. 6.8a, the complex poles shift towards the real axis causing ζ_{min} to increase. However, the real pole also moves rapidly towards the unstable region decreasing d_{min} . The choice of m_{p1} is affected by contradicting objectives of stability margin and damping ratio. Thus, n_{p1} is chosen to allow the maximum stability margin while meeting the ζ_{min} constraint. With an increase in n_{q1} in Fig. 6.8b, the real pole moves rapidly towards the y-axis giving a dynamics with two distinct real roots, thus reducing the dynamics to a nearly first order characteristic [159]. Conversely, the decrease in n_{q1} renders a second order dynamics.

$$\begin{cases} d = -\lambda_r \\ \zeta = -\lambda_r / \sqrt{\lambda_r^2 + \lambda_i^2} \end{cases} \quad (6.72)$$

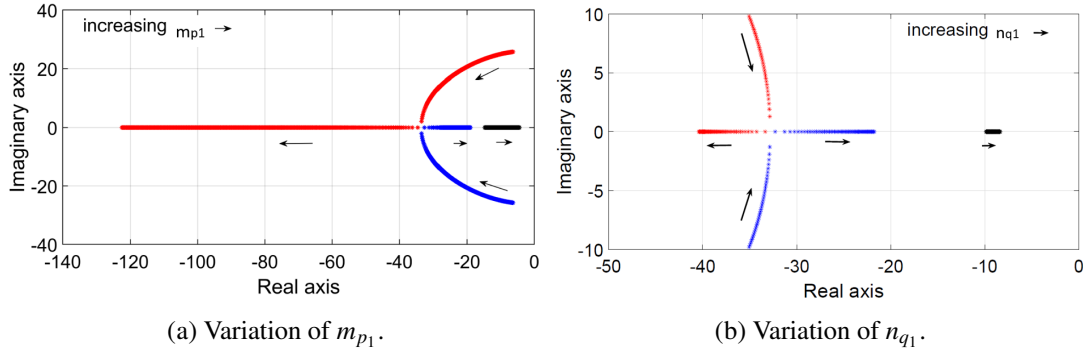


Fig. 6.8: Effect of Variation of Active Damping Parameters in IDCs.

The inertia of the microgrid has to be designed to support the system on the event of unexpected contingencies to improve the transient stability of the system. If the worst system contingency is a generation loss or sudden load increase of P_{cont} and Q_{cont} and the allowable ROCOF and ROCOV limits are defined as $\left(\frac{d\omega}{dt}\right)_{lim}$ and $\left(\frac{dV}{dt}\right)_{lim}$, the required total system inertia may be calculated as (6.73) and (6.74). The system dynamics can be represented by a fifth order characteristic equation when the grid-forming controller is operated in the inertia mode, similar to the cubic equation described in the droop control mode. The corresponding linearized equations of voltage and phase angle are given by (6.76) and (6.75). The root locus plots of the impact of active damping terms on the system dynamics in the inertia mode are shown in the root locus plots of Fig. 6.9. Unlike Fig. 6.8a, both the damping and stability margin decrease with an increase in m_{p1} as indicated by the pole movement in Fig. 6.9a. A similar trend can be observed with the variation of n_{q1} in Fig. 6.9b. Thus, the system dynamics in this control mode can be improved by decreasing m_{p1} and n_{q1} .

$$J_p^{tot} = P_{cont} / \left(\frac{d\omega}{dt}\right)_{lim} \quad (6.73)$$

$$J_q^{tot} = Q_{cont} / \left(\frac{dV}{dt}\right)_{lim} \quad (6.74)$$

$$\Delta\phi = -\left(\frac{m_p}{s} + m_{p1}\right) \frac{\Delta P}{(1 + J_p n_p s)} \quad (6.75)$$

$$\Delta V_g = -(n_q + n_{q1} s) \frac{\Delta Q}{(1 + J_q m_q)} \quad (6.76)$$

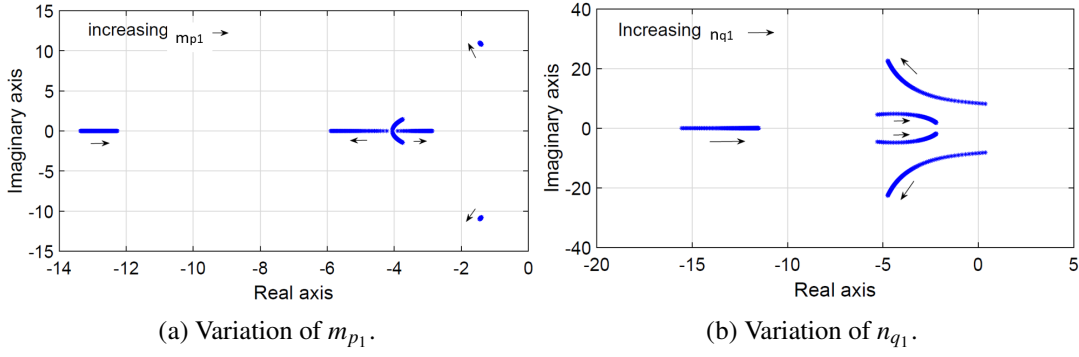


Fig. 6.9: Effect of Variation of Active Damping Parameters in Inertia Controllers.

6.4 Deriving Stability Limits for Droop Parameters

The modal analysis method of determining the system stability by explicitly computing the eigenvalues of the system state matrix for every operating point is computationally inefficient for larger systems with a numerous parameters. The computation problem grows exponentially with the number of parameters. Hence methods that provide an alternative to the eigenvalue estimation that can estimate the closed form expressions of the parametrically stable region can be employed to derive the stability constraints in the higher level controls that schedule the frequency response parameters of the IBRs.

In this context, the Lyapunov function approach can be a tractable alternative. Consider the frequency dynamics of the microgrid represented by (6.77) from the small signal model of the microgrid described in Section 6.1, where \mathbf{V} and $\boldsymbol{\delta}$ represent the deviations in the nodal voltage magnitudes and angles. D_p and D_q are diagonal matrices with the inverse of the nodal $P-f$ and $Q-V$ droop coefficients, and T_f is the LPF time constant. The impedance matrices in the model are given by (6.78), where Y_{net} and Y_{load} are the network and load admittance matrices defined in the Laplace domain in [142].

$$\begin{cases} T_f D_p \ddot{\boldsymbol{\delta}} + (D_p - B') \dot{\boldsymbol{\delta}} + B \boldsymbol{\delta} + (G + \bar{G}) \mathbf{V} - G' \dot{\mathbf{V}} = 0 \\ (T_f D_q - B') \dot{\mathbf{V}} + (D_q + B + \bar{B}) \mathbf{V} - G \boldsymbol{\delta} + G' \dot{\boldsymbol{\delta}} = 0 \end{cases} \quad (6.77)$$

$$\begin{cases} B = -Im[Y_{net}^0], G = Re[Y_{net}^0] \\ \bar{B} = -2Im[Y_{load}^0], \bar{G} = 2Re[Y_{load}^0] \\ B' = Im[Y_{net}^1 + Y_{load}^1], G' = -Re[Y_{net}^1 + Y_{load}^1] \end{cases} \quad (6.78)$$

With n nodes, and if state vector $x = [\boldsymbol{\delta}, \mathbf{V}, \dot{\boldsymbol{\delta}}]$, the system state matrix is a $3n \times 3n$ matrix. Applying the invariance principle of the Lyapunov function, if there exists $3n \times 3n$ matrices $\Xi > 0$ and $\Pi \geq 0$ satisfying (6.79), then the system trajectories converge to the equilibrium, and the system is therefore small signal stable. $W(x)$ is known as the Lyapunov function. Therefore, the conditions for existence of such matrices represent the closed form criteria for the SSS of the microgrid.

$$W(x) = x^T \Xi x, \dot{W}(x) \leq -x^T \Pi x \leq 0 \quad (6.79)$$

The IBR microgrid stability conditions for a lossy microgrid can be derived as shown in [142]. The conditions in (6.80) represent the nodal droop conditions. If there are multiple IBRs in the node, their equivalent collective stiffness is considered as the criteria. Both the grid-forming and grid-following frequency responsive response can contribute to the nodal droop/stiffness.

$$\begin{cases} G_{ij} + \bar{G}_{ij} + G'_{ij}/2T_f \geq 0 \\ D_{p_{ij}}/2 - B'_{ij} + 2T_f B_{ij} \geq 0 \\ D_{p_{ij}} - 2B'_{ij} - G'_{ij}/2 - T_f (G_{ij} + \bar{G}_{ij}) \geq 0 \\ D_{q_{ij}} - B_{ij}/T_f \geq 0 \\ D_{q_{ij}} + B_{ij} + \bar{B}_{ij} - G_{ij} - G'_{ij}/(2T_f) - 3\bar{G}_{ij}/2 \geq 0 \\ 2B_{ij} - \bar{G}_{ij} \geq \left(G_{ij} + G'_{ij}/(2T_f) \right) \left(D_{q_{ij}} - B'_{ij}/T_f \right)^{-1} \left(G_{ij} + G'_{ij}/(2T_f) \right) \end{cases} \quad (6.80)$$

The conditions in (6.80) for every pair of electrically adjacent nodes i and j , give the stable range of droop parameters based on the system data. Unlike modal analysis that

has to be carried out for every change in the network parameters, the derived conditions serve as a set of closed form constraints for the droop settings of IBRs.

6.5 Chapter Summary

The virtual inertia and frequency control strategies presented in the previous chapters have been developed to enhance the frequency stability of the system. Using the derived small signal model and the islanded microgrid power flow, the eigenmodes of the IBR microgrid have been analyzed for parameter variation and the interaction of different IBR controls in this chapter. The discussed model and analysis connects the individual IBR control strategies back to the bigger picture, which is the system stability. The next chapter highlights the major take-aways from the thesis and the possible avenues for further research in this topic.

Chapter 7

Conclusion

Design and control of hybrid ESS and other available flexibilities for IBR frequency response control have been studied in this work. The central idea of the thesis is that the frequency responsive controls and their parameters affect the damping of the system and therefore the oscillatory stability of the system, specifically in the context of 100% IBR microgrids. As a solution, MPC control strategies that can simultaneously provide inertia emulation and damping control have been proposed using the available flexibility based on the system requirements assessed by its model. Cooperative higher level strategies have been explored to handle the limited and time-varying flexibilities of the individual DERs whilst they are coordinated to collectively control the system frequency and damping characteristics. The primary outcomes of the research are listed below.

7.1 Research Outcomes

1. A storage sizing methodology has been discussed in Chapter 3 exclusively for the fast frequency response and inertia emulation control of IBRs. The flexibilities of the loads and PV inverters are accounted in the virtual battery model, to define the power and energy capacity of the additional storage reserves to meet a given set of grid code requirements of frequency response.

2. The cooperative MPC grid-following strategy proposed in Chapter 4 allows the control to simultaneously optimize the different frequency response characteristics such as the initial ROCOF, f_{nadir} , peak overshoot, and the settling time. A high inertia is required to optimize the initial ROCOF and f_{nadir} , whereas a high damping is required to minimize the peak overshoot and the settling time of the response. With the conventional controls, this requires separate inertia and damping control reserves however by simultaneously tuning the inertia and damping parameters. The optimal response can be provided with lesser reserve capacity. The individual IBRs are coordinated by a higher level consensus algorithm to account for the time-varying resource constraints.
3. An isochronous grid-forming IBR control has been discussed in Chapter 5 for one or few dedicated grid-forming units for the autonomous operation of IBR microgrids. The proposed framework is implemented with local MPC controllers coordinated by a load sharing algorithm unlike traditional isochronous controllers where parallel operation may lead to instability. Further, for systems with a large number of flexible IBRs, a droop-based grid-forming approach has been implemented using a cooperative MPC framework that allows for the optimization of the different frequency response metrics while coordinating the load sharing between the participating DERs.
4. Finally, the small signal model of IBR-microgrids with grid-forming and grid-following frequency response is derived in Chapter 6 and the stability is analyzed by modal analysis for the variation of control parameters. The steady-state information for islanded microgrids is obtained from the stochastic backward forward sweep power flow algorithm developed in this work. Finally, a set of stability criteria for the range of droop parameters have been derived using the Lyapunov function. They do not require separate analysis for different steady-state operating points, and is therefore suitable for larger systems. Topics such as these need further research and are timely with the growing influx of controllable power electronics in power systems. The recommendations for promising avenues of further research on these topics are listed below.

7.2 Recommendations for Future Works

Analysis of the impact of inertia emulation by IBRs and the impact of their interaction on the stability of the system is an emerging area of research that has a growing scope with the increasing penetration of power electronics into the synchronous power systems. The particular case of 100% IBR microgrids has been largely studied in this thesis with a futuristic view. Massive integration of IBRs and the impact of their controls in the transmission networks are of high demand as large clusters of intermittent penetrations are being observed to have adverse effects on the system operations and stability.

Below are the recommendations of some timely topics for the interested researchers to continue this work and explore further.

1. The storage sizing methodology for FFR and inertia emulation in Chapter 3 may be improved by considering the different storage technology characteristics and their economics to derive an optimal energy storage mix.
2. The analysis of the performance of MPC control strategies for various prediction horizons and their trade-offs between the computation, memory requirement, and performance enhancement can be interesting to optimize the controller. A high computation and memory search requirement is not ideal for the fast-frequency controllers or inertia emulators. Hence, explicit MPC implementations may be explored for a faster yet optimal performance.
3. The MPC is heavily reliant on the model accuracy, hence non-linear MPCs or other optimal control alternatives with black box models, such as fuzzy or robust controllers that consider the uncertainties in the model and noise such as H_∞ may be explored as alternatives.
4. For the small signal stability analysis, methods that are independent of steady-state operating points and linearized models, such as energy function methods, bifurcation hypersurface formulation may be studied further to derive the closed form stability criteria on the parameters, especially for large systems.

5. Currently there exists very few markets for fast frequency response services such as that in the UK and not many ancillary services markets for the procurement of inertia services, however with the transition of the power system with the massive penetration of converter-based generation, the need for inertia services is implicit. Market mechanisms for inertia and fast-frequency ancillary services provisions are crucial for providing cost-effective ancillary services for grid stability and therefore can be a timely topic for future works.

References

- [1] (2019) Singapore EMA: Singapore Energy Statistics. [Online]. Available: <https://www.ema.gov.sg> xi, 2, 3
- [2] (2016) UNFCCC: Paris Agreement, Decision 1/CP.21, Article 17. [Online]. Available: <https://unfccc.int> 1
- [3] M. Pehl, A. Arvesen, F. Humpenöder, A. Popp, E. G. Hertwich, and G. Luderer, “Understanding future emissions from low-carbon power systems by integration of life-cycle assessment and integrated energy modelling,” *Nature Energy*, vol. 2, no. 12, pp. 939–945, dec 2017. 1, 4
- [4] (2019) NASA’s Global Climate Change Website: A Degree of Concern: Why Global Temperatures Matter. [Online]. Available: <https://climate.nasa.gov> 2
- [5] (2020, Mar.) IRENA: Renewable Capacity Highlights. [Online]. Available: <https://www.irena.org> 2
- [6] (2018) SERIS: Solar Energy Roadmap for Singapore. [Online]. Available: <http://www.seris.sg> 4
- [7] M. Rezkalla, A. Zecchino, S. Martinenas, A. M. Prostejovsky, and M. Marinelli, “Comparison between synthetic inertia and fast frequency containment control based on single phase EVs in a microgrid,” *Applied Energy*, vol. 210, pp. 764–775, 2018. 5, 6
- [8] N. Hatziargyriou, *Microgrids: Architectures and Control*. Wiley, 2013. 6

- [9] C. Feng, F. Wen, S. You, Z. Li, F. Shahnia, and M. Shahidehpour, “Coalitional Game-Based Transactive Energy Management in Local Energy Communities,” *IEEE Transactions on Power Systems*, vol. 35, no. 3, pp. 1729–1740, 2020. [7](#)
- [10] T. Van Der Schoor and B. Scholtens, “Power to the people: Local community initiatives and the transition to sustainable energy,” *Renewable and Sustainable Energy Reviews*, vol. 43, pp. 666–675, 2015. [7](#)
- [11] J. Lowitzsch, C. E. Hoicka, and F. J. van Tulder, “Renewable energy communities under the 2019 European Clean Energy Package – Governance model for the energy clusters of the future?” *Renewable and Sustainable Energy Reviews*, vol. 122, no. October 2019, 2020. [7](#)
- [12] P. Chakraborty, E. Baeyens, K. Poolla, P. P. Khargonekar, and P. Varaiya, “Sharing Storage in a Smart Grid: A Coalitional Game Approach,” *IEEE Transactions on Smart Grid*, vol. 10, no. 4, pp. 4379–4390, 2019. [7](#), [8](#), [25](#), [26](#), [27](#), [43](#)
- [13] D. H. Tungadio and Y. Sun, “Load frequency controllers considering renewable energy integration in power system,” *Energy Reports*, vol. 5, pp. 436–453, nov 2019. [7](#)
- [14] A. Ibraheem, P. Kumar, and D. P. Kothari, “Recent philosophies of automatic generation control strategies in power systems,” *IEEE Transactions on Power Systems*, vol. 20, no. 1, pp. 346–357, 2005. [7](#)
- [15] R. Patel, C. Li, L. Meegahapola, B. Mcgrath, and X. Yu, “Enhancing Optimal Automatic Generation Control in a Multi-Area Power System With Diverse Energy Resources,” *IEEE Transactions on Power Systems*, vol. 34, no. 5, pp. 3465–3475, 2019. [7](#)
- [16] D. M. Greenwood, K. Y. Lim, C. Patsios, P. F. Lyons, Y. S. Lim, and P. C. Taylor, “Frequency response services designed for energy storage,” *Applied Energy*, vol. 203, pp. 115–127, 2017. [8](#)

- [17] L. H. Koh, P. Wang, F. H. Choo, K. J. Tseng, Z. Gao, and H. B. Püttgen, “Operational adequacy studies of a PV-based and energy storage stand-alone microgrid,” *IEEE Transactions on Power Systems*, vol. 30, no. 2, pp. 892–900, 2015. [8](#), [28](#)
- [18] G. Delille, B. François, and G. Malarange, “Dynamic frequency control support by energy storage to reduce the impact of wind and solar generation on isolated power system’s inertia,” *IEEE Transactions on Sustainable Energy*, vol. 3, no. 4, pp. 931–939, 2012. [8](#), [27](#)
- [19] Z. Lu, H. Li, and Y. Qiao, “Probabilistic Flexibility Evaluation for Power System Planning Considering Its Association With Renewable Power Curtailment,” *IEEE Transactions on Power Systems*, vol. 33, no. 3, pp. 3285–3295, 2018. [8](#)
- [20] C. Zhong, Y. Zhou, and G. Yan, “A novel frequency regulation strategy for a PV system based on the curtailment power-current curve tracking algorithm,” *IEEE Access*, vol. 8, pp. 77 701–77 715, 2020. [8](#)
- [21] Z. Zhou, C. Wang, and L. Ge, “Operation of stand-alone microgrids considering the load following of biomass power plants and the power curtailment control optimization of wind turbines,” *IEEE Access*, vol. 7, pp. 186 115–186 125, 2019. [8](#)
- [22] F. Carducci, A. Giovannelli, M. Renzi, and G. Comodi, “Improving flexibility of industrial microgrids through thermal storage and HVAC management strategies,” *Energy Procedia*, vol. 142, pp. 2728–2733, 2017. [8](#)
- [23] S. H. Tindemans, V. Trovato, and G. Strbac, “Decentralized Control of Thermostatic Loads for Flexible Demand Response,” *IEEE Transactions on Control Systems Technology*, vol. 23, no. 5, pp. 1685–1700, 2015. [8](#)
- [24] A. Delavari and I. Kamwa, “Sparse and Resilient Hierarchical Direct Load Control for Primary Frequency Response Improvement and Inter-Area Oscillations Damping,” *IEEE Transactions on Power Systems*, vol. 33, no. 5, pp. 5309–5318, 2018. [8](#)

- [25] X. Lou, D. K. Yau, H. H. Nguyen, and B. Chen, "Profit-optimal and stability-aware load curtailment in smart grids," *IEEE Transactions on Smart Grid*, vol. 4, no. 3, pp. 1411–1420, 2013. [8](#)
- [26] T. Kerdphol, F. S. Rahman, Y. Mitani, K. Hongesombut, and S. Küfeoğlu, "Virtual inertia control-based model predictive control for microgrid frequency stabilization considering high renewable energy integration," *Sustainability (Switzerland)*, vol. 9, no. 5, 2017. [8](#), [24](#), [51](#)
- [27] N. Pogaku, M. Prodanović, and T. G. Green, "Modeling, analysis and testing of autonomous microgrid of an inverter-based microgrid," *IEEE Trans. on Power Electronics*, vol. 22, no. 2, pp. 613–625, 2007. [8](#), [15](#), [16](#), [19](#), [31](#), [47](#), [113](#), [114](#)
- [28] E. Barklund, N. Pogaku, M. Prodanovic, C. Hernandez-Aramburo, and T. C. Green, "Energy management in autonomous microgrid using stability-constrained droop control of inverters," *IEEE Transactions on Power Electronics*, vol. 23, no. 5, pp. 2346–2352, 2008. [8](#), [13](#), [31](#)
- [29] H. Bevrani, T. Ise, and Y. Miura, "Virtual synchronous generators: A survey and new perspectives," *International Journal of Electrical Power and Energy Systems*, vol. 54, pp. 244–254, 2014. [8](#)
- [30] S. Kundu, K. Kalsi, and S. Backhaus, "Approximating flexibility in distributed energy resources: A geometric approach," *20th Power Systems Computation Conference, PSCC 2018*, pp. 1–7, 2018. [8](#), [27](#)
- [31] P. Tielens and D. Van Hertem, "Receding Horizon Control of Wind Power to Provide Frequency Regulation," *IEEE Transactions on Power Systems*, vol. 32, no. 4, pp. 2663–2672, 2017. [9](#)
- [32] T. S. Borsche, T. Liu, and D. J. Hill, "Effects of rotational Inertia on power system damping and frequency transients," *Proceedings of the IEEE Conference on Decision and Control*, vol. 54rd IEEE, no. Cdc, pp. 5940–5946, 2015. [9](#)

- [33] H. E. Brown and C. L. DeMarco, “Synthetic inertia and small signal instability,” in *NAPS 2016 - 48th North American Power Symposium, Proceedings*, 2016. [9](#), [29](#), [109](#)
- [34] P. Tielens and D. Van Hertem, “Influence of system wide implementation of virtual inertia on small-signal stability,” in *2016 IEEE International Energy Conference, ENERGYCON 2016*, 2016. [9](#), [29](#), [109](#), [132](#)
- [35] A. Ulbig, T. S. Borsche, and G. Andersson, “Impact of low rotational inertia on power system stability and operation,” *IFAC Proceedings Volumes (IFAC-PapersOnline)*, vol. 19, pp. 7290–7297, 2014. [9](#)
- [36] F. Dorfler, J. W. Simpson-Porco, and F. Bullo, “Breaking the hierarchy: Distributed control and economic optimality in Microgrids,” *IEEE Transactions on Control of Network Systems*, vol. 3, no. 3, pp. 241–253, 2016. [13](#), [14](#)
- [37] N. Soni, S. Doolla, and M. C. Chandorkar, “Analysis of Frequency Transients in Isolated Microgrids,” *IEEE Transactions on Industry Applications*, vol. 53, no. 6, pp. 5940–5951, 2017. [13](#), [19](#), [23](#), [68](#)
- [38] M. D. Ilic, R. Jaddivada, and M. Korpas, “Interactive protocols for distributed energy resource management systems (DERMS),” *IET Generation, Transmission and Distribution*, vol. 14, no. 11, pp. 2065–2081, 2020. [13](#)
- [39] J. A. Lopes, C. L. Moreira, and A. G. Madureira, “Defining control strategies for analysing microgrids islanded operation,” *2005 IEEE Russia Power Tech, PowerTech*, vol. 21, no. 2, pp. 916–924, 2005. [13](#)
- [40] J. Pahasa and I. Ngamroo, “Coordinated PHEV, PV, and ESS for Microgrid Frequency Regulation Using Centralized Model Predictive Control Considering Variation of PHEV Number,” *IEEE Access*, vol. 6, pp. 69 151–69 161, 2018. [13](#)
- [41] M. M. A. Abdelaziz, M. F. Shaaban, H. E. Farag, and E. F. El-Saadany, “A multistage centralized control scheme for islanded microgrids with PEVs,” *IEEE Transactions on Sustainable Energy*, vol. 5, no. 3, pp. 927–937, 2014. [13](#)

- [42] N. L. Díaz, A. C. Luna, J. C. Vasquez, and J. M. Guerrero, "Centralized Control Architecture for Coordination of Distributed Renewable Generation and Energy Storage in Islanded AC Microgrids," *IEEE Transactions on Power Electronics*, vol. 32, no. 7, pp. 5202–5213, 2017. [13](#)
- [43] J. M. Guerrero, J. C. Vasquez, J. Matas, L. G. De Vicuña, and M. Castilla, "Hierarchical control of droop-controlled AC and DC microgrids - A general approach toward standardization," *IEEE Transactions on Industrial Electronics*, vol. 58, no. 1, pp. 158–172, 2011. [13](#), [14](#), [15](#)
- [44] J. W. Simpson-Porco, Q. Shafiee, F. Dorfler, J. C. Vasquez, J. M. Guerrero, and F. Bullo, "Secondary Frequency and Voltage Control of Islanded Microgrids via Distributed Averaging," *IEEE Transactions on Industrial Electronics*, vol. 62, no. 11, pp. 7025–7038, 2015. [13](#), [15](#)
- [45] H. Xin, L. Zhang, Z. Wang, D. Gan, and K. P. Wong, "Control of island AC microgrids using a fully distributed approach," *IEEE Transactions on Smart Grid*, vol. 6, no. 2, pp. 943–945, 2015. [13](#)
- [46] S. T. Cady, A. D. Member, and C. N. Hadjicostis, "A Distributed Generation Control Architecture for Islanded AC Microgrids," *IEEE Transactions on Control Systems Technology*, vol. 23, no. 5, pp. 1717–1735, 2015. [13](#)
- [47] M. C. Chandorkar, D. M. Divan, and R. Adapa, "Control of parallel connected inverters in standalone ac supply systems," *IEEE Transactions on Industry Applications*, vol. 29, no. 1, pp. 136–143, 1993. [13](#), [16](#), [19](#), [29](#)
- [48] N. Soni, S. Doolla, and M. C. Chandorkar, "Inertia design methods for islanded microgrids having static and rotating energy sources," *2015 IEEE Industry Applications Society Annual Meeting*, vol. 52, no. 6, pp. 1–8, 2015. [13](#), [16](#), [31](#), [47](#), [91](#), [92](#), [132](#)
- [49] A. K. Jain, A. Nagarajan, I. Chernyakhovskiy, T. Bowen, B. Mather, and J. Cochran, "Evolution of Distributed Energy Resource Grid Interconnection

- Standards for Integrating Emerging Storage Technologies,” *51st North American Power Symposium, NAPS 2019*, vol. 4105, no. 2009, 2019. [15](#)
- [50] J. Rocabert, A. Luna, F. Blaabjerg, and P. Rodríguez, “Control of Power Converters in AC Microgrids,” *IEEE Transactions on Power Electronics*, vol. 27, no. 11, pp. 4734–4749, 2012. [15](#), [16](#), [85](#)
- [51] X. Wang, J. M. Guerrero, Z. Chen, and F. Blaabjerg, “Distributed energy resources in grid interactive AC microgrids,” *2nd International Symposium on Power Electronics for Distributed Generation Systems, PEDG 2010*, pp. 806–812, 2010. [16](#)
- [52] T. Kerdphol, F. S. Rahman, Y. Mitani, M. Watanabe, and S. Kufeoglu, “Robust Virtual Inertia Control of an Islanded Microgrid Considering High Penetration of Renewable Energy,” *IEEE Access*, vol. 6, no. February, pp. 625–636, 2018. [16](#)
- [53] N. R. Ullah, T. Thiringer, and D. Karlsson, “Voltage and transient stability support by wind farms complying with the E.ON netz grid code,” *IEEE Transactions on Power Systems*, vol. 22, no. 4, pp. 1647–1656, 2007. [16](#)
- [54] P. Unruh, M. Nuschke, P. Strauß, and F. Welck, “Overview on grid-forming inverter control methods,” *Energies*, vol. 13, no. 10, 2020. [16](#)
- [55] M. Chlela, D. Mascarella, G. Joos, and M. Kassouf, “Fallback control for isochronous energy storage systems in autonomous microgrids under denial-of-service cyber-attacks,” *IEEE Transactions on Smart Grid*, vol. 9, no. 5, pp. 4702–4711, 2018. [16](#)
- [56] I. U. Nutkani and D. G. Holmes, “Hybrid Isochronous-Droop Control for Power Management in DC microgrids,” *2017 19th European Conference on Power Electronics and Applications, EPE 2017 ECCE Europe*, vol. 2017-January, pp. 4085–4091, 2017. [16](#)
- [57] V. Knap, S. K. Chaudhary, D. I. Stroe, M. Swierczynski, B. I. Craciun, and R. Teodorescu, “Sizing of an energy storage system for grid inertial response and

- primary frequency reserve,” *IEEE Transactions on Power Systems*, vol. 31, no. 5, pp. 3447–3456, 2016. [16](#), [28](#), [45](#)
- [58] R. Eriksson, N. Modig, and K. Elkington, “Synthetic inertia versus fast frequency response : a definition,” *IET Renewable Power Generation*, vol. 12, pp. 507–514, 2018. [17](#), [18](#)
- [59] U. Markovic, Z. Chu, P. Aristidou, and G. Hug, “LQR-Based Adaptive Virtual Synchronous Machine for Power Systems With High Inverter Penetration,” *IEEE Transactions on Sustainable Energy*, vol. 10, no. 3, pp. 1501–1512, 2019. [18](#), [23](#), [58](#), [59](#), [94](#)
- [60] U. Tamrakar, T. M. Hansen, R. Tonkoski, and D. A. Copp, “Model Predictive Frequency Control of Low Inertia Microgrids,” *IEEE International Symposium on Industrial Electronics*, vol. 2019-June, pp. 2111–2116, 2019. [18](#), [24](#)
- [61] M. Li, W. Huang, T. NengLing, L. Yang, D. Duan, and Z. Ma, “A Dual-Adaptivity Inertia Control Strategy for Virtual Synchronous Generator,” *IEEE Transactions on Power Systems*, vol. PP, no. c, pp. 1–1, 2019. [18](#)
- [62] B. B. Johnson, S. V. Dhople, A. O. Hamadeh, and P. T. Krein, “Synchronization of parallel single-phase inverters with virtual oscillator control,” *IEEE Transactions on Power Electronics*, vol. 29, no. 11, pp. 6124–6138, 2014. [19](#), [22](#)
- [63] U. Tamrakar, D. Shrestha, M. Maharjan, B. P. Bhattarai, T. M. Hansen, and R. Tonkoski, “Virtual inertia: Current trends and future directions,” *Applied Sciences (Switzerland)*, vol. 7, no. 7, pp. 1–29, 2017. [19](#), [20](#), [21](#), [22](#), [51](#)
- [64] Z. Peng, J. Wang, D. Bi, Y. Dai, and Y. Wen, “The Application of Microgrids Based on Droop Control with Coupling Compensation and Inertia,” *IEEE Transactions on Sustainable Energy*, vol. 3029, no. c, 2017. [19](#)
- [65] J. Driesen and K. Visscher, “Virtual synchronous generators,” *IEEE Power and Energy Society 2008 General Meeting: Conversion and Delivery of Electrical Energy in the 21st Century, PES*, pp. 8–10, 2008. [20](#)

- [66] T. Vu Van, K. Visscher, J. Diaz, V. Karapanos, A. Woyte, M. Albu, J. Bozelie, T. Loix, and D. Federenciuc, "Virtual synchronous generator: An element of future grids," *IEEE PES Innovative Smart Grid Technologies Conference Europe, ISGT Europe*, pp. 1–7, 2010. [20](#)
- [67] V. Karapanos, S. De Haan, and K. Zwetsloot, "Real time simulation of a power system with VSG hardware in the loop," *IECON Proceedings (Industrial Electronics Conference)*, pp. 3748–3754, 2011. [20](#), [51](#)
- [68] D. Shrestha, U. Tamrakar, Z. Ni, and R. Tonkoski, "Experimental verification of virtual inertia in diesel generator based microgrids," *Proceedings of the IEEE International Conference on Industrial Technology*, pp. 95–100, 2017. [20](#)
- [69] K. Sakimoto, Y. Miura, and T. Ise, "Stabilization of a power system with a distributed generator by a Virtual Synchronous Generator function," *8th International Conference on Power Electronics - ECCE Asia: "Green World with Power Electronics", ICPE 2011-ECCE Asia*, no. 2, pp. 1498–1505, 2011. [21](#)
- [70] J. Alipoor, Y. Miura, and T. Ise, "Power system stabilization using virtual synchronous generator with alternating moment of inertia," *IEEE Journal of Emerging and Selected Topics in Power Electronics*, vol. 3, no. 2, pp. 451–458, 2015. [21](#), [23](#), [58](#)
- [71] K. Sakimoto, Y. Miura, and T. Ise, "Stabilization of a power system including inverter-type distributed generators by a virtual synchronous generator," *Electrical Engineering in Japan (English translation of Denki Gakkai Ronbunshi)*, vol. 187, no. 3, pp. 7–17, 2014. [21](#)
- [72] P. Rodriguez, C. Citro, J. I. Candela, J. Rocabert, and A. Luna, "Flexible Grid Connection and Islanding of SPC-Based PV Power Converters," *IEEE Transactions on Industry Applications*, vol. 54, no. 3, pp. 2690–2702, 2018. [21](#)
- [73] T. Shintai, Y. Miura, and T. Ise, "Oscillation damping of a distributed generator using a virtual synchronous generator," *IEEE Transactions on Power Delivery*, vol. 29, no. 2, pp. 668–676, 2014. [21](#)

- [74] Q. C. Zhong and G. Weiss, “Synchronverters: Inverters that mimic synchronous generators,” *IEEE Transactions on Industrial Electronics*, vol. 58, no. 4, pp. 1259–1267, 2011. [21](#)
- [75] R. Rosso, S. Engelken, and M. Liserre, “Robust stability analysis of synchronverters operating in parallel,” *IEEE Transactions on Power Electronics*, vol. 34, no. 11, pp. 11 309–11 319, 2019. [21](#)
- [76] Z. Shuai, W. Huang, Z. J. Shen, A. Luo, and Z. Tian, “Active Power Oscillation and Suppression Techniques between Two Parallel Synchronverters during Load Fluctuations,” *IEEE Transactions on Power Electronics*, vol. 35, no. 4, pp. 4127–4142, 2020. [21](#)
- [77] Q. C. Zhong, P.-L. P. Nguyen, Z. Ma, and W. Sheng, “Self-synchronised Synchronverters: Inverters without a Dedicated Synchronisation Unit,” *IEEE Transactions on Power Electronics*, vol. 29, no. c, pp. 1–1, 2014. [22](#)
- [78] B. B. Johnson, S. V. Dhople, J. L. Cale, A. O. Hamadeh, and P. T. Krein, “Oscillator-based inverter control for islanded three-phase microgrids,” *IEEE Journal of Photovoltaics*, vol. 4, no. 1, pp. 387–395, 2014. [22](#)
- [79] B. B. Johnson, M. Sinha, N. G. Ainsworth, F. Dörfler, and S. V. Dhople, “Synthesizing Virtual Oscillators to Control Islanded Inverters,” *IEEE Transactions on Power Electronics*, vol. 31, no. 8, pp. 6002–6015, 2016. [22](#)
- [80] M. Sinha, F. Dörfler, B. B. Johnson, and S. V. Dhople, “Virtual Oscillator Control subsumes droop control,” *Proceedings of the American Control Conference*, vol. 2015-July, pp. 2353–2358, 2015. [22](#)
- [81] B. Johnson, M. Rodriguez, M. Sinha, and S. Dhople, “Comparison of virtual oscillator and droop control,” *IEEE 18th Workshop on Control and Modeling for Power Electronics (COMPEL)*, no. September, pp. 1–6, 2017. [22](#)
- [82] G. Díaz, C. González-Morán, J. Gómez-Aleixandre, and A. Diez, “Complex-valued state matrices for simple representation of large autonomous microgrids

- supplied by PQ and Vf generation,” *IEEE Transactions on Power Systems*, vol. 24, no. 4, pp. 1720–1730, 2009. [22](#)
- [83] G. Diaz, C. Gonzalez-Moran, J. Gomez-Aleixandre, and A. Diez, “Scheduling of droop coefficients for frequency and voltage regulation in isolated microgrids,” *IEEE Transactions on Power Systems*, vol. 25, no. 1, pp. 489–496, feb 2010. [23](#), [132](#)
- [84] N. M. Dehkordi, N. Sadati, and M. Hamzeh, “Robust tuning of transient droop gains based on Kharitonov’s stability theorem in droopcontrolled microgrids,” *IET Generation, Transmission and Distribution*, vol. 12, no. 14, pp. 3495–3501, 2018. [23](#)
- [85] M. Altin, J. C. Kuhlmann, K. Das, and A. D. Hansen, “Optimization of synthetic inertial response from wind power plants,” *Energies*, vol. 11, no. 5, 2018. [23](#)
- [86] E. Tegling, M. Andreasson, J. W. Simpson-Porco, and H. Sandberg, “Improving performance of droop-controlled microgrids through distributed PI-control,” *Proceedings of the American Control Conference*, vol. 2016-July, pp. 2321–2327, 2016. [23](#)
- [87] W. Zhang, A. M. Cantarellas, J. Rocabert, A. Luna, and P. Rodriguez, “Synchronous Power Controller with Flexible Droop Characteristics for Renewable Power Generation Systems,” *IEEE Transactions on Sustainable Energy*, vol. 7, no. 4, pp. 1572–1582, 2016. [23](#)
- [88] N. Sockeel, J. Gafford, B. Papari, and M. Mazzola, “Virtual Inertia Emulator-based Model Predictive Control for Grid Frequency Regulation Considering High Penetration of Inverter-based Energy Storage System,” *IEEE Transactions on Sustainable Energy*, vol. 3029, 2020. [24](#), [51](#)
- [89] C. Jin, W. Li, J. Shen, P. Li, L. Liu, and K. Wen, “Active Frequency Response Based on Model Predictive Control for Bulk Power System,” *IEEE Transactions on Power Systems*, vol. 34, no. 4, pp. 3002–3013, 2019. [24](#)

- [90] J. A. DeCastro, “Rate-Based Model Predictive Control of Turbofan Engine Clearance,” *Journal of Propulsion and Power*, vol. 23, no. 4, pp. 804–813, Jul. 2007. [25](#)
- [91] M. Huang, H. Nakada, S. Polavarapu, K. Butts, and I. Kolmanovsky, “Rate-Based Model Predictive Control of Diesel Engines,” *IFAC Proceedings Volumes*, vol. 46, no. 21, pp. 177–182, 2013. [25](#), [96](#)
- [92] S. Bera, S. Misra, and D. Chatterjee, “C2C: Community-Based Cooperative Energy Consumption in Smart Grid,” *IEEE Transactions on Smart Grid*, vol. 9, no. 5, pp. 4262–4269, 2018. [25](#), [26](#)
- [93] J. Khazaei, D. H. Nguyen, and N. G. M. Thao, “Primary and secondary voltage/frequency controller design for energy storage devices using consensus theory,” *6th International Conference on Renewable Energy Research and Applications*, vol. 2017-Janua, pp. 447–453, 2017. [25](#)
- [94] X. Wang, J. Li, J. Xing, and R. Wang, “A novel finite-time average consensus protocol based on event-triggered nonlinear control strategy for multiagent systems,” *Journal of Inequalities and Applications*, vol. 2017, no. 1, oct 2017. [25](#), [26](#)
- [95] L. Wang and F. Xiao, “Finite-time consensus problems for networks of dynamic agents,” *IEEE Transactions on Automatic Control*, vol. 55, no. 4, pp. 950–955, apr 2010. [26](#)
- [96] W. Liu, W. Gu, J. Wang, W. Yu, and X. Xi, “Game theoretic non-cooperative distributed coordination control for multi-microgrids,” *IEEE Transactions on Smart Grid*, vol. 9, no. 6, pp. 6986–6997, 2018. [26](#)
- [97] J. Chen and Q. Zhu, “A Game-Theoretic Framework for Resilient and Distributed Generation Control of Renewable Energies in Microgrids,” *IEEE Transactions on Smart Grid*, vol. 8, no. 1, pp. 285–295, 2017. [26](#)
- [98] L. Han, T. Morstyn, and M. McCulloch, “Incentivizing Prosumer Coalitions With Energy Management Using Cooperative Game Theory,” *IEEE Transactions on Power Systems*, vol. 34, no. 1, pp. 303–313, 2019. [26](#)

- [99] G. Lou, W. Gu, Y. Xu, M. Cheng, and W. Liu, “Distributed MPC-Based Secondary Voltage Control Scheme for Autonomous Droop-Controlled Microgrids,” *IEEE Transactions on Sustainable Energy*, vol. 8, no. 2, pp. 792–804, 2017. [26](#)
- [100] S. C. Dhulipala, R. V. A. Monteiro, R. F. S. Teixeira, C. Ruben, A. Bretas, and G. C. Guimaraes, “Distributed Model Predictive Control Strategy for Distribution Networks Volt/VAR Control: A Smart Buildings Based Approach,” *IEEE Transactions on Industry Applications*, vol. 9994, 2019. [26](#)
- [101] X. Xing, L. Xie, and H. Meng, “Cooperative energy management optimization based on distributed MPC in grid-connected microgrids community,” *International Journal of Electrical Power and Energy Systems*, vol. 107, no. August 2018, pp. 186–199, 2019. [26](#)
- [102] E. Hammad, A. Farraj, and D. Kundur, “On Effective Virtual Inertia of Storage-Based Distributed Control for Transient Stability,” *IEEE Transactions on Smart Grid*, vol. 10, no. 1, pp. 327–336, 2019. [26](#)
- [103] B. K. Poolla, D. Groß, and F. Dörfler, “Placement and Implementation of Grid-Forming and Grid-Following Virtual Inertia and Fast Frequency Response,” *IEEE Transactions on Power Systems*, vol. 34, no. 4, pp. 3035–3046, 2019. [26](#), [28](#)
- [104] S. S. Guggilam, C. Zhao, E. D. Anese, Y. C. Chen, and S. V. Dhople, “Optimizing DER participation in inertial and primary-frequency response,” *IEEE Transactions on Power Systems*, vol. 33, no. 5, pp. 5194–5205, sep 2018. [26](#)
- [105] F. Ju, J. Wang, J. Li, G. Xiao, and S. Biller, “Virtual battery: A battery simulation framework for electric vehicles,” *IEEE Transactions on Automation Science and Engineering*, vol. 10, no. 1, pp. 5–15, 2013. [27](#)
- [106] J. T. Hughes, A. D. Domínguez-García, and K. Poolla, “Identification of Virtual Battery Models for Flexible Loads,” *IEEE Transactions on Power Systems*, vol. 31, no. 6, pp. 4660–4669, 2016. [27](#), [43](#)

- [107] N. S. Raman and P. Barooah, "On the round-trip efficiency of an HVAC-Based virtual battery," *IEEE Transactions on Smart Grid*, vol. 11, no. 1, pp. 403–410, 2020. [27](#)
- [108] I. Chakraborty, S. P. Nandanoori, S. Kundu, and K. Kalsi, "Stochastic Virtual Battery Modeling of Uncertain Electrical Loads Using Variational Autoencoder," *American Control Conference (accepted)*, vol. 2, pp. 2–7, 2020. [27](#)
- [109] S. P. Nandanoori, I. Chakraborty, T. Ramachandran, and S. Kundu, "Identification and Validation of Virtual Battery Model for Heterogeneous Devices," *IEEE Power and Energy Society General Meeting*, vol. 2019-August, 2019. [27](#), [43](#)
- [110] E. Spahic, D. Varma, G. Beck, G. Kuhn, and V. Hild, "Impact of reduced system inertia on stable power system operation and an overview of possible solutions," *IEEE Power and Energy Society General Meeting*, vol. 2016-Novem, no. 0325663, pp. 1–5, 2016. [27](#)
- [111] D. Groß, S. Bolognani, B. K. Poolla, and F. Dörfler, "Increasing the Resilience of Low-inertia Power Systems by Virtual Inertia and Damping," in *Proceedings of IREP Symposium*, 2017. [27](#)
- [112] J. Fang, H. Li, Y. Tang, and F. Blaabjerg, "Distributed Power System Virtual Inertia Implemented by Grid-Connected Power Converters," *IEEE Transactions on Power Electronics*, vol. 33, no. 10, pp. 8488–8499, 2018. [27](#)
- [113] S. M. Vaca, C. Patsios, and P. Taylor, "Sizing of hybrid energy storage systems for frequency response of solar farms in Ecuador," *IEEE PES Innovative Smart Grid Technologies Conference - Latin America, ISGT Latin America*, vol. 2017-January, pp. 1–7, 2017. [27](#), [28](#)
- [114] F. Zhang, Z. Hu, K. Meng, L. Ding, and Z. Dong, "HESS sizing methodology for an existing thermal generator for the promotion of AGC response ability," *IEEE Transactions on Sustainable Energy*, vol. 11, no. 2, pp. 608–617, 2020. [27](#), [28](#)
- [115] T. Jiang, H. Chen, X. Li, R. Zhang, X. Kou, and F. Li, "Optimal Sizing and Operation Strategy for Hybrid Energy Storage Systems Considering Wind Uncertainty,"

- IEEE Power and Energy Society General Meeting*, vol. 2018-August, no. 2, 2018. 27, 28
- [116] Y. Liu, W. Du, L. Xiao, H. Wang, S. Bu, and J. Cao, "Sizing a Hybrid Energy Storage System for Maintaining Power Balance of an Isolated System with High Penetration of Wind Generation," *IEEE Transactions on Power Systems*, vol. 31, no. 4, pp. 3267–3275, 2016. 27, 28
- [117] R. Fernández-Blanco, Y. Dvorkin, B. Xu, Y. Wang, and D. S. Kirschen, "Optimal Energy Storage Siting and Sizing: A WECC Case Study," *IEEE Transactions on Sustainable Energy*, vol. 8, no. 2, pp. 733–743, 2017. 28
- [118] C. K. Das, T. S. Mahmoud, O. Bass, S. M. Muyeen, G. Kothapalli, A. Baniasadi, and N. Mousavi, "Optimal sizing of a utility-scale energy storage system in transmission networks to improve frequency response," *Journal of Energy Storage*, vol. 29, no. November 2019, p. 101315, 2020. 28
- [119] Y. V. Makarov, P. Du, M. C. W. Kintner-Meyer, C. Jin, and H. F. Illian, "Sizing energy storage to accommodate high penetration of variable energy resources," *IEEE Transactions on Sustainable Energy*, vol. 3, no. 1, pp. 34–40, 2012. 28
- [120] J. Xiao, L. Bai, F. Li, H. Liang, and C. Wang, "Sizing of energy storage and diesel generators in an isolated microgrid Using Discrete Fourier Transform (DFT)," *IEEE Transactions on Sustainable Energy*, vol. 5, no. 3, pp. 907–916, 2014. 28, 47
- [121] H. Wang, Q. Lv, G. Yang, and H. Geng, "Siting and sizing method of energy storage system of microgrid based on power flow sensitivity analysis," *The Journal of Engineering*, vol. 2017, no. 13, pp. 1974–1978, 2017. 28
- [122] S. M. Hakimi, A. Hasankhani, M. Shafie-khah, and J. P. Catalão, "Optimal sizing and siting of smart microgrid components under high renewables penetration considering demand response," *IET Renewable Power Generation*, vol. 13, no. 10, pp. 1809–1822, 2019. 28

- [123] M. M. A. Abdelaziz, H. E. Farag, E. F. El-Saadany, and Y. A. R. I. Mohamed, "A novel and generalized three-phase power flow algorithm for islanded microgrids using a newton trust region method," *IEEE Transactions on Power Systems*, vol. 28, no. 1, pp. 190–201, 2013. [29](#)
- [124] F. Mumtaz, M. H. Syed, M. A. Hosani, and H. H. Zeineldin, "A Novel Approach to Solve Power Flow for Islanded Microgrids Using Modified Newton Raphson with Droop Control of DG," *IEEE Transactions on Sustainable Energy*, vol. 7, no. 2, pp. 493–503, 2016. [29](#)
- [125] F. Hameed, M. A. Hosani, and H. H. Zeineldin, "A modified backward/forward sweep load flow method for islanded radial microgrids," *IEEE Transactions on Smart Grid*, vol. 10, no. 1, pp. 910–918, Jan 2019. [29](#), [117](#), [125](#)
- [126] J. H. Teng, "A direct approach for distribution system load flow solutions," *IEEE Transactions on Power Delivery*, vol. 18, no. 3, pp. 882–887, 2003. [29](#), [115](#), [118](#), [119](#)
- [127] V. Mohan, R. Suresh, J. G. Singh, W. Ongsakul, and N. Madhu, "Microgrid Energy Management Combining Sensitivities, Interval and Probabilistic Uncertainties of Renewable Generation and Loads," *IEEE Journal on Emerging and Selected Topics in Circuits and Systems*, vol. 7, no. 2, pp. 262–270, 2017. [30](#)
- [128] Y. Li, W. Li, W. Yan, J. Yu, and X. Zhao, "Probabilistic optimal power flow considering correlations of wind speeds following different distributions," *IEEE Transactions on Power Systems*, vol. 29, no. 4, pp. 1847–1854, 2014. [30](#), [119](#)
- [129] M. Fan, V. Vittal, G. T. Heydt, and R. Ayyanar, "Probabilistic power flow studies for transmission systems with photovoltaic generation using cumulants," *IEEE Transactions on Power Systems*, vol. 27, no. 4, pp. 2251–2261, 2012. [30](#), [120](#)
- [130] X. Ai, S. Member, and J. Wen, "A Discrete Point Estimate Method for Probabilistic Load Flow Based on the Measured Data of Wind Power," *IEEE Transactions on Industry Applications*, vol. 49, no. 5, pp. 2244–2252, 2013. [30](#)

- [131] S. J. Yao and W. Yan, “Cornish-Fisher Expansion for Probabilistic Power Flow of the Distribution System with Wind Energy System,” in *4th International Conference on Electric Utility Deregulation and Restructuring and Power Technologies*, 2011, pp. 1378–1383. [30](#)
- [132] Z. Ren, W. Li, R. Billinton, and W. Yan, “Probabilistic Power Flow Analysis Based on the Stochastic Response Surface Method,” *IEEE Transactions on Power Systems*, vol. 31, no. 3, pp. 2307–2315, 2016. [30](#), [125](#)
- [133] A. S. Vijay, D. K. Dheer, A. Tiwari, and S. Doolla, “Performance evaluation of homogeneous and heterogeneous droop-based systems in microgrid-stability and transient response perspective,” *IEEE Transactions on Energy Conversion*, vol. 34, no. 1, pp. 36–46, 2019. [31](#)
- [134] D. K. Dheer, N. Soni, and S. Doolla, “Improvement of small signal stability margin and transient response in inverter-dominated microgrids,” *Sustainable Energy, Grids and Networks*, vol. 5, pp. 135–147, 2016. [31](#)
- [135] R. Wang, Q. Sun, D. Ma, and Z. Liu, “The Small-Signal Stability Analysis of the Droop-Controlled Converter in Electromagnetic Timescale,” *IEEE Transactions on Sustainable Energy*, vol. 10, no. 3, pp. 1459–1469, 2019. [31](#)
- [136] Z. Zeng, H. Yang, and R. Zhao, “Study on small signal stability of microgrids: A review and a new approach,” *Renewable and Sustainable Energy Reviews*, vol. 15, no. 9, pp. 4818–4828, 2011. [31](#)
- [137] S. Daarco and J. A. Suul, “Small-Signal analysis of an isolated power system controlled by a virtual synchronous machine,” *Proceedings - 2016 IEEE International Power Electronics and Motion Control Conference, PEMC 2016*, pp. 462–469, 2016. [31](#)
- [138] J. Ma, Z. Song, Y. Zhang, Y. Shen, and J. S. Thorp, “Model order reduction analysis of DFIG integration on the power system small-signal stability considering the virtual inertia control,” *IET Generation, Transmission and Distribution*, vol. 11, no. 16, pp. 4087–4095, 2017. [31](#)

- [139] F. D. Simpson-porco J., John W. and B. F., “Synchronization and Power Sharing for Droop-Controlled Inverters in Islanded Microgrids,” *Automatica*, vol. 49, no. 9, pp. 2603–2611, 2013. 31
- [140] J. Schiffer, R. Ortega, A. Astolfi, J. Raisch, and T. Sezi, “Conditions for stability of droop-controlled inverter-based microgrids,” *Automatica*, vol. 50, no. 10, pp. 2457–2469, 2014. 31
- [141] S. Kundu, W. Du, S. P. Nandanoori, F. Tuffner, and K. Schneider, “Identifying parameter space for robust stability in nonlinear networks: A microgrid application,” *Proceedings of the American Control Conference*, vol. 2019-July, no. 1, pp. 3111–3116, 2019. 31
- [142] S. P. Nandanoori, S. Kundu, W. Du, F. Tuffner, and K. P. Schneider, “Distributed Small-Signal Stability Conditions for Inverter-Based Unbalanced Microgrids,” *IEEE Transactions on Power Systems*, vol. 8950, no. c, pp. 1–1, 2020. 31, 136, 137
- [143] S. Kundu, S. P. Nandanoori, K. Kalsi, S. Geng, and I. A. Hiskens, “Distributed barrier certificates for safe operation of inverter-based microgrids,” *Proceedings of the American Control Conference*, vol. 2019-July, pp. 1042–1047, 2019. 31
- [144] J. Fang, H. Li, Y. Tang, and F. Blaabjerg, “On the Inertia of Future More-Electronics Power Systems,” *IEEE Journal of Emerging and Selected Topics in Power Electronics*, vol. 7, no. 4, pp. 2130–2146, 2019. 34, 35
- [145] ENTSO-E. (2018) Rate of Change of Frequency (RoCoF) withstand capability. [Online]. Available: <https://docstore.entsoe.eu> 35
- [146] CERC, Govt. of India. (2020) Report of the Expert Group : Review of Indian Electricity Grid Code. [Online]. Available: <http://www.cercind.gov.in/> 35
- [147] Y. Zhang, J. Jiang, Y. An, L. Wu, H. Dou, J. Zhang, Y. Zhang, S. Wu, M. Dong, X. Zhang, and Z. Guo, “Sodium-ion capacitors: Materials, Mechanism, and Challenges,” *ChemSusChem*, vol. 13, no. 10, pp. 2522–2539, 2020. 37

- [148] T. M. Gür, “Review of electrical energy storage technologies, materials and systems: Challenges and prospects for large-scale grid storage,” *Energy and Environmental Science*, vol. 11, no. 10, pp. 2696–2767, 2018. [37](#)
- [149] M. Bagheri-Sanjareh, M. H. Nazari, and G. B. Gharehpetian, “A novel and optimal battery sizing procedure based on mg frequency security criterion using coordinated application of bess, led lighting loads, and photovoltaic systems,” *IEEE Access*, vol. 8, pp. 95 345–95 359, 2020. [40](#), [41](#)
- [150] J. J. Nedumgatt, K. B. Jayakrishnan, S. Umashankar, D. Vijayakumar, and D. P. Kothari, “Perturb and observe MPPT algorithm for solar PV systems-modeling and simulation,” *Annual IEEE India Conference: Engineering Sustainable Solutions, INDICON*, no. 1, 2011. [40](#)
- [151] M. Parshin, M. Majidi, F. Ibanez, and D. Pozo, “On the use of thermostatically controlled loads for frequency control,” *IEEE Milan PowerTech*, 2019. [42](#)
- [152] J. Liu, W. Zhang, and Y. Liu, “Primary Frequency Response from the Control of LED Lighting Loads in Commercial Buildings,” *IEEE Transactions on Smart Grid*, vol. 8, no. 6, pp. 2880–2889, 2017. [42](#)
- [153] Y. Shan, J. Hu, Z. Li, and J. M. Guerrero, “A model predictive control for renewable energy based AC microgrids without any PID regulators,” *IEEE Transactions on Power Electronics*, vol. 33, no. 11, pp. 9122–9126, nov 2018. [54](#)
- [154] S. P. Nandanoori, I. Chakraborty, T. Ramachandran, and S. Kundu, “Identification and validation of virtual battery model for heterogeneous devices,” in *2019 IEEE Power Energy Society General Meeting (PESGM)*, 2019, pp. 1–5. [64](#)
- [155] T. Morstyn, B. Hredzak, and V. G. Agelidis, “Distributed cooperative control of microgrid storage,” *IEEE Transactions on Power Systems*, vol. 30, no. 5, pp. 2780–2789, 2015. [64](#), [66](#)
- [156] N. Papathanassiou, S. and Hatziaargyriou and K. Strunz, “A Benchmark Low Voltage Microgrid Network,” in *CIGRE Symposium, Athens, Greece.*, 2005, pp. 1–8. [66](#)

- [157] J. Wang, A. Pratt, and M. Baggu, “Integrated Synchronization Control of Grid-Forming Inverters for Smooth Microgrid Transition,” *IEEE Power and Energy Society General Meeting*, vol. 2019-August, pp. 0–4, 2019. [84](#)
- [158] A. Mohd, E. Ortjohann, W. Sinsukthavorn, M. Lingemann, N. Hamsic, and D. Morton, “Isochronous load sharing and control for inverterbased distributed generation,” *2009 International Conference on Clean Electrical Power, ICCEP*, pp. 324–329, 2009. [85](#)
- [159] J. M. Guerrero, J. Matas, L. G. de Vicuna, M. Castilla, and J. Miret, “Decentralized control for parallel operation of distributed generation inverters using resistive output impedance,” *IEEE Transactions on Industrial Electronics*, vol. 54, no. 2, pp. 994–1004, 2007. [88](#), [89](#), [99](#), [134](#)
- [160] W. Yao, M. Chen, J. Matas, J. M. Guerrero, and S. Member, “Design and Analysis of the Droop Control Method for Parallel Inverters Considering the Impact of the Complex Impedance on the Power Sharing,” *IEEE Transactions on Industrial Electronics*, vol. 58, no. 2, pp. 576–588, 2011. [88](#), [89](#)
- [161] Y. A. R. I. Mohamed and E. F. El-Saadany, “Adaptive decentralized droop controller to preserve power sharing stability of paralleled inverters in distributed generation microgrids,” *IEEE Transactions on Power Electronics*, vol. 23, no. 6, pp. 2806–2816, 2008. [90](#)
- [162] B. T. Stewart, S. J. Wright, and J. B. Rawlings, “Cooperative distributed model predictive control for nonlinear systems,” *Journal of Process Control*, vol. 21, no. 5, pp. 698–704, 2011. [97](#)
- [163] S. Isukapalli, “Computational methods for sensitivity and uncertainty analysis for environmental and biological models,” *National Exposure Research Laboratory, US Environmental Protection Agency*, vol. 600, no. 1, p. 68, 2001. [122](#), [123](#)
- [164] I. Dobson, “Computing a closest bifurcation instability in multidimensional parameter space,” *Journal of Nonlinear Science*, vol. 3, no. 1, pp. 307–327, 1993. [132](#)

List of Publications

1. L. Subramanian, V. Debusschere, H. B. Gooi and N. Hadjsaid, "A Distributed Model Predictive Control Framework for Grid-friendly Distributed Energy Resources," in *IEEE Transactions on Sustainable Energy*, doi: 10.1109/TSTE.2020.3018913.
2. L. Subramanian, V. Debusschere, H. B. Gooi, and N. Hadjsaid, "A Cooperative Rate-based Model Predictive Framework for Flexibility Management of DERs." (Journal submission under review)
3. L. Subramanian, V. Debusschere and H. B. Gooi, "Design and Control of Storage Systems for Voltage Source Controlled Autonomous Microgrids," *2019 IEEE Power & Energy Society General Meeting (PESGM)*, Atlanta, GA, USA, 2019, pp. 1-5, doi: 10.1109/PESGM40551.2019.8973887.
4. L. Subramanian and H. B Gooi, "Stabilizing Droop Variation of Converter-Connected Generation in Autonomous Microgrids with Virtual Inertia Control," *2018 IEEE Energy Conversion Congress and Exposition (ECCE)*, Portland, OR, 2018, pp. 3746-3753, doi: 10.1109/ECCE.2018.8557936.
5. L. Subramanian and H. B. Gooi, "Stochastic Backward/Forward Sweep Power Flow Analysis for Islanded Microgrids," *2018 IEEE Innovative Smart Grid Technologies - Asia (ISGT Asia)*, Singapore, 2018, pp. 48-53, doi: 10.1109/ISGT-Asia.2018.8467763.

Résumé de la Thèse

Le système électrique est traditionnellement alimenté par des machines tournantes synchrones comme les turbines à vapeur, les turbines hydrauliques et les moteurs diesel. Ces machines tournantes contribuent intrinsèquement à la résilience du système en fournissant une inertie rotative. La fréquence du réseau est indicative du bilan de puissance en temps réel à travers le réseau et peut être traitée comme l'un des principaux indices de performance du réseau. En cas de défaut, l'inertie synchrone aide à atténuer le taux de variation de la fréquence par rapport à sa valeur nominale, c'est-à-dire que plus l'inertie est élevée, plus le taux de variation de la fréquence est faible. La présence d'une inertie adéquate donne donc la liberté de laisser un temps aux commandes de la soupape d'entrée du régulateur pour répondre à la variation de la fréquence.

Avec le remplacement graduel des machines synchrones par de la production renouvelable décentralisée (PED), intermittente et connectée à travers des convertisseurs statiques telles que le solaire PV et l'éolien, la réduction de l'inertie inhérente au système est évidente. Cependant, d'un autre côté, la quantité d'inertie requise dans ce système électrique en évolution est réduite, du fait de la réponse plus rapide des PED commandées par convertisseur. Ainsi, nous devons recourir à l'inertie synthétique pour améliorer la résilience du système électrique, ou à une réponse en fréquence primaire plus rapide pour assurer la fiabilité du système avec une plus faible inertie.

Dans ce contexte, cette thèse explore des questions telles que: Quelle est la capacité adéquate d'inertie synthétique et/ou de la réponse en fréquence pour un système électrique (tendant vers le 100% renouvelable via des convertisseurs) stable? Comment

quantifier la flexibilité nécessaire pour fournir cette inertie adéquate? Une inertie synthétique supérieure au niveau adéquat indique-t-elle nécessairement une marge de stabilité plus élevée? Dans quelle mesure l'effet de l'inertie synthétique décentralisée est-il différent de celui de l'inertie synchrone sur la stabilité oscillatoire?

Premièrement, les aspects de la flexibilité et les méthodes pour les caractériser pour une inertie synthétique adéquate et une réponse en fréquence rapide sont abordés. Un modèle de stockage virtuel a été proposé afin de quantifier les flexibilités hétérogènes bidirectionnelles et leur combinaison pour fournir un certain niveau d'inertie synthétique. À titre d'illustration, un système de stockage d'énergie hybride a été dimensionné pour fournir une inertie synthétique et une réponse en fréquence rapide pour un réseau électrique standard.

Par la suite, l'émulation d'inertie synthétique et le contrôle de fréquence rapide actionné par PV avec stockage d'énergie hybride ont été explorés. Dans cette thèse, le contrôle de l'onduleur a été étudié avec un modèle complet de composants (côté DC) prenant en compte les effets de l'intermittence de production, contrairement à la plupart des travaux de recherche sur le contrôle de l'onduleur qui supposent un stockage DC suffisamment (ou même infiniment) grand.

Les contrôleurs d'inertie synthétique sont classés comme des topologies d'inertie synthétique "grid-following" et "grid-forming", ce qui affecte considérablement leur impact sur la stabilité du système. Classiquement, les paramètres d'inertie et d'amortissement sont réglés et fixés sur une tranche de temps planifiée en fonction de la flexibilité disponible. Il a été observé qu'une inertie plus élevée est requise lors de l'apparition d'une perturbation pour limiter le taux de déviation de la fréquence et un amortissement plus élevé est requis pour un temps de stabilisation plus rapide. Par conséquent, pour chacune des topologies de contrôle, un émulateur d'inertie en temps réel basé sur des règles a été proposé pour optimiser l'écart de fréquence, sa vitesse et le temps de stabilisation. L'algorithme basé sur des règles a été amélioré grâce à une commande prédictive avec une linéarisation qui tient compte du taux de variation des variables d'état. La linéarisation basée sur le taux étend la validité du modèle aux zones transitoires. Pour

les systèmes avec plusieurs "grid-formers" et plusieurs unités sensibles aux fréquences, un problème d'optimisation décentralisée a été formulé et résolu pour régler collectivement les paramètres d'inertie et d'amortissement qui sont limités par les flexibilités disponibles.

L'efficacité de l'inertie synthétique "grid-forming" et "grid-following" décentralisée en remplacement de leur homologue synchrone dans le micro-réseau a été comparée. La régulation des micro-réseaux en mode connectés au réseau et insulaires a été étudiée en modélisant les PED avec des stratégies de contrôle discutées. L'impact des deux types de contrôles d'inertie synthétique sur la stabilité en petits signaux du système est examiné par l'analyse modale et les diagrammes de bifurcation pour dériver les conditions de stabilité oscillatoire dans un micro-réseau avec des réserves d'inertie synthétique décentralisée. L'efficacité des stratégies de contrôle proposées pour restaurer la stabilité en fréquence des systèmes à faible inertie a été validée par l'expérimentation "power hardware-in-the-loop".